2007-07-18

Dynamic Testing of a Full-Scale Pile Cap with Dense Silty Sand Backfill

Todd J. Valentine
Brigham Young University - Provo

DYNAMIC TESTING OF A FULL-SCALE PILE CAP WITH DENSE SILTY SAND BACKFILL

by

Todd J. Valentine

A thesis submitted to the faculty of

Brigham Young University

in partial fulfillment of the requirements for the degree of

Master of Science

Department of Civil and Environmental Engineering

Brigham Young University

August 2007

BRIGHAM YOUNG UNIVERSITY

GRADUATE COMMITTEE APPROVAL

of a thesis submitted by

Todd J. Valentine

This thesis has been read by each member of the following graduate committee and by majority vote has been found to be satisfactory.

Date	Travis M. Gerber, Chair
Date	Kyle M. Rollins
Date	Norm L. Jones

BRIGHAM YOUNG UNIVERSITY

As chair of the candidate's graduate committee, I have read the thesis of Todd J. Valentine in its final form and have found that (1) its format, citations, and bibliographical style are consistent and acceptable and fulfill university and department style requirements; (2) its illustrative materials including figures, tables, and charts are in place; and (3) the final manuscript is satisfactory to the graduate committee and is ready for submission to the university library.

Date

Travis M. Gerber
Chair, Graduate Committee

Accepted for the Department

Steven E. Benzley
Department Chair

Accepted for the College

Alan R. Parkinson
Dean, Ira A. Fulton College of Engineering and Technology

ABSTRACT

DYNAMIC TESTING OF A FULL-SCALE PILE CAP WITH DENSE SILTY SAND BACKFILL

Todd J. Valentine

Department of Civil and Environmental Engineering

Master of Science

Full-scale dynamic lateral load tests were performed on a pile cap with a dense silty sand backfill condition. Two hydraulic load actuators connected a test pile cap with a reaction cap. The load actuators incrementally loaded the test cap up to 50 mm of displacement. After each load increment, the displacement was held constant while an eccentric mass shaker induced dynamic loads under a ramping sequence from 1 Hz to 10 Hz. A baseline response was developed under a no backfill condition. Passive soil pressure was measured using pressure cells and tactile sensors.

It was concluded that the presence of the backfill significantly increased the lateral load resistance of the pile-cap system, with the resistance nearly doubling at a 50 mm deflection level. After initial loading, the pile cap system experienced a loss in load resistance. In the case with backfill present, this relaxation generally represented

a 10 to 15% loss in resistance. Additionally, after undergoing dynamic, cyclic loading, the resistance was approximately 40 to 80% of its initial value. Dynamic displacement amplitudes were on the order of 0 to 2 mm. Passive pressure from the backfill was observed to be non-linear with a concentration of pressure near the bottom of the pile cap. Rankine, Coulomb, and log-spiral earth pressure theories underestimated the passive earth pressure from the backfill by at least 30%.

The natural frequency of the pile cap increased with increasing with static displacement level while placement of the backfill further increased the frequency of the pile cap. On average, the presence of the backfill increased the reloading stiffness of the pile cap by a factor of three to four, whereas the damping ratio increased by a factor of two. The dense silty sand backfill acting by itself on the face of the 1.12 m tall and 5.18 m wide pile cap face exhibited a reloading stiffness on the order of 120 to 250 kN/mm and a damping ratio of 30 to 70%. These damping ratios are significantly higher than that typical expected for structural materials but appear to be consistent with values for soils.

ACKNOWLEDGMENTS

I would like to first of all thank my graduate advisor, Dr. Travis M. Gerber, for his time and patience with me in this project. He has been a wonderful mentor and friend to me throughout my education at Brigham Young University. He not only helped me through my studies but also in giving great advice in my personal life. I also would like to thank Dr. Kyle M. Rollins for his contributions in this project. Participating in this research with these two professors has been a valuable experience. I wish to express thanks to my final committee member, Dr. Norm L. Jones, for allowing for late submittals and working with me while I've been away from campus.

I gratefully acknowledge the support for this research provided by the National Science Foundation under Award Number CMS-0421312 and the George E. Brown, Jr. Network for Earthquake Engineering Simulation (NEES) which operates under NSF Award Number CMS-0402490.

I would like to thank Robert Nigbor and staff from nees@UCLA equipment site for providing support for the field testing.

I am grateful for the support of David Anderson, BYU Civil Engineering Department Technician, for providing field support, running the equipment, and spending countless hours with me calibrating earth pressure cells.

Thanks to Ku Hyun Kwon and Immanuel “Kaleo” Runnels for assisting in this project. They both have been great friends and have been such valuable assets in the development of the research. I would also like to express my gratitude to everyone else in room 192 for the humor and discussions that made life bearable during the stressful times. I would also like to thank Janice Sorenson and Tamera Seely from the Civil and Environmental Engineering Department for always keeping me on the right path towards graduation.

Sincere thanks to my family for their continuous support and love through my education. I feel greatly blessed to have come from such a wonderful family.

I wish to thank my best friend and companion, Tawnya, for her love, encouragement, and endless support. I have been truly blessed to have her by my side. Finally, I would like to express my thanks to my Father in Heaven for all the many blessings in my life.

TABLE OF CONTENTS

LIST OF TABLES

LIST OF FIGURES

1 Introduction

1.1 Background

Passive earth pressure plays a significant role in stability for bridges and other laterally loaded structures. The Rankine, Coulomb, or log-spiral methods are often used to predict the maximum passive pressure acting on abutment walls and pile caps under static loading; however, the passive pressure-deflection relationship is less predictable. Several methods have come forth in order to predict the load-deflection relationship from varying soil types. Some methods assume a linear elastic relationship while other methods use non-linear relationships for the development of passive earth pressure as a function of deflection.

For seismic loading conditions, these methods may fall short. Most load-deflection relationships were developed using static or extremely slow loading conditions. However, seismic loads include cyclic and dynamic components which affect the load-deflection curve. Cyclic loadings tend to decrease soil strength and stiffness, whereas dynamic loadings increase soil strength and stiffness due to material and radiation damping. Full-scale testing which includes dynamic and cyclic load effects has yet to provide a well-defined load-displacement curve for seismic design situations. Currently, the engineering community uses load-deflection relationships based essential on static load conditions for seismic design.

1.2 Objective of Research

The objective of this research is to develop a load-displacement relationship for a dense silty sand backfill based on full-scale testing which accounts for dynamic and cyclic load affects. The data will provide a better definition of dynamic and cyclic soil response. The full-scale test data obtained from field testing will be available to compare against the performance of small-scale models and computer programs.

2 Literature Review

2.1 Overview

The following sections summarize previous research relative to the measurement and quantification of a soil's passive resistance when subjected to lateral loading from a foundation. The first section will present address the results of some previous full-scale testing conducted to determine the contribution of the soil adjacent to a pile cap in a laterally loaded pile system. The second section reviews studies and methods used for seismic loadings on various retaining walls. The third section covers research done on the equipment used to measure earth pressures. These studies expressly deal with grid-based tactile sensors and earth pressure cells which play an important role in the full-scale load tests on which this thesis is based. The final section of the review briefly discusses methods currently used in practice for calculating passive resistance of backfill soils surrounding pile caps and abutments under dynamic and static loadings.

2.2 Lateral Resistance of Backfilled Pile Caps

Maroney (1995) and Romstad et al. (1996)

Maroney (1995) and Romstad et al. (1996) report the results of a test they

conducted on a one-half-scale bridge abutment at the University of California at Davis backfilled with a clayey silt soil. The 1.7 m tall west abutment abutment was loaded to failure by applying a longitudinal loading. By subtracting the resistance provided by the piles, the researchers found that the ultimate strength "compared well to the commonly used" pressure value of 370 kPa (7.7 ksf), however, the stiffness was significantly lower than the 115kN/m/m width (200 k/in/ft width) for a 2.5 m (8-foot) high wall as was then currently used by CALTRANS.

Mokwa and Duncan (2001)

Mokwa and Duncan (2001) evaluated the lateral load-resistance of three pile caps at a site near Blacksburg, VA. Their tests began by laterally loading the pile caps in the native soil which consisted of sandy lean clay and sandy silt. The native soil was removed and the cap was laterally loaded again to find the resistance due to the piles alone. Finally, three different types of backfill were used to find the effects of the backfill on the amount of resistance provided by the pile caps. The backfill types were compacted sand, loose sand, and compacted gravel.

The tests found that two of the pile caps were resisting 50% of the load, and the other cap was resisting 40% when the native soil was in place. The load deflection curves can be seen in Figure 2-1. Also, deflections increased upwards to 500% when the native soil was removed. Varying the backfill type demonstrated that pile cap resistance is dependent upon the stiffness and strength of the soil around the cap. Two conclusions were made in evaluating lateral resistance provided by a pile-group/pile-cap foundation. First, lateral resistance increases as the stiffness and strength of soil

around the cap increases. Second, increasing cap thickness or depth results in smaller lateral deflections.

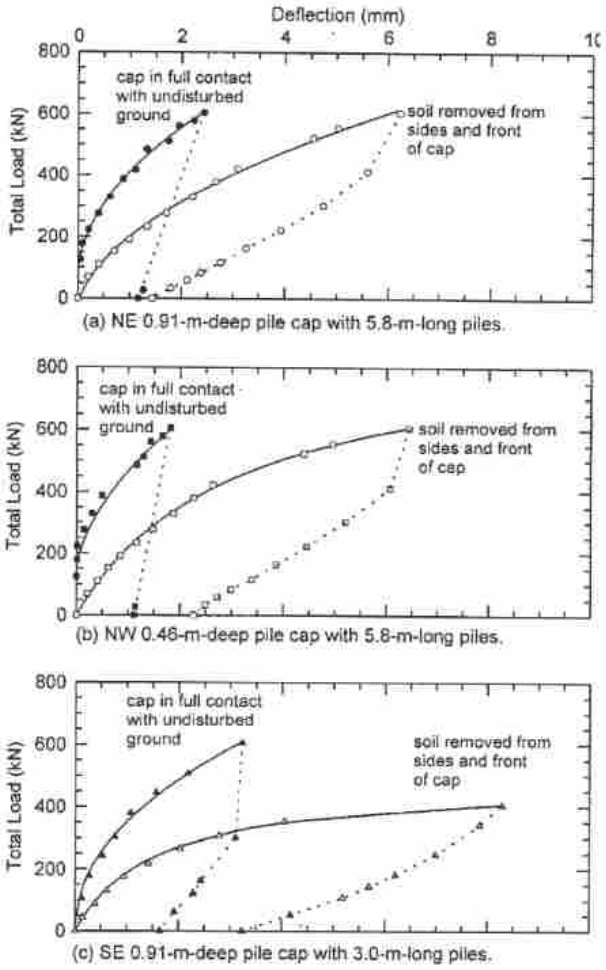

Figure 2-1 Pile Cap Resistance Test Results from Mokwa and Duncan

Cole (2003), Cole and Rollins (2006), and Rollins and Cole (2006)

Cole and Rollins performed cyclic lateral load tests on a full-scale 4 x 3 pile group attached to a concrete pile cap 1.12 m in height by 3.05 m in length by 5.18 m in width (Cole, 2003; Cole and Rollins, 2006; Rollins and Cole, 2006). These tests included two tests without any backfill around the pile cap, four tests with different soil types backfilled around the pile cap, and one test with a trench excavated between

the pile cap and backfill. The first two tests isolated the passive resistance contributed by the piles without backfill. The following four tests used backfill consisting of clean sand, silty sand, fine gravel, and coarse gravel. The load-deflection curves without backfill were then subtracted from the various backfill load-deflection curves to obtain the passive resistance attributed by the backfill as shown in Figure 2-2.

Cole and Rollins concluded that the log spiral method, in general, predicts well the observed failure surface geometry and was also typically within 15% of the measured value. Overall, the pile cap lateral passive resistance contributed between 33 and 47% of the total lateral resistance. To account for cyclic loading conditions, where backfill soil stiffness degenerates and a gap forms between the backfill and pile cap, a cyclic hyperbolic model was developed. Figure 2-3 shows the relationships between reloaded soil stiffness, Kr, as a function of apparent soil movement, Δ_s, and Δ_p, as related to previous maximum deflection that were established.

Comparing measured results with estimated load-deflection curves using the cyclic hyperbolic model provided varying results, but was reasonably successful in modeling the measured passive force-deflection behavior, despite its simplicity.

2.3 Dynamic Earth Pressures on Retaining Walls

Whitman (1990)

Whitman (1990) examined the seismic design of gravity retaining walls. His examination began with the Mononobe-Okabe equation. The Mononobe-Okabe equation modifies Coulomb's method to account for inertia forces corresponding to

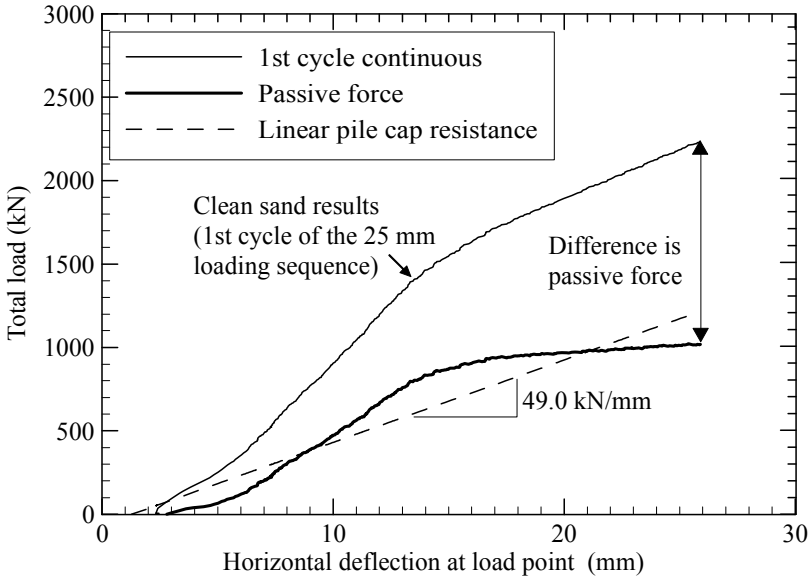

Figure 2-2 Load-deflection Plot Showing How the Passive Force Was Calculated

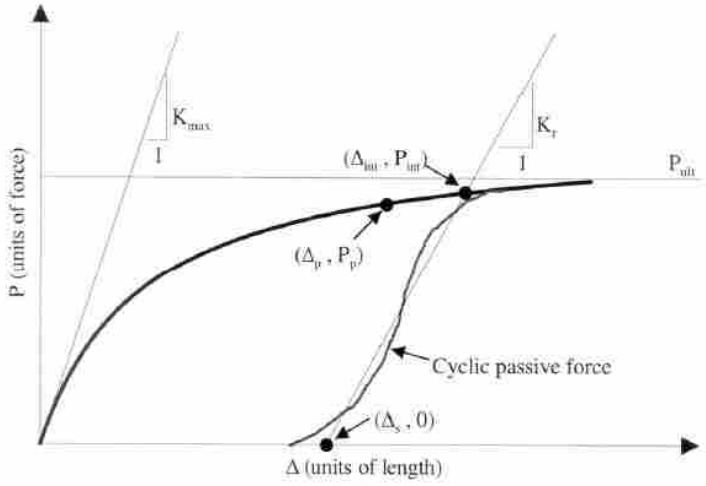

Description of terms
Δ_p – Previous deflection (units of length)
P_p – Previous passive resistance (units of force)
K_{max} - Initial soil stiffness of the load-deflection curve (units of force/length)
K_r - Reloaded soil stiffness (units of force/length)
Δ_s - Apparent soil movement (units of length)
Δ_{int} - Deflection intercept of K_r and hyperbolic relationship (units of length)
P_{int} – Passive load intercept of K_r and hyperbolic relationship (units of force)

Figure 2-3 Proposed Cyclic Hyperbolic Model

horizontal and vertical accelerations, $k_h g$ and $k_v g$ respectively. The backfill thrust against a wall can be expressed as:

$$P_{AE} = (1/2)\gamma(1-k_v)H^2 K_{AE} \quad (1)$$

where γ is the unit weight of backfill, H the height of the wall, and K_{AE} the active stress coefficient. K_{AE} is a function of the friction angle of the backfill, the friction angle between backfill and wall, and of the acceleration coefficients.

The dynamic response of gravity walls is complex due to the backfill forces, the inertia of the wall, and the movement constraints. There are few field studies of actually measured dynamic earth pressures. These tests include the outward sliding of a gravity wall, movement and distortion of the Coulomb wedge, the deformability of the backfill, residual forces, and tilting walls. Selection of an appropriate design acceleration coefficient depends on the allowable permanent movement of the wall. The relationship recommended by Whitman (based on Richards and Elms' interpretation of Newmark sliding block analyses) is as follows:

$$\Delta = 0.087 \frac{V}{Ag}\left(\frac{N}{A}\right)^{-4} \quad (2)$$

where Δ is the permanent displacement, Ag and V are the peak acceleration and peak velocity of the plane, respectively, and N is the maximum acceleration (normalized by the gravitational constant) that can be transmitted across the block/plane interface. It

is suggested in design to select an acceptable displacement and then use a prescribed A and V to find the transmitted acceleration coefficient N by applying Equation 2. The thrust is then found by setting N as the seismic coefficient k_h. The weight of the wall required to resist the thrust is then found and multiplied by a factor of safety. Table 2-1 shows satisfactory factors of safety along with their probabilities.

Table 2-1 Probabilities that Walls Will Not Displace Greater Than Allowable Movements

Safety Factor on Wall Weight	Probability [Actual>allowable]
1.0	90%
1.1	95%
1.2	>95%

Elms and Richards (1990)

Elms and Richards (1990) outlined a displacement-controlled approach to seismic designing, which is derived from Newmark's sliding block model. This method is outlined above in the Whitman literature review. Elms and Richards assumed that the design approach could only be applied to gravity walls failing by sliding. They conducted further experiments to apply the design method to other types of walls and to alternative failure modes. The first experiment tested a gravity wall failing by sliding. The results found that the design method gives an accurate prediction of cutoff acceleration and displacement. Rotation about the base was considered, but preliminary tests were carried out and the test walls were difficult to fail.

Rotation about the top in tied-back walls was considered. The integrity of the tie and anchor and the passive resistance are two of the most important design considerations in tie-back walls. Tests were performed and found the sliding-block assumption applies to a passive-pressure situation if the residual value of φ is used. However, a higher force threshold must be passed, which is considerably higher than for the active sliding wall case. Therefore, the toe of a tied-back wall might be severely weakened if it had survived an earthquake. Tests were also conducted on reinforced earth walls and found that the sliding-block model can be used as long as the residual φ is used.

In conclusion, Elms and Richards found that displacement-controlled design can be applied to gravity walls, tied-back walls, and reinforced earth walls. This method applies only if the residual φ is used.

Bakeer, Shobha, and Ishibashi (1990)

Bakeer et al. (1990) researched experimentally and analytically the effect of dynamic earth pressures on various gravity walls. The current state of practice applies the Mononobe-Okabe formula in design of retaining walls for the dynamic condition, but this formula does not account for mode of movement. Three types of movement modes for retaining walls were tested: rotation about the top, rotation about the bottom, and translation. The experimental test was conducted at the University of Washington. The test consisted of a removable retaining wall with the backfill soil on a shaking table to provide one directional vibration. Comparisons were made of total active thrust, incremental dynamic active thrust, and the point of application of the

earth pressure. A finite element model was created for an analytical investigation. The finite element model tested for the same movement modes as the experimental tests, but also included active rocking of a free wall.

The experiments and analytical models both disagree with the hydrostatic distribution assumed in the Mononobe-Okabe approach. Figure 2-4 graphically shows earth pressure distribution found from the finite element analysis. During all failure modes, the dynamic earth pressure is higher than the Mononobe-Okabe value in the upper third of the wall. The entire height of the wall experienced higher values than the Mononobe-Okabe values when the wall rotated about its base. However, smaller earth pressures than the Mononobe-Okabe values develop near base of the wall during translation, rotation about the top of the wall, and a rocking wall. In conclusion, experimental and analytical research suggests that the Mononobe-Okabe formula may underestimate the magnitude of the dynamic earth pressure, which may result in higher driving forces. A design of an earth retaining structure to resist dynamic forces should account for the expected mode of movement.

2.4 Earth Pressure Instrumentation

Paikowsky and Hajduk (1997)

Paikowsky and Hajduk (1997) tested the calibration and use of a grid-based tactile pressure sensor. The grid-based tactile sensor was developed at MIT, and a firm called Tekscan holds the patent. The tactile pressure technology consists of a sensor that has rows and columns separated by semi-conductive ink. The intersection of these rows and columns make up a sensing area. When a force is applied, the ink's

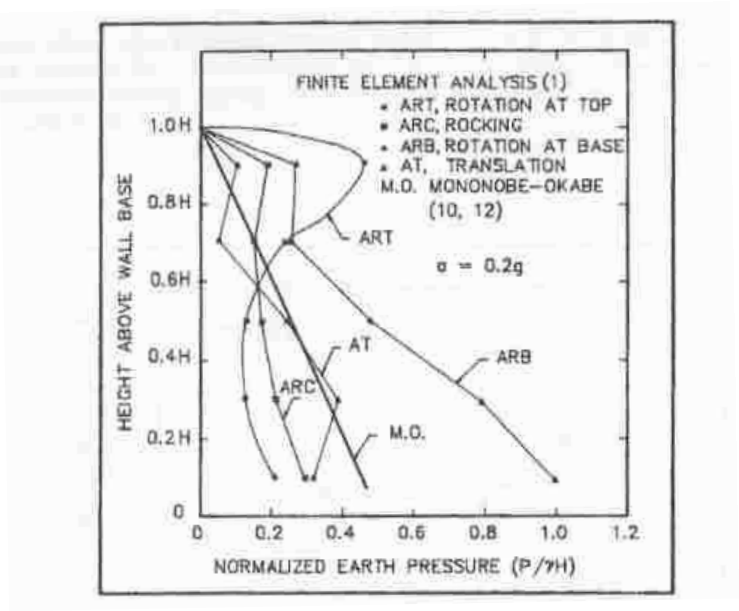

Figure 2-4 Analytical Results of Earth Pressures

resistance is changed, which is then recorded and transferred through a handle and cable to a data acquisition board. The sensor chosen for their research has a sensing area of 84 X 84 mm with a 1,936 individual sensing units. Glass beads were used to represent a granular material.

Three factors were evaluated in calibration of the sensors: the effects of load rate, post loading response (including creep), and hysteresis. A calibration system was set up in order to best represent actual testing conditions. A calibration equation was used in converting raw sensor data (RSD) to pressure. The equation is shown below:

$$Pressure(kPa) = K_{NC}(RSD - b) \tag{3}$$

where RSD is the averaged raw sensor data, K_{NC} is the slope of the applied pressure (a1) divided by the average slope of RSD (a2), and b is the offset of the averaged slope of RSD (in units of RSD).

The following figure (Figure 2-5) shows the load rate calibration diagram used in developing the calibration equation.

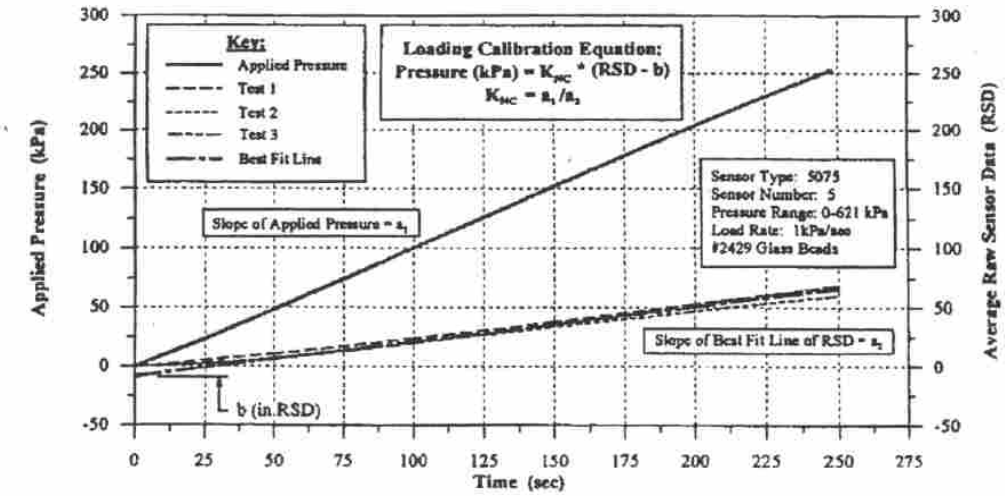

Figure 2-5 Load Rate Calibration Equation

The linear calibration analysis for load rate found that for pressures smaller than 100 kPa, an error of greater than 10% existed. However, for pressures exceeding pressures of 100 kPa, the accuracy was within ±10%. Unloading calibration analysis found that for OCR values of 1 to 1.5, values were within ±20%. For OCR values from 1.5 to 2, values were within ±35%. Post load rate and creep analysis found that the tactile sensor is sensitive to post loading and creep according to load rate and magnitude, but further research is required to quantify the relationship.

A system was set up to determine the accuracy of results in using a grid-based tactile system. The system involved two shear box frames with glass beads placed in the middle. The sensors were located at the front and rear of the system. Figure 2-6 shows the setup for this system. At peak shear resistance at a displacement of 2 mm the normal stress exhibits about four times the "at rest" conditions. This gives an inaccuracy of about ±10%.

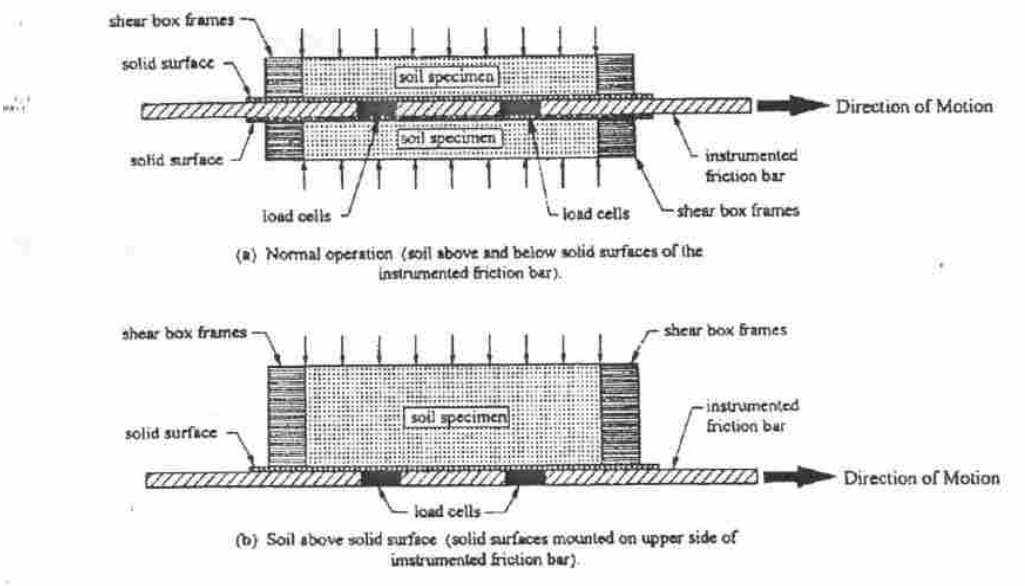

Figure 2-6 Different Test Configurations

Overall, Paikowsky and Hajduk concluded that the implementation of the grid-based tactile system is both feasible and promising.

Filz and Brandon (1994)

George M. Filz and Thomas L. Brandon (1994) tested the effects of compaction-induced lateral pressures. Two methods were used to measure the

dynamic compactor forces: direct instrumentation on the compactors and embedded earth pressure cells. The testing involved burying the pressure cells and compacting the backfill over the sensors. The registration ratio, Equation 4, was used to describe the factors that influence the performance of the pressure cells:

$$R = \frac{\sigma_c}{\sigma_s} \tag{4}$$

where σ_c is the normal stress measured by the cell based on fluid calibration and σ_s is the normal stress present in the soil.

The conclusions made in their research are that standing waves could be created at the pressure cell locations by the reflection of seismic waves off the backfill boundaries. This would cause a slight increase of the pressure cell reading compared to the direct instruments on the compactors. The pressure distributions below the base of the compactor influence the pressure cell readings. A registration ratio of unity was found to best estimate compactor forces. Pressure cell placement influences readings such as different soil conditions and the presence of clods in the backfill. Finally, lateral earth pressure caused by compaction can produce a non-linearity in cell response due to rotation of lateral stresses.

Filz and Duncan (1993)

George M. Filz and J. Michael Duncan (1993) tested pressure cells for drift. The pressure cells were mounted on a wall in a retaining wall facility. The cells were calibrated using two different methods: fluid calibration and in situ (soil) calibration. Soil was filled behind the wall, compacted, and then removed. Pressure cells and load

cells were monitored for drift after compaction was completed. Test conditions varied from test to test. The conditions that varied were soil type, compactor type, lubricated walls, and surface treatment. During the tests, the load cells never drifted; however, the pressure cells did drift. Figure 2-7 below shows drift during one of the tests.

The researchers observed that drift in the pressure cells were very small when the instrumented wall was lubricated. They postulated that the lubricated wall prevented moisture from infiltrating the concrete, and that perhaps during the other tests moisture was migrating from the soil to the concrete wall, causing a slight deformation of the pressure cell. To test moisture migration, the concrete wall was wetted at two cell locations using water in small reservoirs. Readings were taken over time as the cells were submerged. Negative drift occurred. The wall was then dried and treated with three applications of Thompson's Water Seal. The procedure was then repeated with the treated wall. Negative drift still occurred, but was significantly less. Figure 2-8 shown below shows the results of the above mentioned test.

Temperature was also considered for drift; however, temperature was essentially constant throughout the tests. Therefore, temperature change could not have attributed to drift during the tests.

Conclusions drawn from the tests are that pressure cells can be calibrated by applying pressure to the cell through fluid or soil. Data scatter can be reduced by installing a large number of pressure cells or by measuring pressures over large areas. Finally, drift occurred due to the migration of moisture from the soil to the concrete wall resulting in a slight distortion of the cells. Applying Thompson's Water Seal to the retaining wall significantly reduced the drift found in the pressure cells.

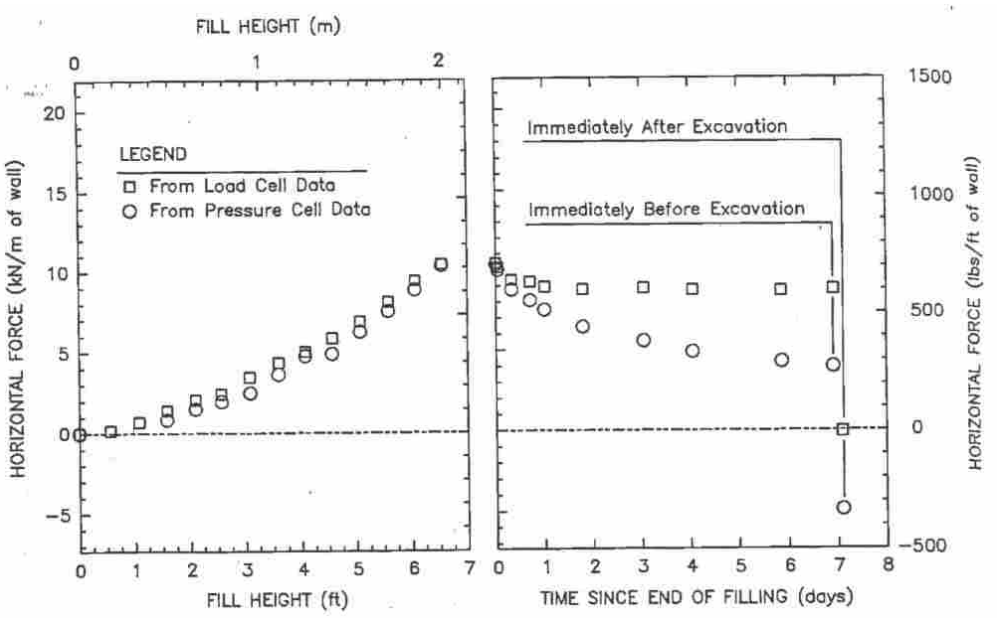

Figure 2-7 Comparison of Horizontal Force Magnitudes

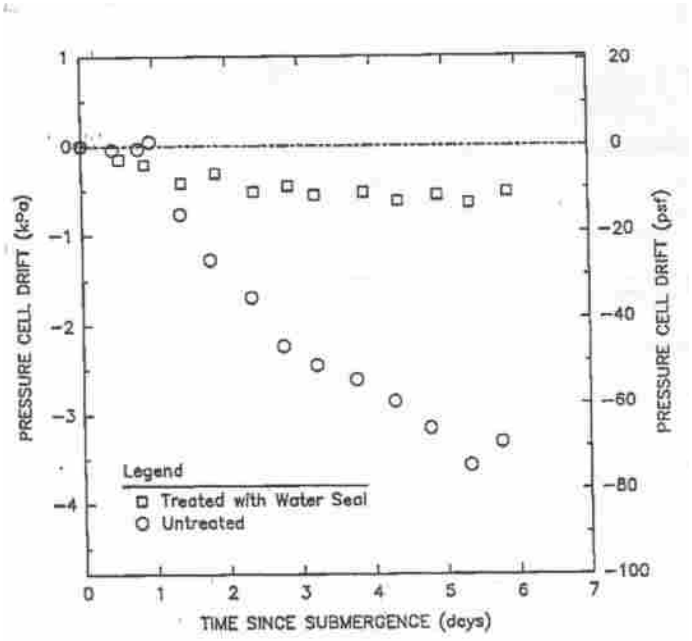

Figure 2-8 Pressure Cell Submergence Result

2.5 Determination of Soil Passive Pressure - State of Practice

CALTRANS (Romstad et al., 1996)

The California Department of Transportation (Romstad et al., 1996) working with the University of California, Davis developed a method in estimating abutment strength and stiffness. (This work was also discussed briefly in the previous summary of research by Maroney (1995)). To predict the passive strength of the soil, they suggest solving Equation 5, Equation 6, Equation 7, and Equation 8, simultaneously which account for friction on the wall and cohesion on the failure plane.

$$0 = P_{bw-soil} - F * \sin\theta - N * \cos\theta \tag{5}$$

$$0 = -D - W - F * \cos\theta + N * \sin\theta \tag{6}$$

$$F = c * (w * h / \cos\theta) + \tan\phi \tag{7}$$

$$D = P_{bw-soil} * \tan\phi_w \tag{8}$$

where W is the weight of the soil wedge above the surface passive failure surface, F is the friction force of the failure surface, N is the normal force developed on the lower failure surface, D is the drag down force developed between the backwall and soil wedge, and $P_{bw\text{-}soil}$ is the passive resistance provided by the soil wedge behind the backwall. Other necessary information for the longitudinal ultimate passive resistance model includes abutment height, h, and width, w. These equations will solve for the passive strength of the soil for a given θ. The free body diagram used in the development of the above equations is shown in Figure 2-9.

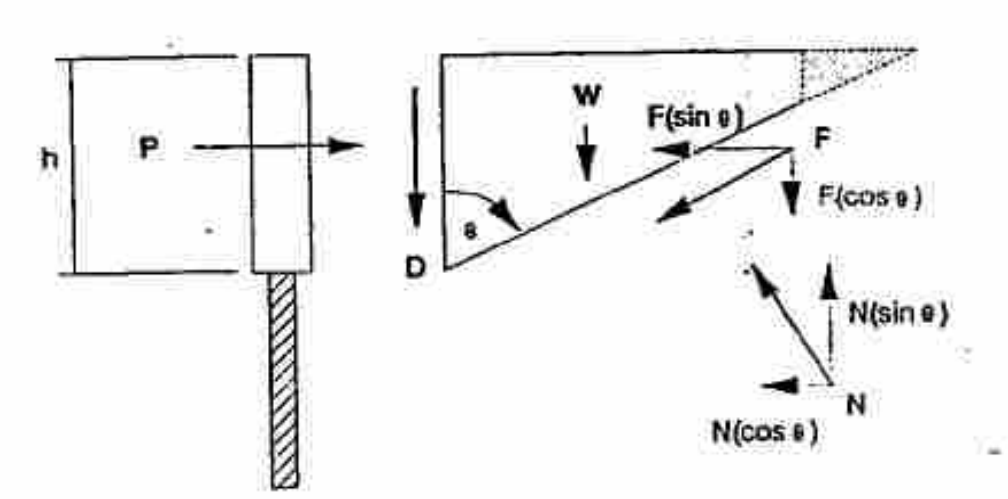

Figure 2-9 Free Body Diagram Developed by CALTRANS

CALTRANS suggests calibrating a load-deflection curve using Equation 9 below which includes information from the procedure mentioned above and a standardized curve, which takes the form of the CALTRANS test data.

$$\frac{P_{bw-soil}}{(P_{bw-soil})_{ult}} = A(\Delta / h) + B(\Delta / h)^{C} \tag{9}$$

where $P_{bw\text{-}soil}$ is defined above. $(P_{bw\text{-}soil})_{ult}$ is the ultimate passive resistance provided by the soil wedge behind the backwall. Δ is the deflection and h is the height of the abutment backwall. "The parameters A, B, and C are determined by (1) fitting the curve to the ultimate backwall-soil load at the (Δ/h) at which the ultimate condition was achieved during the abutment test, (2) fitting the curve's first derivative to zero at the (Δ/h) at which the ultimate backwall-soil load was achieved during the abutment test, and (3) fitting the curve to 70% of the ultimate backwall-soil load at a (Δ/h) of

30% of the (Δ/h) associated with the ultimate backwall-soil load. The third fitting criterion is a simple estimate of significant yield" (Romstad et al., 1996).

Seed and Whitman (1970)

Seed and Whitman (1970) suggest using appropriate factor of safeties in designing bridge abutments and retaining walls. They suggest the factor of safety used in designing for static pressures would be adequate for earthquake loads. Seed and Whitman use the example of designing a retaining wall for an active pressure coefficient of 0.25 with a factor of safety 1.5 against translation by sliding along the base. Seed and Whitman also suggest a factor of safety of 1.15 for the factor of safety due to earthquake forces. This factor of safety would lead the seismic lateral force coefficient K_{AE} to be

$$K_{AE} = 0.25 * \frac{1.5}{1.15} = 0.325 \tag{10}$$

If the peak ground acceleration occurs only once during an earthquake and does not have enough duration to cause significant wall displacement, then the effective ground acceleration will be less than maximum. Seed and Whitman suggest that this might cause wall movements of about 85% of the peak acceleration. This would cause the wall based on the static design to withstand a seismic lateral force coefficient of

$$K_{AE} = 0.325 * \frac{100}{85} = 0.38 \tag{11}$$

If the backfill surface is horizontal with an angle of friction of 35˚, then K_{AE} may be related to the peak ground acceleration $k_h g$ by the approximate equation:

$$K_{AE} = 0.25 + \frac{3}{4} k_h = 0.38 \quad (12)$$

i.e. $k_h = 0.17$

Thus, the wall would have a factor of safety of 1.15 against significant displacements in an earthquake with maximum ground acceleration of about 0.17g, without any extra provisions for seismic effects. Table 2-2 and Table 2-3 display expected acceleration values using a factor of safety of 1.15 against translation during an earthquake. It should be noted that when the backfill slopes at 20˚, the peak acceleration the wall can withstand is significantly reduced. Also, the ability for the wall to resist earthquake forces designed for static pressures depends on factors such as the earth pressure coefficient used for the static pressure design, the factor of safety in the static pressure design, the acceptable factor of safety against translation under seismic loading conditions, the acceptable factor of safety against excessive tilting of the wall under seismic conditions, the angle of friction of the backfill material, and the slope behind the wall.

Duncan and Mokwa (2001)

Duncan and Mokwa (2001) developed a spreadsheet that computes the passive resistance on a structure by using a log spiral analyses numerically. The spreadsheet also provides a correction factor to account for three dimensional effects. A Prandtl

zone near the wall and a Rankine zone at the ground zone are assumed to define the failure mechanism. The shape of the critical log spiral is determined by iteration. The

Table 2-2 Acceleration levels with a factor of safety of 1.15 against translation during an earthquake – Horizontal backfill

Factor of safety against translation due to static pressures only	Tolerable peak acceleration level for walls designed for earth pressure coefficient K_A = 0.25			Tolerable peak acceleration level for walls designed for earth pressure coefficient K_A = 0.30		
	φ_b' = 35˚	φ_b' = 37˚	φ_b' = 39˚	φ_b' = 35˚	φ_b' = 37˚	φ_b' = 39˚
1.5	0.22g	0.25g	0.29g	0.30g	0.33g	0.37g
1.3	0.15g	0.19g	0.22g	0.24g	0.27g	0.31g

Table 2-3 Acceleration levels with a factor of safety of 1.15 against translation during an earthquake – Backfill slope 20˚

Factor of safety against translation due to static pressures only	Tolerable peak acceleration level for walls designed for earth pressure coefficient KA = 0.3		
	φ_b' = 35˚	φ_b' = 37˚	φ_b' = 39˚
1.5	0.12g	0.15g	0.19g
1.3	0.08g	0.11g	0.15g

spiral center is found by computing passive resistance for various locations for three components. The three components are the resistance due to the weight and internal friction of the soil, resistance due to the surcharge and the angle of internal friction of the soil, and the resistance due to the cohesion of the soil. The position of the spiral center is varied until a location is found that results in the smallest passive resistance. The log spiral failure mechanism is shown in Figure 2-10.

The spreadsheet uses Equation 13 to relate passive resistance per unit length of structure to total passive resistance.

$$P_{ult} = (E_p)(M)(b) \tag{13}$$

where P_{ult} is the total passive resistance on the structure (units of force); E_p is the passive resistance per unit length (units of force/length); M is the Ovesen-Brinch Hansen correction factor for 3D effects (dimensionless); and b is the length of the structure perpendicular to the plane of analysis (units of length). An upper limit of 2.0 is placed on the value of M.

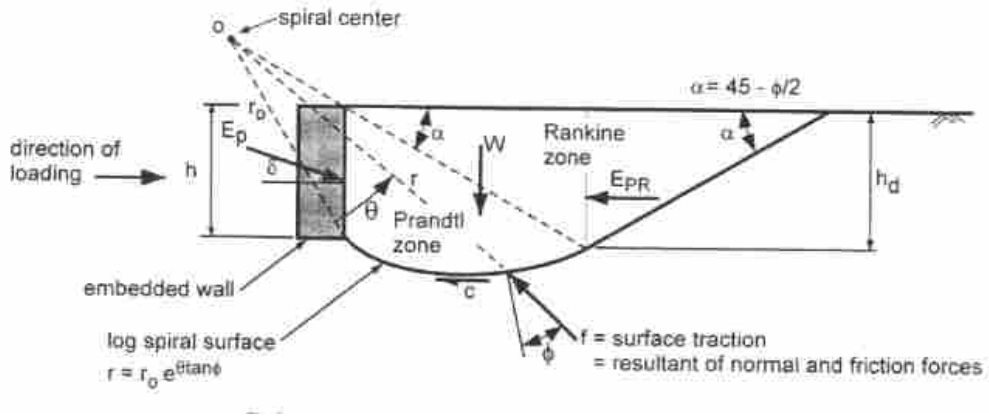

Figure 2-10 Log Spiral Failure Mechanism

The variation of passive resistance with deflection is calculated in the spreadsheet by the hyperbolic relationship defined in Equation 14.

$$P = \frac{y}{\left[\frac{1}{K_{\max}} + R_f \frac{y}{P_{ult}}\right]} \tag{14}$$

where P is the passive resistance (units of force); P_{ult} ultimate (maximum) passive resistance (units of force), computed above; y is the deflection (units of length); K_{max} is the initial stiffness which is the initial slope of the load-deflection curve (units of force/length); and R_f is the failure ratio which is P_{ult}/hyperbolic asymptote (dimensionless).

3 Site Characterization and Experimental Setup

3.1 General

The research for this thesis was conducted at the Interstate 15 (I-15) National Testbed site located in Salt Lake City, Utah at South Temple Street near 700 West underneath Interstate-15. This is the same site with the same pile cap used by Cole and Rollins in their cyclic testing (Cole, 2003; Cole and Rollins, 2006; Rollins and Cole, 2006). A map of the site showing the location of the test cap relative to previous geotechnical testing locations and bridge foundations for the interstate is shown in Figure 3-1.

3.2 Site Characterization

3.2.1 Surface Conditions

The site is relatively vacant, located underneath Interstate-15. Several full-scale pile and pile group tests have been performed in this area, both during and after the reconstruction of I-15. The surface topography is relatively flat at an elevation of approximately 1,289 meters. In the immediate vicinity of the test pile cap, the surface soils were excavated prior to construction, creating an excavated ground surface of 1.1 m on average below the surrounding ground surface.

3.2.2 Subsurface Conditions

The results of several geotechnical investigations conducted at the test site have been compiled and presented by Cole (2003). In-situ testing consisted of standard penetration testing (SPT), cone penetration testing (CPT), pressuremeter testing (PMT), vane shear testing (VST), bore hole shear testing (BST), shear wave velocity testing (SCPT), nuclear density testing, and in-situ direct shear testing. The SPT test relies on blow counts to ascertain approximate relative densities of soil strata. The CPT test yielded various data such as cone tip resistance (q_c), sleeve friction (f_s), and pore water pressure (u). A number of CPT tests were conducted with very similar results, indicating that subsurface conditions are generally consistent throughout the site. Laboratory results consisted of obtaining index properties such as natural moisture content, fines content, unit weights, Atterberg limits and soil classification. Consolidation and shear strength testing was also performed.

The near-surface soils consist of clay, silt and sand deposited after the regressive phase of Lake Bonneville. Most of these surficial deposits were deposited during the Holocene to uppermost Pleistocene age and during the last cycle of Lake Bonneville. The surficial deposits are underlain by lacustrine clay and silt of late Pleistocene age deposited by Lake Bonneville (Personius and Scott, 1992). In general, subsurface soils consist of approximately 5 m of moderately to highly plastic clays interbedded with medium dense silty sand layers, underlain by highly plastic, sensitive clays to a depth of 9.5 m. Deeper soils generally consist of alternating layers of silty sand and moderately plastic clay. An idealized soil profile developed by Cole showing basic soil types and shear strength parameters is shown in Figure 3-2.

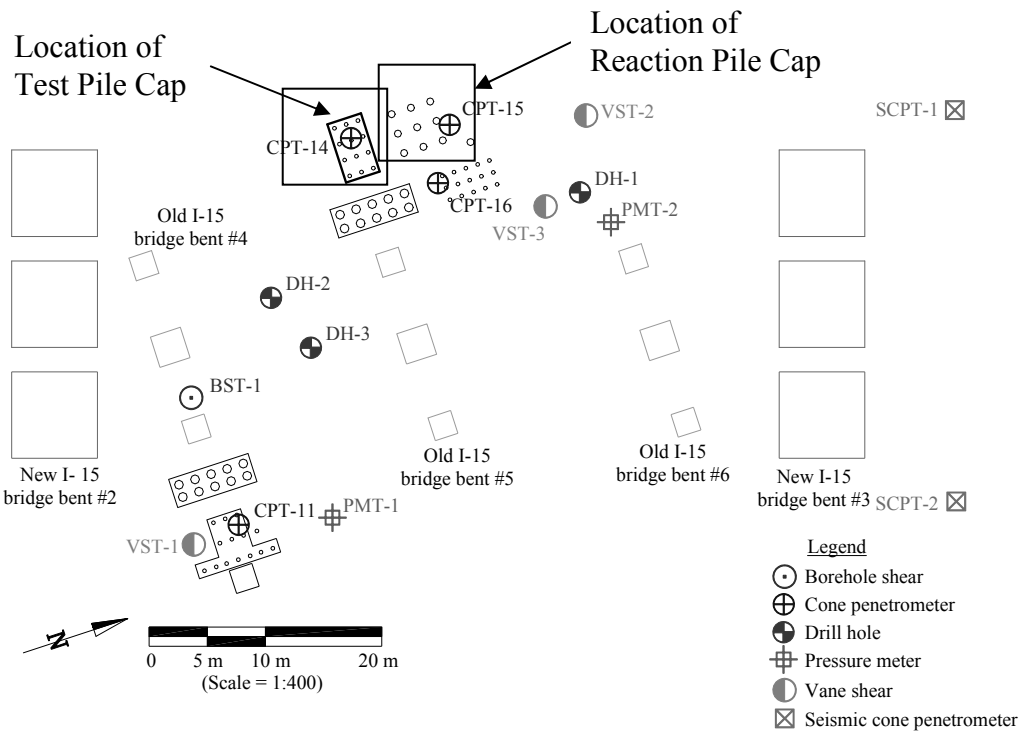

Figure 3-1 Site Map and Geotechnical Test Locations (after Cole, 2003)

3.3 Experimental Setup

3.3.1 General

Figure 3-3 shows the main elements of the load testing program, each of which is discussed in more detail in the following text.

3.3.2 Test Pile Cap

The pile cap used for this research is the same used by Cole and Rollins, but retrofitted to accommodate two hydraulic actuators and an eccentric mass shaker. The cap is a 1.12 m tall reinforced concrete block measuring 5.18 x 3.05 m in plan view.

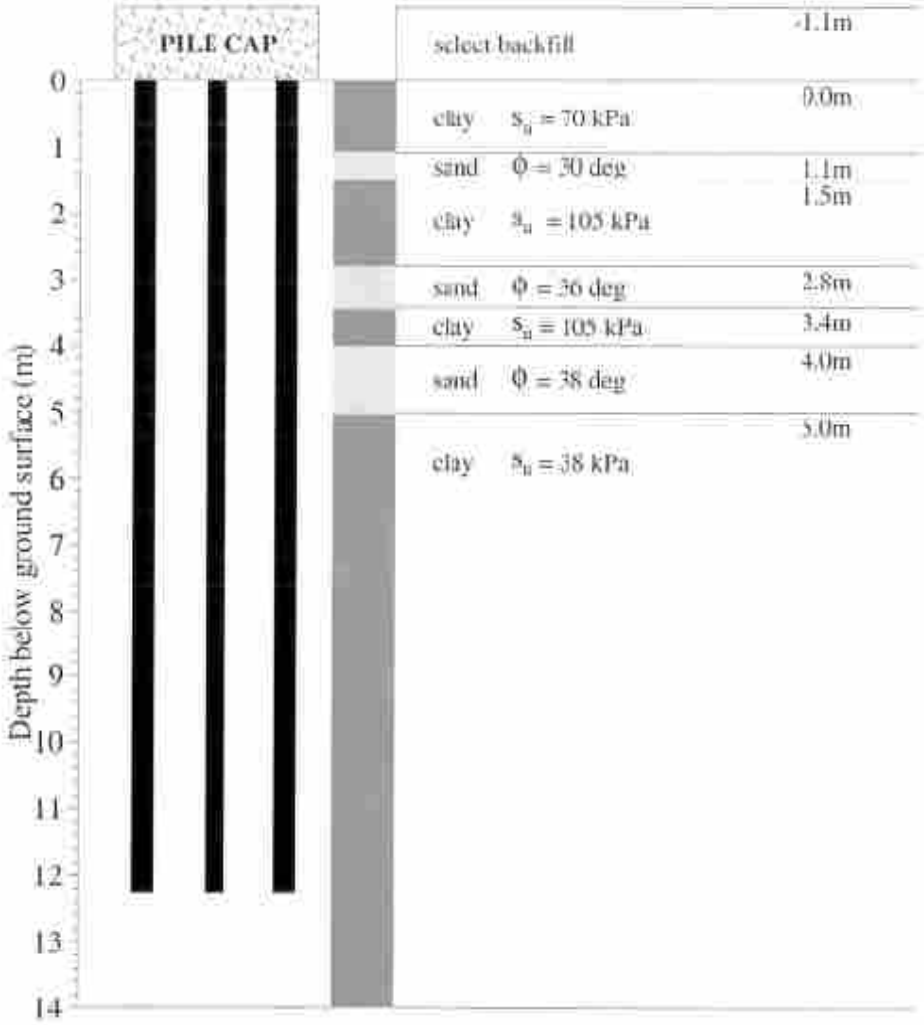

Figure 3-2 Idealized Soil Profile and Strength Properties (Cole, 2003)

The pile cap connects 12 steel pipes installed in a 4 x 3 configuration with center-to-center spacings of 4.4 and 3.3 pile-diameters in the long and short dimensions, respectively. The piles have a 324 mm outside diameter and a 9.5 mm thick wall. The steel pipe piles are ASTM A252, Grade 3 (i.e., 310 MPa minimum yield strength); however, manufacturer mill certifications for 192 specimens of this type of pipe pile had an average yield strength of 404.6 MPa based on a 0.2% offset criteria. The piles extend to a depth of approximately 12.2 m below the excavated ground surface and are

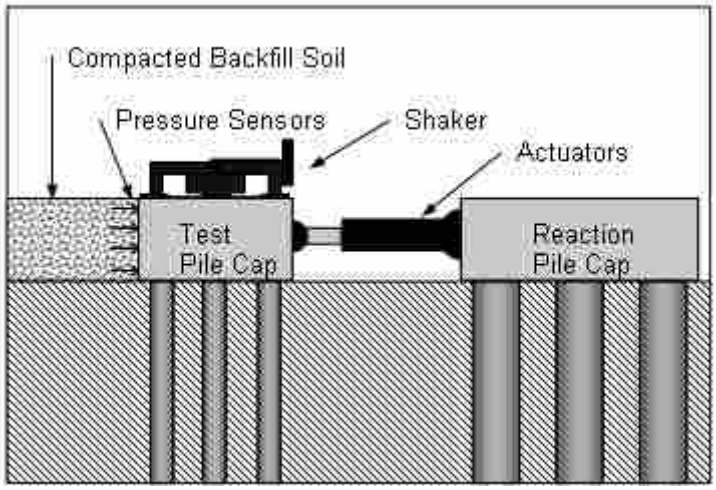

Figure 3-3 Schematic Showing Main Components Used in the Testing Program

filled with concrete. The steel pile sections are embedded approximately 75 mm into the concrete cap. Also a circular reinforcing cage consisting of six #25 vertical bars and a #13 spiral at a 305 mm pitch extends approximately 1.7 m into each pile and 1.06 m into the cap.

3.3.3 Reaction Pile Cap

Prior to testing, a reaction pile cap was constructed approximately 3.84 m north of the existing test pile cap. The existing piles shown to the north of the test cap in Figure 3-1 had to be extracted and reinstalled somewhat to the north using a vibratory hammer so that they would be located beneath the needed location of the reaction cap. The reaction cap is 1.12 m tall and 5.18 x 5.33 m in plan view (with the short direction corresponding to the north and south faces, matching the test cap). The pile cap connects nine steel pipe piles installed in a 3 x 3 configuration with approximately 3 pile-diameter center-to-center spacings. The steel pipe piles have an

outside diameter of 610 mm, a wall thickness of 12.7 mm, and are of the same steel grade as the piles in the test cap. The piles extend to a similar depth of approximately 12.2 m, with the uppermost 2.7 m containing reinforced concrete and the remainder filled with soil. The steel pile sections are embedded approximately 75 mm into the concrete cap. Also, a circular reinforcing cage consisting of eight #32 vertical bars and a #13 spiral at a 152 mm pitch extends approximately 2.74 m into each pile and 1.0 m into the cap.

3.3.4 Load Actuator

The test pile cap and reaction pile cap were connected by two hydraulic load actuators installed in parallel. Each actuator (manufactured by MTS Corporation) has a load capacity of 2.7 and 2.0 MN in compression and tension, respectively, and has a stroke of ±508 mm. The ends of the actuators are equipped with swiveling heads, creating a moment-free pinned connection. The two actuators were connected at mid-height of the test pile cap and reaction pile cap with four high-strength, threaded steel rods, installed in sleeves which extended the full length of the pile caps. The actuators were used to slowly push the test pile cap to predetermined displacement levels. The actuators were unable (and not intended) to apply a rapid cyclic loading due to the high levels of load required to initially displace the pile cap.

3.3.5 Eccentric Mass Shaker

The George E. Brown, Jr. Network for Earthquake Engineering Simulation (NEES) provided an eccentric mass shaker from the University of California Los

Angeles equipment site. The shaker (model MK-15 manufactured by ANCO Engineers) was mounted on top of the existing pile cap and anchored with chemically bonded, threaded steel rod embeedded in the pile cap. The eccentric mass shaker was used to create a cyclic, dynamic loading superimposed on the static loading provided by the actuators. The shaker has uni-directional force and frequency capacities of 445 kN and 25 Hz (but not at the same time). Due to safety concerns (potential loosening of the anchors), the shaker was operated during testing at levels not exceeding approximately 356 kN.

The force-frequency relationship for the shaker is controlled by the eccentricity provided by the configuration of its four baskets and their internal brick payloads. The equation relating force and frequency is given by Equation 14:

$$Force = u * 0.102 * (WR) * f^2/1000 \tag{14}$$

where force is expressed in kips, u is the loop amplitude in inches, and *f* is frequency in hertz, and WR is the total eccentricity of the weight and basket per basket in lb-in.

3.3.6 Instrumentation

Load and displacement were measured throughout the tests. Eight linear variable differential transducers (LVDT) were used to directly measure the displacement of the pile cap and reaction foundation as the actuator applied load. Triaxial-accelerometers were mounted on the pile cap to record cap motions.

Recorded accelerations where subsequently used to compute the relative displacement of the pile cap as it was shaken.

Load was measured directly by strain-gauge load cells built into the actuators. Pressure at the soil cap-interface was measured using four earth pressure cells and two thin-film tactile pressure sensors manufactured by Tekscan, Inc. The stainless steel earth pressure cells were 230 mm in diameter with capacities of at least 600 kPa. The cells were designed with a reinforced backplate to reduce point loading effects when directly mounting the cell to a concrete or steel structure, and the cells utilize a semi-conductor pressure transducer rather than a vibrating wire transducer to more accurately measure rapidly changing pressures. The earth pressure cells were recess-mounted, flush on the side of the pile cap. This was accomplished by removing existing concrete from the face of the pile cap to a diameter slightly larger than the pressure cell, and then embedding a template the same size as the pressure cell into a fast-set cement grout placed onto the underlying roughened surface. A smooth and intimate contact between the template and concrete was produced. After curing, the template was removed and a water-resistant sealant was applied to the underlying grout surface. The pressure plate was then installed in the recess created by the template and secured with 4 small anchors. Additionally, a vertical groove was cut into the face of the pile cap from the pressure cell location to the top of the cap to accommodate the stem and wiring of the pressure cells. To protect the pressure cell stem and wiring, a small steel pipe was cut in half lengthwise and secured over the groove.

The tactile pressure sensors are made of relatively thin polyester sheets embedded with semi-conductive material and measure pressures on a grid of approximately 10.2 mm spacing over a 530 mm wide and 490 mm high area. Horizontal and vertical sensing elements intersect at "sensels". The change in the resistance over each sensel determines the pressure acting on the sensor. Each tactile pressure sensor used in this testing contained 2016 sensels. An electronic handle was attached to each tactile sensor and was used to transfer data from the sensing pad to a laptop computer. Before being used in the field, the sensors were equilibrated and calibrated in the lab using a pneumatic bladder system. Ideally, the equilibration and calibration procedures should be performed using material that will be in contact with the tactile pressure sensor during field tests; however, this was not possible since the exact nature of the sensor-material interface depended upon the particular arrangement of soil particles which would be dictated by future soil placement and compaction conditions in the field. Separate experiments conducted with the sensor mounted between a concrete surface and fine to medium grained sand found that reasonable results could be achieve using the standard interface provided by the bladder system. With coarser material, however, the accuracy of the pressure measurements degraded as individual sensels were either point loaded by individual soil particles or not loaded at all, being in contact with the space between particles.

The pressure cells were centered at depths of approximately 216, 387, 716 and 876 mm below the top of the pile cap. The tactile pressure sensors were evenly spaced vertically along the height of the pile cap. To protect the handle of the lower tactile pressure sensor, a covered recess was made in the face of the pile cap. Small holes

were punctured along the outer edges of the tactile pressure sensors to allow entrapped air to escape during backfilling.

The data acquisition software allows the spatial pressure distribution to be viewed in real-time. A sample real-time window is shown in Figure 3-4. The figure shows the reading from the tactile pressure sensors immediately after the shaker run at 50 mm. Each small square in the figure represents a sensel on the tactile pressure sensor. (Due to the gray scale format of the figure some resolution in color is lost).

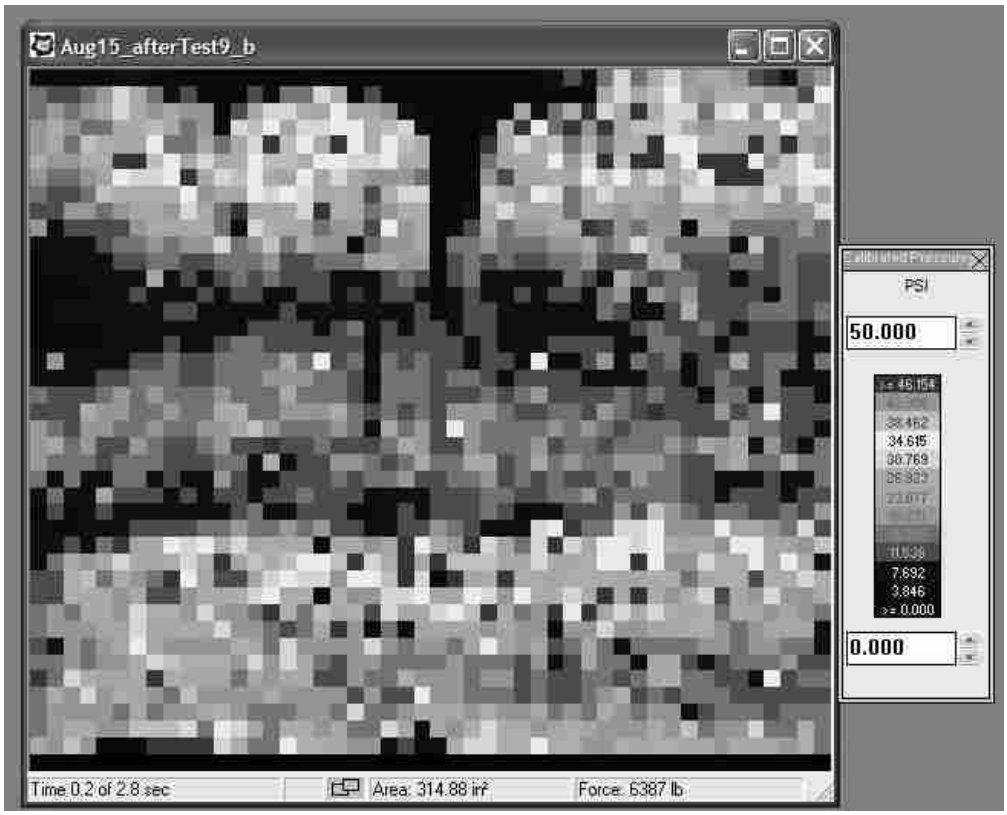

Figure 3-4 Sample Tekscan Real-Time Window

Instrumentation data was recorded using the NEES mobile field station and a laptop was used to collect data from the stand-alone tactile pressure sensors. The

NEES mobile station recorded data at 200 samples per second (sps), and the laptop recording the tactile pressure sensors recorded data at 100 sps. Figure 3-5 and Figure 3-6 show elevation and plan views of the test cap together with instrumentation and equipment. Figure 3-7, Figure 3-8, and Figure 3-9 show pictures of the actuators, backfill area, and pile cap instrumentation, respectively.

3.4 Dense Silty Sand Backfill

The silty sand backfill used in the pile cap test was the same material as that used in previous load tests by Cole and Rollins at the test site. A recently performed sieve analysis indicates that the silty sand has 5.6% gravel, 53.6% sand, and 40.8% fines as seen in Figure 3-10. The soil classifies as a silty sand (SM) according to the Unified Soil Classification System. The soil has coefficients of uniformity and gradation of 14.8 and 2.8, respectively.

As determined by Cole and Rollins and shown in Figure 3-11, the maximum dry density of the silty sand is 16.9 and 17.8 kN/m^3 for standard (ASTM D698) and modified (ASTM D1557) proctor compactive effort, respectively. The optimum moisture content for the silty sand is 16.8 and 13.6% for standard and modified proctor effort, respectively. The silty sand backfill was placed along the longer of the two pile cap dimensions (5.18 m) to a depth of approximately 0.3 m below the bottom of the pile cap. Horizontally, the backfill extended approximately 1 m beyond each edge of the pile cap and at least 4.9 m in front of the cap. The backfill was placed in 0.1 to 0.2 m-thick loose lifts and compacted using both a self-propelled, articulated vibratory tamping-foot compactor and a hand-operated rammer (i.e., jumping-jack)

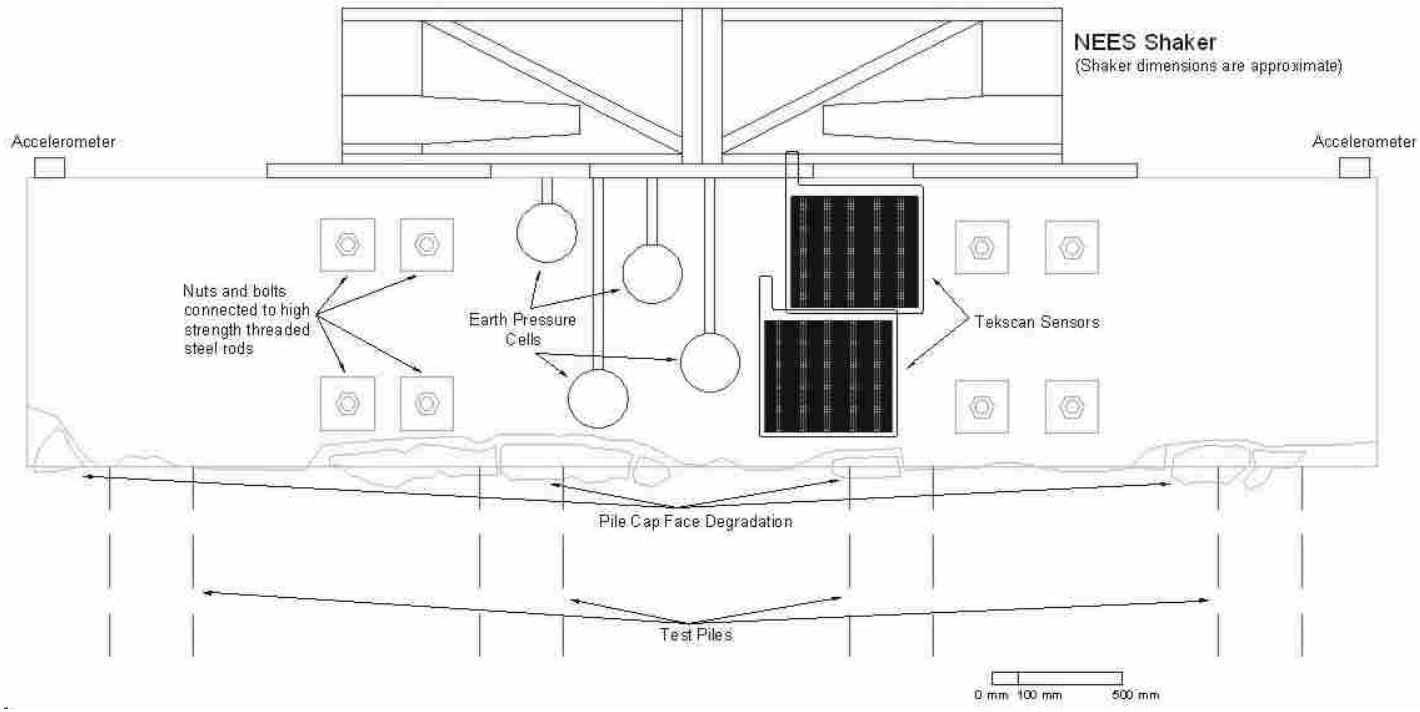

Figure 3-5 Elevation View of Pile Cap Face with Instrumentation

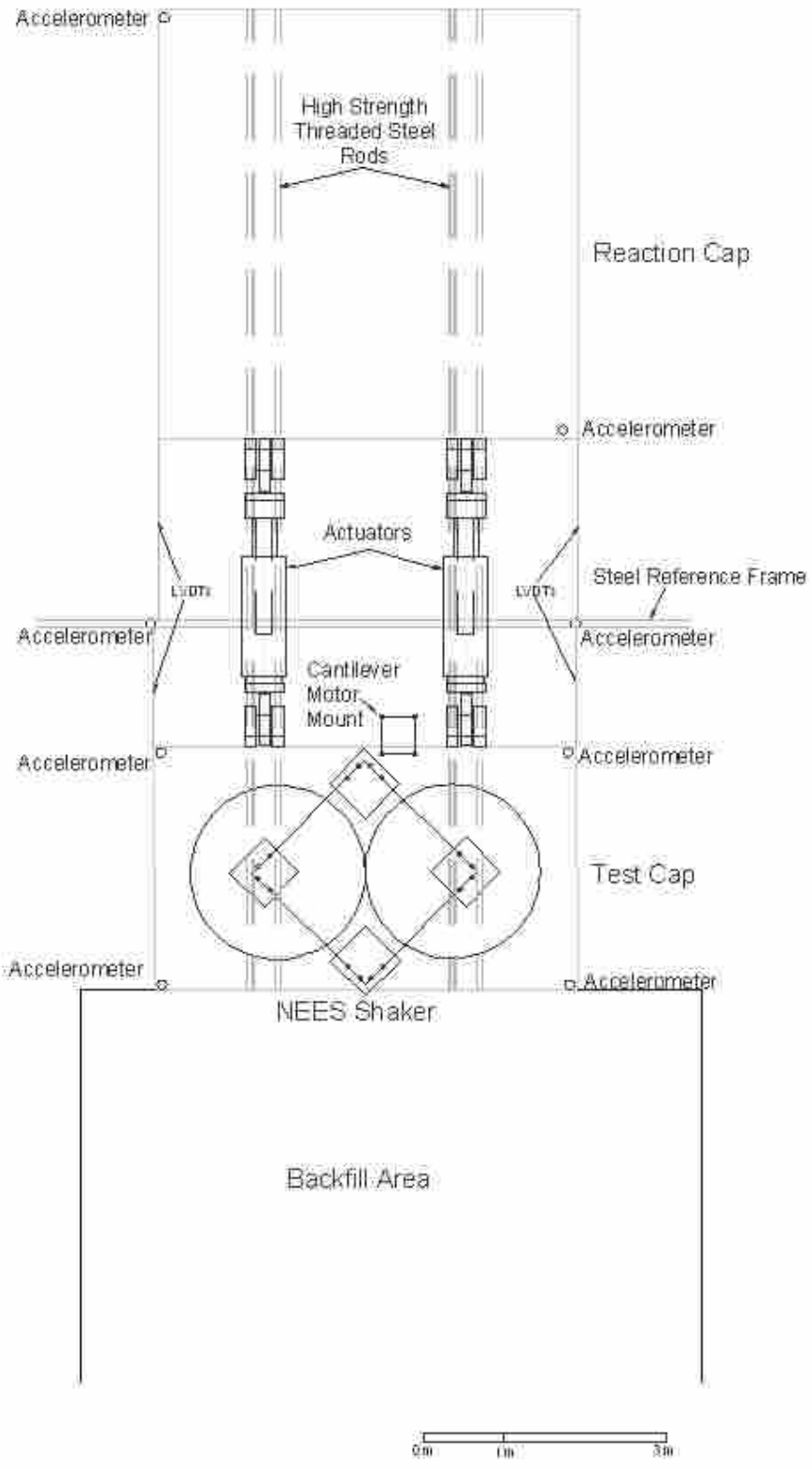

Figure 3-6 Plan View of Test Cap with Instrumentation and Equipment

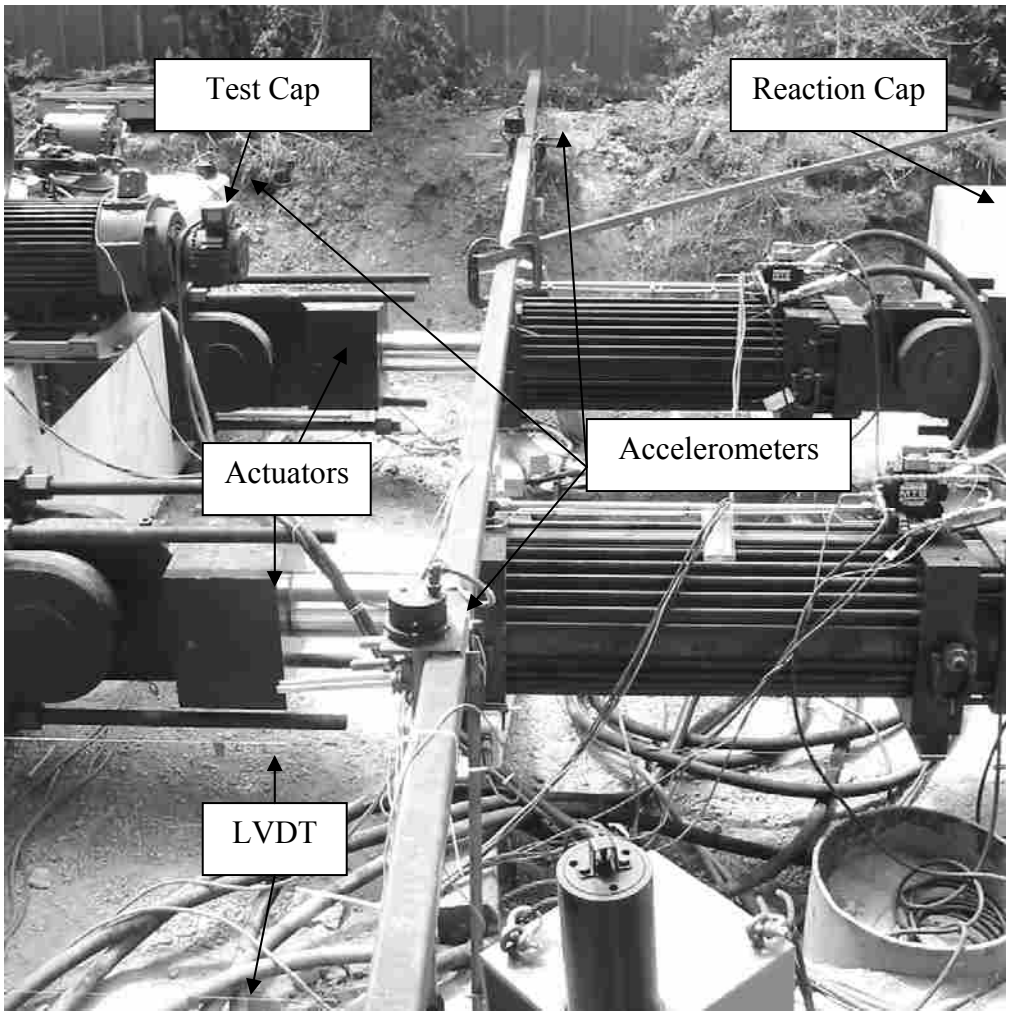

Figure 3-7 Equipment Setup between Test Cap and Reaction Cap

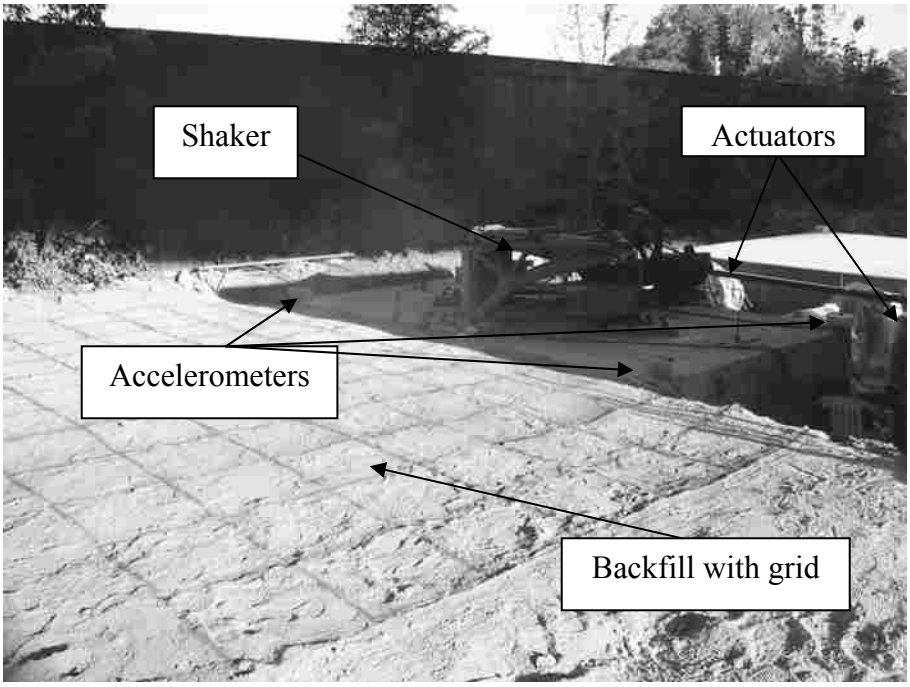

Figure 3-8 Test Setup in front of Test Cap

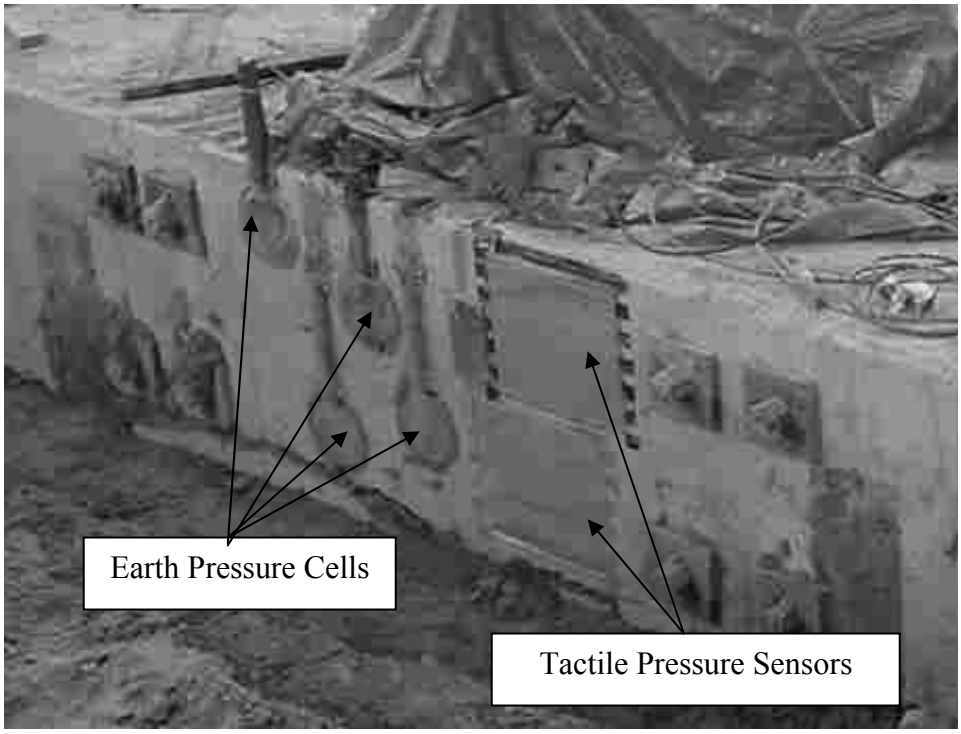

Figure 3-9 Instrumentation Setup on front of Test Cap before Backfill

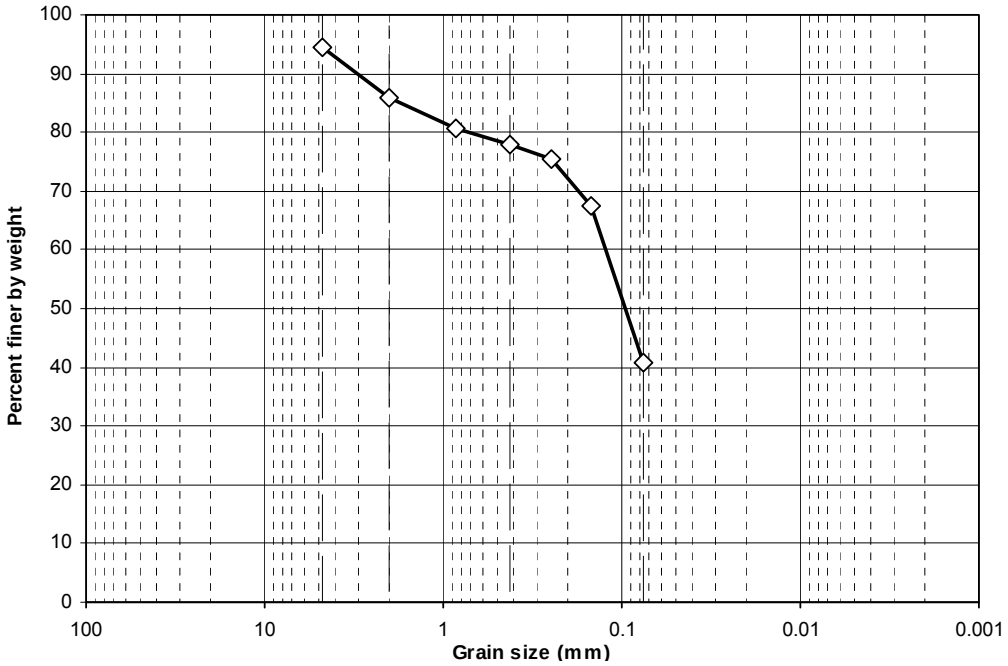

Figure 3-10 Average Grain Size Distribution for Silty Sand

compactors. The silty sand backfill material was compacted to a relatively dense state, representing an average density of 98% of the modified proctor moisture-density test (ASTM D1557). The resulting average dry density and moisture content of the in-place soil were 17.4 kN/m^3 and 10.7%, respectively. A histogram of compacted dry density is shown in Figure 3-12. Using geophysical measurements, Dr. Jim Bay of Utah State University determined the Rayleigh wave velocity of the dense silty sand backfill to be 130 m/sec (450 ft/sec).

Direct shear testing was conducted on the silty sand in the laboratory. Normal stresses are usually selected to be comparable with in-situ conditions, however, the normal stresses for these direct shear laboratory tests are higher than the vertical stresses one would expect in front of the pile cap due to limitations in the testing equipment. Test results showing shear stress versus horizontal deflection, as well as

shear stress versus normal stress, are presented in Figure 3-13 and Figure 3-14. Values for cohesion, c, and friction angle, φ, were found to be 17.4 kPa and 28.8 degrees, respectively.

An in-situ direct shear test was performed on the compacted backfill. The in-situ direct shear device consisted of a steel box, which was 0.46 m square by 0.23 m in height. The shear box was carved into place by creating a square soil column extending approximately 25 mm above the box surface. A steel plate was placed on the soil column, and normal forces were applied in predetermined increments. Shear force was applied using a hand operated bottle jack and measured with a proving ring. The shear box was horizontally displaced until a peak load was achieved. A greater normal load was then applied and the soil was sheared again. The in-situ direct shear test found cohesion and friction angle to be 7.1 kPa and 29.1, respectively. The in-situ direct shear results are presented in Figure 3-15.

3.5 Testing Procedures

Prior to testing, the front face of the test pile cap was backfilled with a silty sand material. The backfill was placed and tested with a nuclear density gauge. Upon completion of the backfill, data samples were taken from the earth pressure cells and tactile pressure sensors to get an initial at-rest passive pressure on the pile cap. The sequence of elements in the testing procedure was as follows. Without any load from the actuators (but with their length fixed between the test and reaction pile caps), the eccentric mass shaker was ramped from 1 Hz to a maximum frequency of 8 or 10 Hz. The shaker was allowed to dwell at each 0.5 Hz frequency increment for 10 to 20

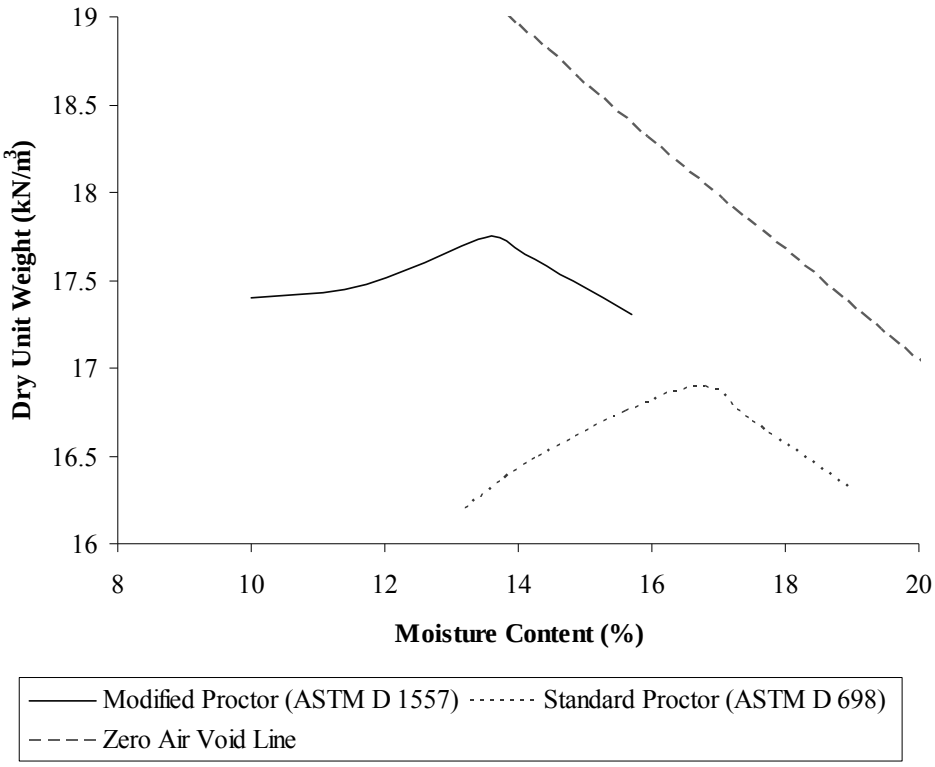

Figure 3-11 Compaction Curves for Silty Sand (after Cole, 2003)

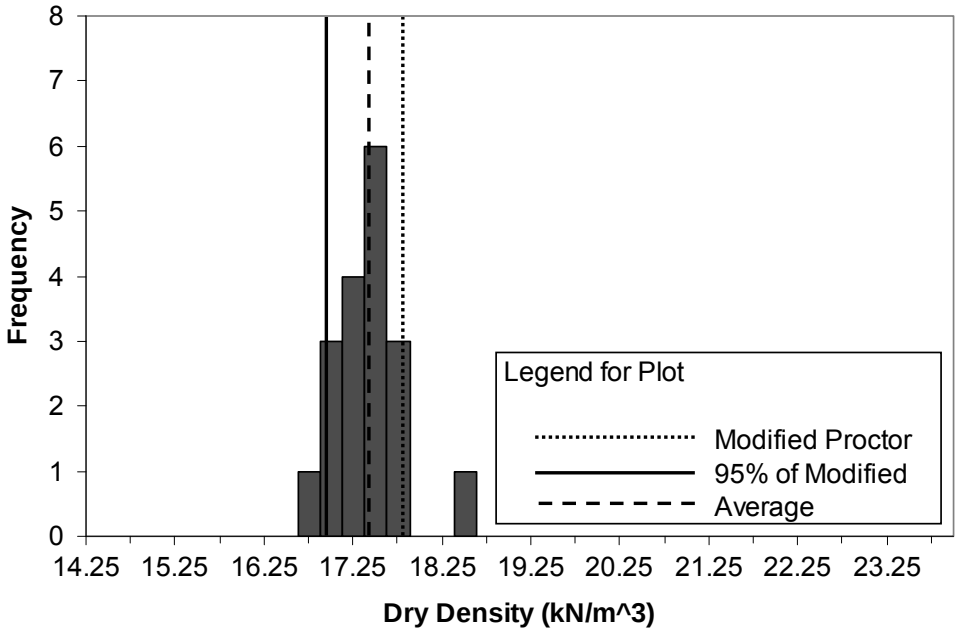

Figure 3-12 Compaction Histogram for Dense Silty Sand

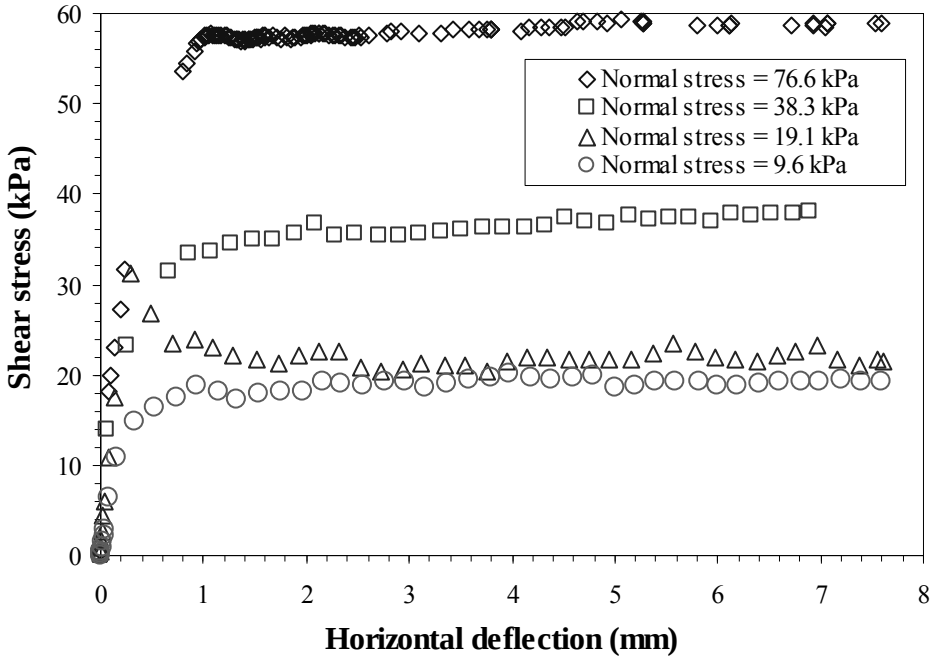

Figure 3-13 Shear Stress vs. Horizontal Deflection - Laboratory Direct Shear Test

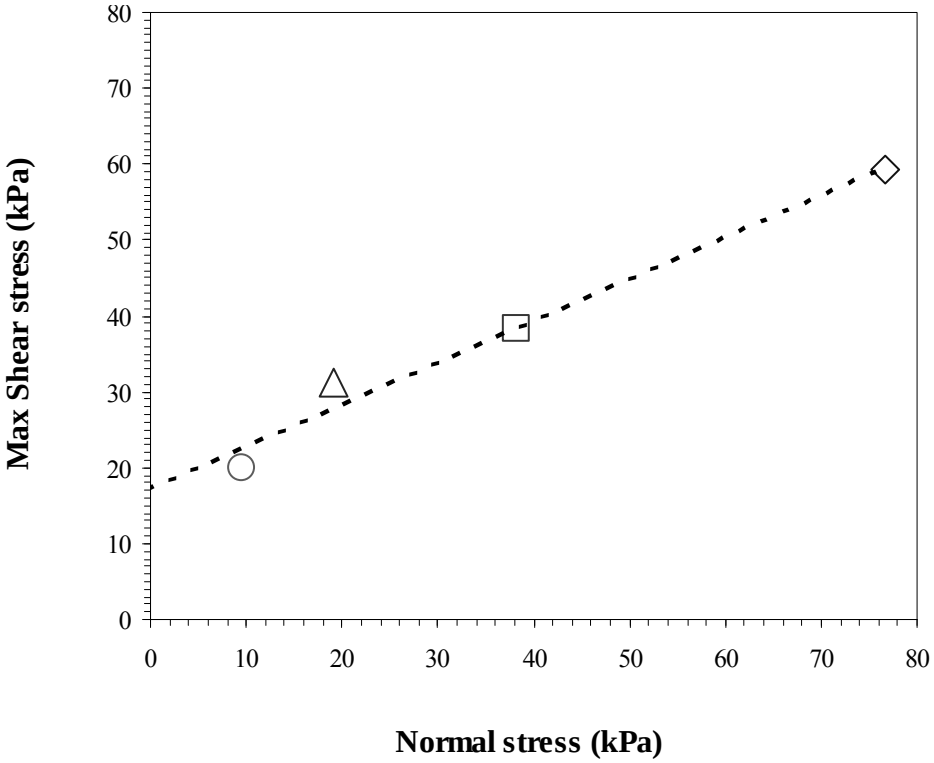

Figure 3-14 Shear Strength Envelope - Laboratory Direct Shear Test

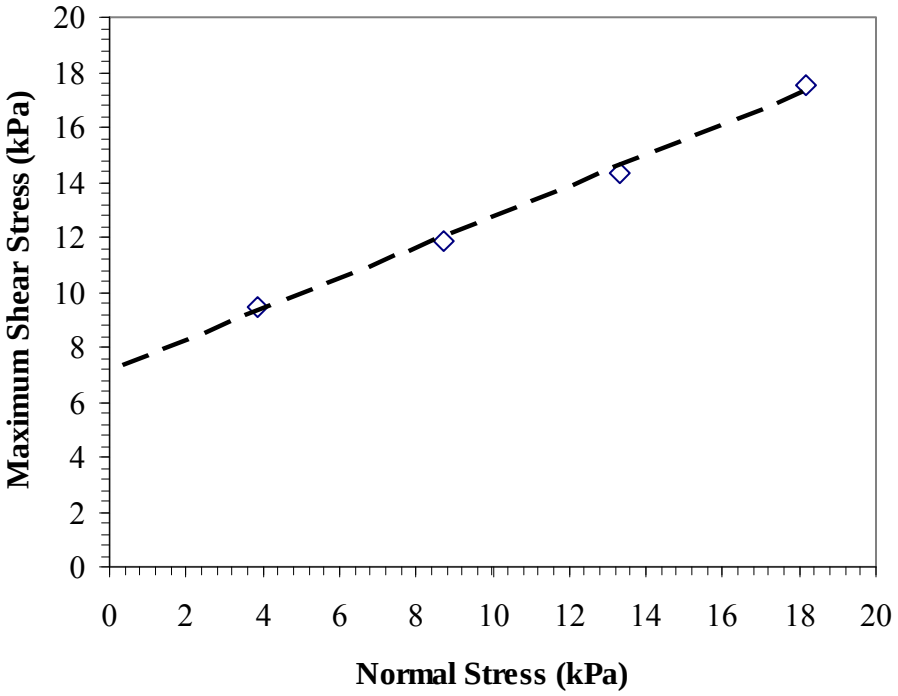

Figure 3-15 Shear Strength Envelope - In-situ Direct Shear Test

seconds. (This length of time would have ideally been much shorter, particularly at higher frequencies, but the shaker was limited to manual control due to loss of the controlling software program). This stepped-ramping procedure was followed for each use (or run) of the shaker. After the shaker had completed its run, the actuators were used to push the test pile cap to a target deflection of 6.35 mm, at which point the actuator lengths were again fixed. The shaker was then employed again. After each shaker run, the backfill was inspected and newly developed cracks were mapped. The sequence of a push by the actuators followed by a run of the shaker constituted an individual test. Each actuator push increased the pile cap deflection by about 6.35 mm, resulting in shaker runs at approximately the following static displacement levels:

6.35, 12.7, 19.1, 25.4, 31.8, 38.1, 44.5, and 50.8 mm. Two additional pushes with the actuator were made without running the shaker.

During the testing, two different basket configurations were used in an attempt to bracket the changing fundamental frequency. The first configuration involved two partially loaded baskets with a WR value (i.e., moment) of 6127 lb-in (692.2 kN-mm) each, resulting in maximum safe operating frequency of 8 Hz. This configuration was used for the first four static displacement levels. At higher displacement levels, a second configuration involving two partially loaded baskets with an eccentricity of 3984 lb-in (450.1 kN-mm) each was used, resulting in maximum safe operating frequency of 10 Hz. Table 3-1 shows the testing sequence for the pile cap with dense silty sand backfill (the primary focus of this thesis) performed on August 15, 2005. Table 3-2 shows the testing sequence for the pile cap without backfill.

Table 3-3 displays all of the backfill conditions tested during the field testing period. The test conducted on August 16 was used to define the baseline (i.e., no backfill in place) condition which was later used to isolate the effects of the backfill.

As stated previously, testing involved two actuators pushing the pile cap to specified deflections; however, it was soon apparent that the load data recorded by one of the actuators was incorrect. Several attempts by the testing crew as well as the actuator manufacturer were made to correct the situation, but to no avail. This malfunctioning actuator was applying load on the west side of test pile. Therefore, only load measured by the east actuator was used in the analyses presented in this thesis, and this actuator's measured load was doubled to account for approximate the load for both actuators. In doubling the load, it is assumed that both actuators applied

equal load to the pile cap. This assumption seems reasonable given that the LVDTs show the essentially the same amount of movement on the west and east sides of the test cap.

Table 3-1 Summary of Test Runs for Pile Cap with Dense Silty Sand Backfill

Test	Target Deflection (mm)	Actual Deflection (mm)	Maximum Frequency (Hz)
1	0	0	8
2	6.35	2	8
3	12.7	9	8
4	19.1	15	8
5	25.4	21	10
6	31.8	27	10
7	38.1	34	10
8	44.5	40	10
9	50.8	47	10
10	57.2	54	No Shaker Run
11	63.5	60	No Shaker Run

Table 3-2 Summary of Test Runs for Pile Cap without Backfill

Test	Target Deflection (mm)	Actual Deflection (mm)	Maximum Frequency (Hz)
1	0	1.3	7.5
2	6.35	4.9	8
3	12.7	11	8
4	19.1	17	8
5	25.4	23	10
6	31.8	30	9
7	38.1	36	9.5
8	44.5	42	9.5
9	50.8	49	9.5

Table 3-3 Summary of Pile Cap Backfill Conditions Tested

Date	Backfill Type	Comments
August 11, 2005	No Backfill	Test Equipment and Condition the Pile Cap
August 15, 2005	Dense Silty Sand	Compaction Target > 95% Mod. Proctor
August 16, 2005	No Backfill	Establish Lateral Resistance due to Piles
August 18, 2005	Loose Silty Sand	Compaction Target = 85-90% Std. Proctor
August 24, 2005	0.91m Wide Gravel Trench	Trench Compaction > 95% Mod. Proctor, Loose Silty Sand Beyond Trench
August 26, 2005	1.83 m Wide Gravel Trench	Trench Compaction > 95% Mod. Proctor, Loose Silty Sand Beyond Trench

4 Test Results and Interpretation

4.1 Overview

This section presents and discusses the lateral load test results for the pile cap both with and without a dense silty sand backfill in place. First the total system resistance (i.e., piles and cap with backfill) is addressed first, followed by the baseline resistance of the system (i.e., piles and cap without backfill). Afterward, the resistance provided by the backfill itself will be addressed. The last section of this chapter will discuss the dynamic damping and stiffness of the test cap with and without backfill, and of the backfill itself.

4.2 Resistance of the Pile Cap with Dense Silty Sand Backfill

Figure 4-1 shows the load-displacement relationship obtained for the pile cap with the dense silty sand backfill. In this figure, relative displacement is based on LVDTs (i.e, string potentiometers). Because of this, displacement within the dynamic, cyclic loading loops are overestimated since it includes additional dynamic movement of the reference frame (this is also why the loops appear large and irregular). Also in this figure, load is based on the measured (doubled) actuator load. Hence, the load shown as a thinner line between the thicker appearing dynamic, cyclic loading loops is

the “static” resistance of the pile cap system together with any backfill. Within the loops, however, both shaker and inertial loads must be combined with the actuator load to determine the complete dynamic resistance of the system.

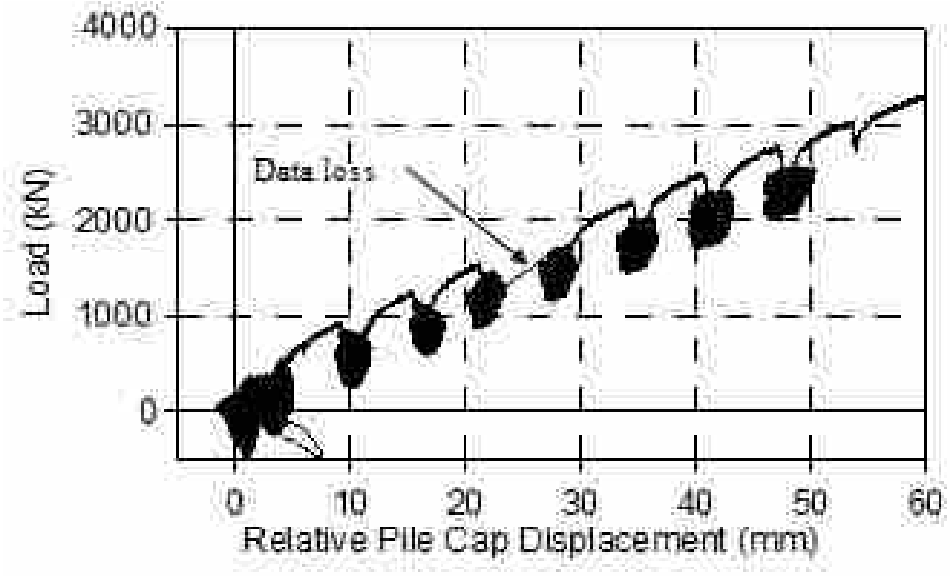

Figure 4-1 Load-Displacement Response of Pile Cap with Dense Silty Sand

In the figure, it is seen that there is a decrease in resistance as the shaker run progresses, but the load is quickly recovered after the shaker stops and the actuators push the pile cap to a new deflection level. More careful inspection of the load-displacement curve shows that there is a loss of load resistance after the actuators have pushed the pile cap to the next displacement level and before the eccentric mass shaker is operated. This “relaxation” is more clearly illustrated in Figure 4-2, which shows load and displacement time histories from Test 4 of the dense silty sand backfill case. The relaxation exhibited in other test segments is similar. In this figure, time has been zeroed for simplification purposes and does not represent the beginning of

the dense silty sand backfill test. Also, the data has been filtered to 1 sps, causing the oscillations in load and deflection during shaker operation to not be clearly seen.

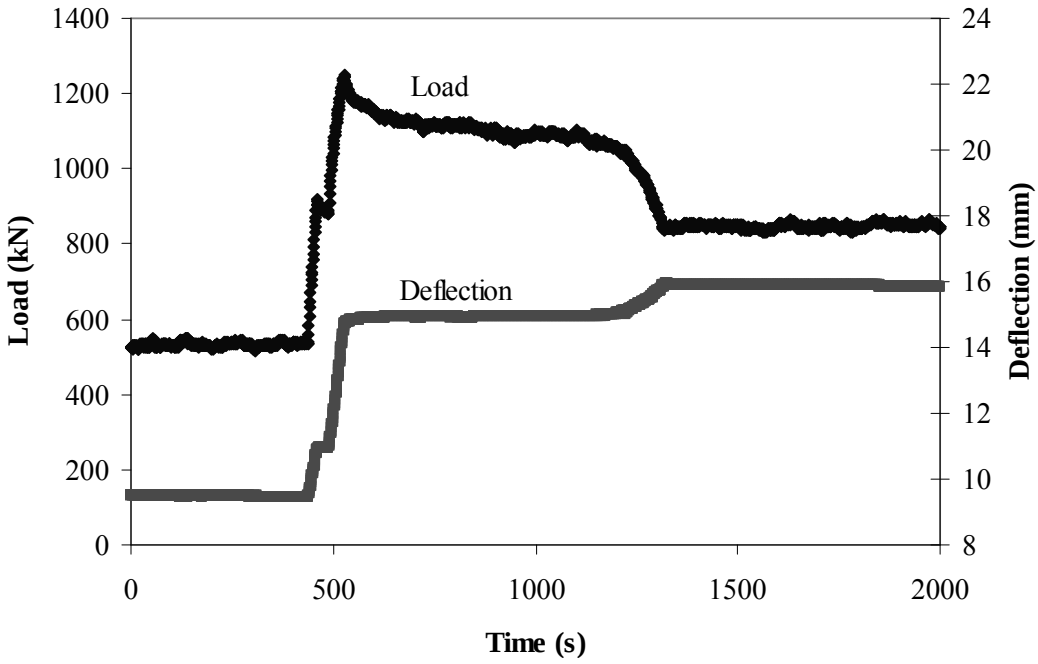

Figure 4-2 Time History of Load and Deflection During One Test Segment

The plot starts at the beginning of a push by the actuators to the new static deflection level. Load and deflection continue to increase and then both reach a peak when the actuator stops pushing the cap. Afterwards, the actuator holds the pile cap at the specified deflection level (i.e., there's no backwards movement), but the load begins to decrease. A ramped loading with the shaker then begins at approximately 1000 seconds. At approximately 1200 seconds, a sharp decline in load is evident while the overall deflection of the pile cap increases. This point occurs approximately at a loading rate of 5 Hz and is likely due to degradation due to cyclic loading and lower peak displacement amplitudes after exceeding the resonant frequency of the pile

cap system. The earlier decrease in load as the deflection is held constant shows a relaxation in the soil. The relaxation can be attributed to both the backfill and the soil surrounding the piles losing strength as the deflection is held constant by the load actuators. Immediately after a static push, the peak load will consequently be higher than the peak dynamic loads experienced during a shaker run. Table 4-1 quantifies the amount of load loss due to soil relaxation. In terms of absolute values, the approximate relaxation load loss increases with increasing deflection at low deflection levels and then levels off at 31 mm.

Table 4-1 Approximate Load Loss Due to Relaxation

Test	Deflection (mm)	Approx. Load Loss Due to Relaxation (kN)
1	0	N/A
2	6	61
3	13	130
4	19	174
5	25	202
6	31	274
7	38	260
8	44	248
9	50	269

Figure 4-3 presents a summary plot the load-deflection relationship for the pile cap with dense silty sand backfill in which the load at it's peak value for each static deflection level (i.e., at the end of the actuator push) is shown as a continuous curve. Also shown in the figure is the load after it undergoes relaxation just before the shaker is started and the load at the end of the ramped shaker loading (i.e., post-cycling). The three curves illustrate the effects of soil relaxation and dynamic, cyclic effects. The

soil relaxes from the peak deflection to immediately before the shaker run, as evident in the decrease in load at each deflection level from the peak curve to the relaxation curve. A much larger difference is seen in comparing the post-cycling curve with the peak curve. This difference appears to be relatively constant throughout the test. The change in load between the relaxed and post-cycling values is caused by the dynamic and cyclic effects produced by the shaker run.

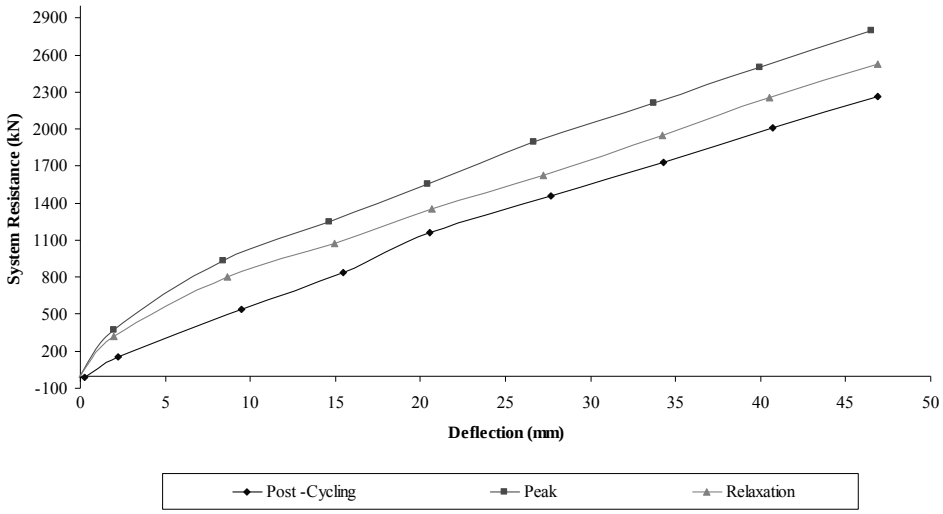

Figure 4-3 Load-Deflection Curves based on Peak, Relaxed, and Post-Cycling Load

The change in load is illustrated in Figure 4-4 as a percent of the peak load. The load degradation caused by dynamic, cyclic effects is more significant at lower deflections, but gradually becomes somewhat constant. The peak versus relaxed load curves tends to stay fairly constant throughout the deflection levels.

Figure 4-5 shows load deflection curves as a function of shaker frequency. The static peak, relaxation, and post cyclic load deflection curves are superimposed upon the frequency-based load deflection curves. As discussed earlier, a loss in load

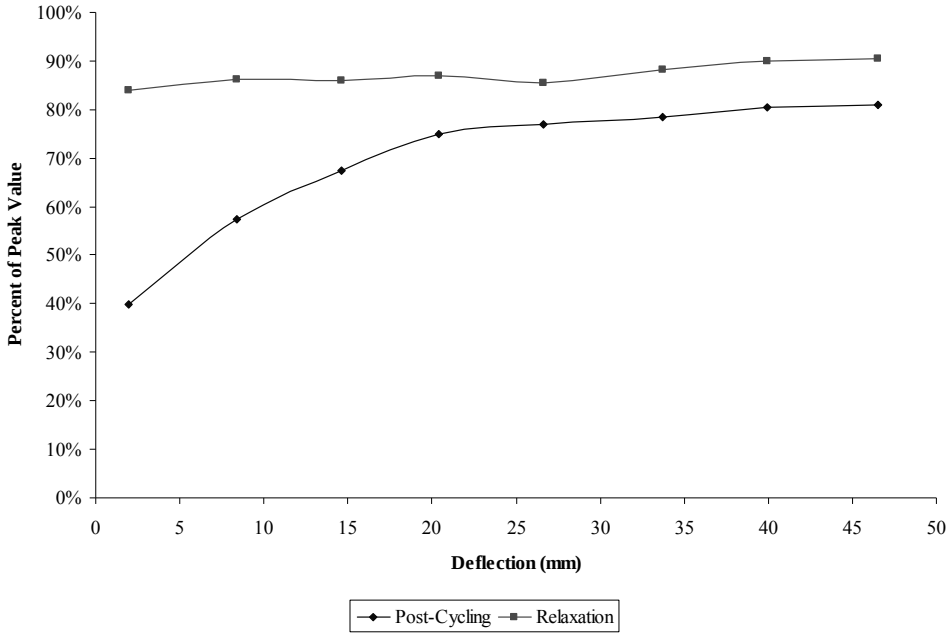

Figure 4-4 Load Degradation due to Relaxation and Dynamic, Cyclic Effects

due to relaxation occurs between the peak (end of static push) and the starting of the shaker. The loads used for system resistance by frequency are the average loads over 20 hysteresis loops for each frequency level. The figure shows that as frequency increases resistance decreases. Degradation is most notable at low deflection levels. Load degradation becomes more constant at high deflection levels. Load degradation is mainly attributed to dynamic, cyclic effects but could also be due to gapping and subsurface relaxation. In this data, the loss in resistance per load cyclic at discrete frequency levels is difficult to quantify due to the continuously ramped nature of the shaker loading. The median dynamic displacement amplitude, u_0, for each frequency and static displacement level is presented in Figure 4-6. These values were calculated using the first 20 hysteretic load-deflection loops after the shaker reached the target frequency. The curves increase in static displacement in 6.35 mm increments from

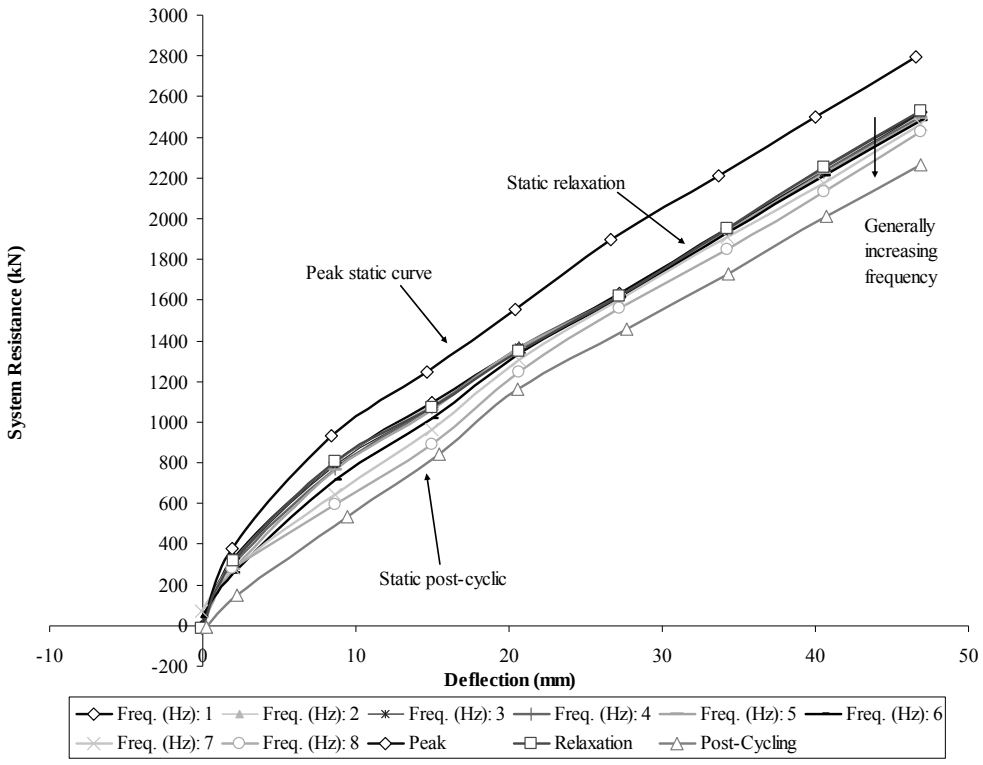

Figure 4-5 Relaxation Effects and Dynamic, Cyclic Effects on Total Passive Resistance as a Function of Frequency

left to right starting from 0 mm for the curve furthest to the left. A change in shaker basket weight is responsible for the abrupt change in displacement amplitude after the 19.1 mm deflection level. The figure shows that dynamic displacement amplitude increases with increasing frequency (and hence shaker force since it is a function of the square of frequency). The maximum dynamic displacement amplitude indicates the approximate damped natural frequency of the system. At zero deflection, the damped natural frequency appears to occur between 6.5 and 7 Hz. The damped natural frequency begins to shift to higher values and is not clearly bracketed at the next three deflection levels prior to changes in the shaker basket configuration. In

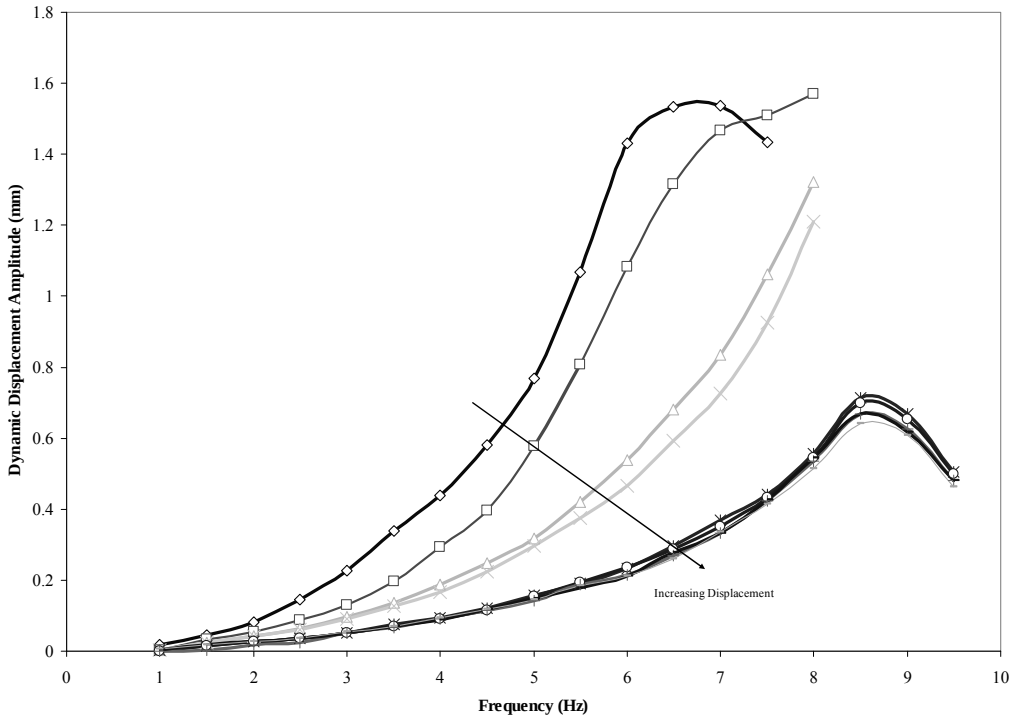

Figure 4-6 Dynamic Displacement Amplitude as a Function of Frequency and Static Displacement Level

subsequent tests at higher levels of static deflection, it is seen that the damped natural frequency increases to approximately 8.5 Hz. Beyond the resonant frequency, the maximum dynamic displacement amplitude decreases with increasing frequency. This reduction is expected in part due to the dynamics and the displacement response of objects vibrating above their natural frequency. Rather than being the response of the test cap by itself, this plot exhibits the superimposed effects of the test cap and the reaction cap behaving as a system.

Figure 4-7 plots the relationship between load (system resistance) and dynamic displacement amplitude. Solid lines represent these relationships as a function of forcing frequency whereas the dotted lines represent these relationships as a function of static displacement level. In this figure, the effects of inertia and the shaker loading

have been combined with the actuator loads (the particulars of the process are described later) to determine the total resistance to horizontal displacement provided by the piles and the dense silty sand backfill during dynamic, cyclic loading.

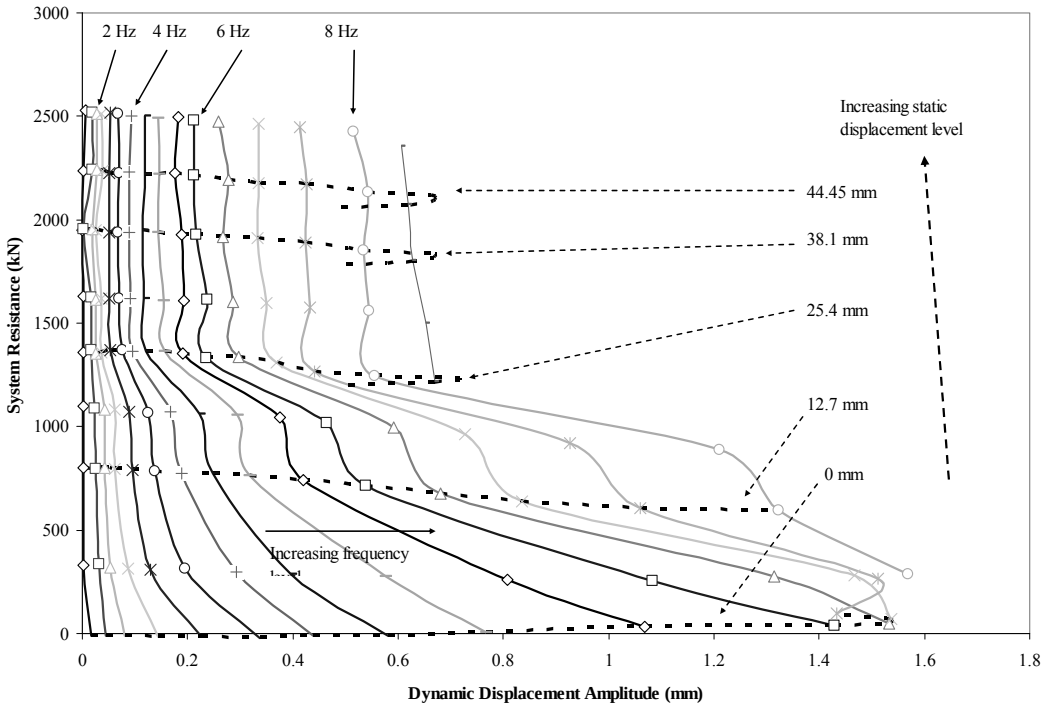

Figure 4-7 System Resistance Versus Dynamic Displacement Amplitude

In interpreting this figure, it should be remembered that frequency is coupled with the dynamic load applied by the shaker, and hence frequency is not truly independent of dynamic displacement because both are related to the load resistance of the system. As seen in the figure, system resistance increases with static displacement level and is accompanied by a decrease in dynamic displacement amplitude. It is also seen that, generally, load resistance slightly decreases with increasing dynamic displacement amplitude and frequency. This suggests that either the soil is behaving non-linearly at these small displacement levels, or that cyclic

effects which degrade resistance are more prominent than rate loading effects which tend to increase resistance or that resist.

4.3 Resistance of the Pile Cap without Backfill (Baseline Response)

Figure 4-8 shows the load-deflection relationship for the pile cap without any backfill present. This figure is similar to Figure 4-1 which shows the load-deflection relationship for the pile cap with the dense silty sand backfill. The load shown in Figure 4-8 is the lateral load resistance provided by the piles and the passive soil interaction. This resistance is also referred to as the "baseline response." The difference between Figure 4-1 and Figure 4-8 is the effect of the backfill. In comparing Figure 4-1 and Figure 4-8, it is seen that the dense silty sand backfill provides a significant increase in load resistance, being nearly doubled at a deflection of 50 mm.

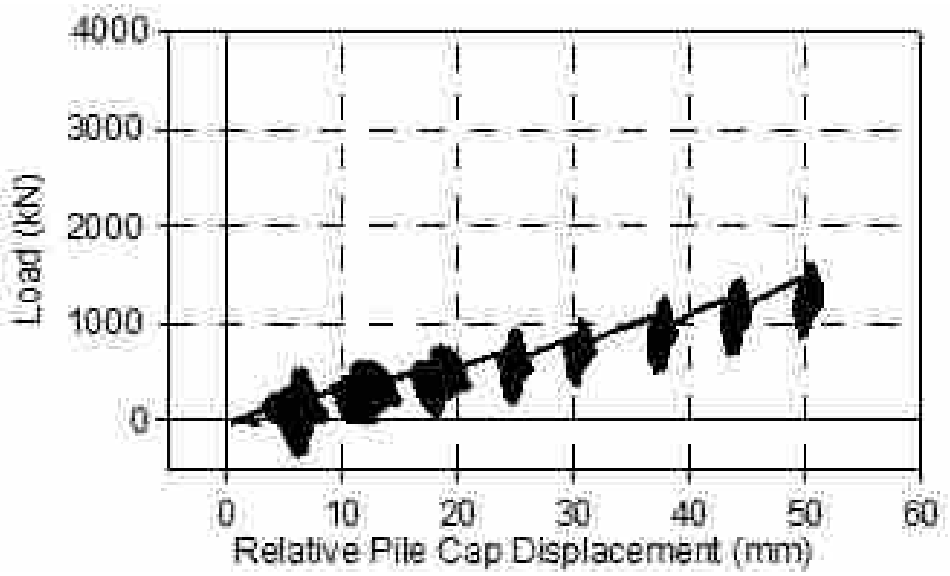

Figure 4-8 Load-Displacement Response of Pile Cap without Backfill

The baseline response shown in Figure 4-8 is quite linear. Since there was significant gapping under the cap from testing conducted prior to 2005, the resistance is entirely from pile-soil interaction and not any interaction with the base of the cap and underlying soil. A best fit line drawn through the peak loads at the end of each actuator push to new static deflection levels has a slope of approximately 27 kN/mm.

The slopes of the load-displacement responses of the cap as it was pulled from its peak deflection level back to zero load at the end of each backfill condition were examined to assess the consistency of this baseline response of 27 kN/mm. These "pull-backs" represent the passive contribution due to the piles only. Figure 4-9 shows pull-backs recorded from the backfill cases involving dense silty sand and a 0.91 m wide gravel trench adjacent to loose silty sand. Also shown in the figure is the simplified load-displacement curve based on the ends of the actuator pushes during loading for the no backfill test as well as its pull-back. The beginning portions of the pull-backs are shown by a curve in the load deflection relationship. The pull-back load deflection gradually changes from a curve into an approximate linear relationship. The curved portion of the pull-backs results from the decreasing soil pressure from the backfill as the pile cap is pulled away from the backfill. The slope becomes linear once a complete gap between the cap and backfill has formed. The similarity of the slopes validates that the baseline response was consistent during testing.

Figure 4-10 shows the pull-back portion of the load-displacement curve for the cap with dense silty sand backfill. The two curves are based on loads based on both earth pressure cells and load actuators. The slopes at the end of the curve seem to

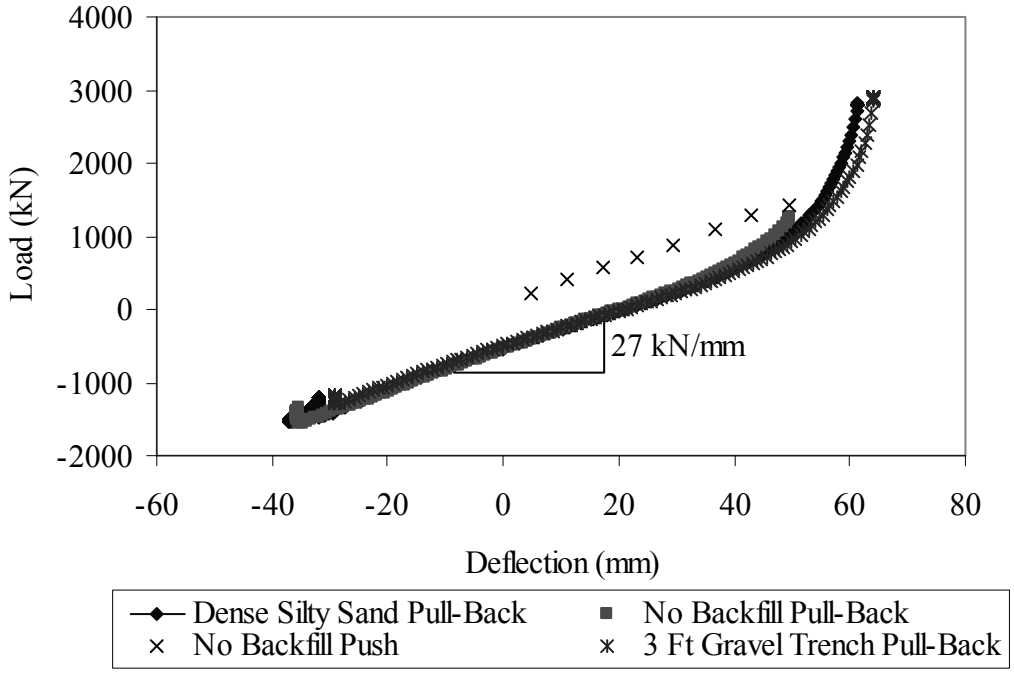

Figure 4-9 Load-Displacement Response During Pull-Backs and Loading Without Backfill

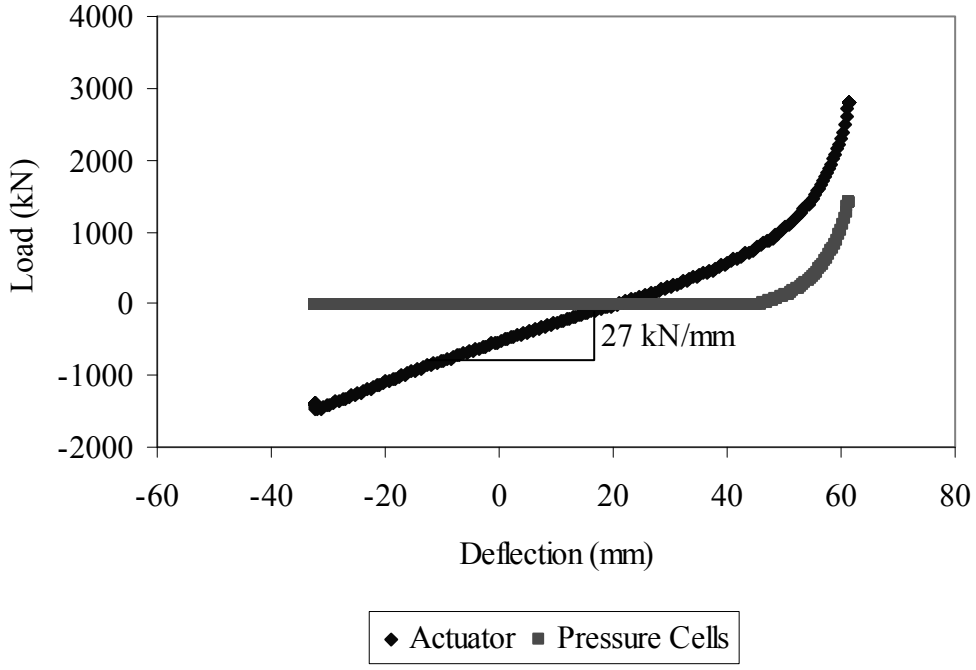

Figure 4-10 Load Based on Pressure Cells and Actuators During Unloading of the Pile Cap

follow the same slope, and when the slope of the actuator curve becomes linear, the slope of the earth pressure cell curve goes to zero. This point indicates where the backfill is no longer acting on the cap.

Figure 4-11 shows load deflection curves as a function of shaker frequency. The static peak, relaxation, and post cyclic load deflection curves are superimposed upon the frequency-based load deflection curves. As discussed earlier, a loss in load due to relaxation occurs between the peak (end of static push) and the starting of the shaker. The figure also shows that as frequency increases resistance decreases with the decrease being most notable at low deflection levels. Load degradation is mainly attributed to dynamic, cyclic effects but could also be due to gapping and subsurface relaxation. In comparing this figure with Figure 4-5 (which represents the case with backfill in place), there is less loss in resistance between the relaxed and post-cycling states, suggesting that the backfill is more prone to strength degradation than the soils surrounding the piles. This makes sense considering that the backfill has a finite contact depth with the cap whereas deeper subsurface soils can provide resistance along the pile length after more shallow subsurface soils have gapped and/or lost strength. The backfill soil is also granular whereas the subsurface soils are primarily plastic clayey below the water table.

Figure 4-12 shows the median dynamic displacement amplitude, u_0, for each shaker frequency and static displacement level. Again, the curves increase in static displacement in 6.35 mm increments from left to right starting from 0 mm for the curve furthest to the left. As was the case with the dense silty sand backfill, a change

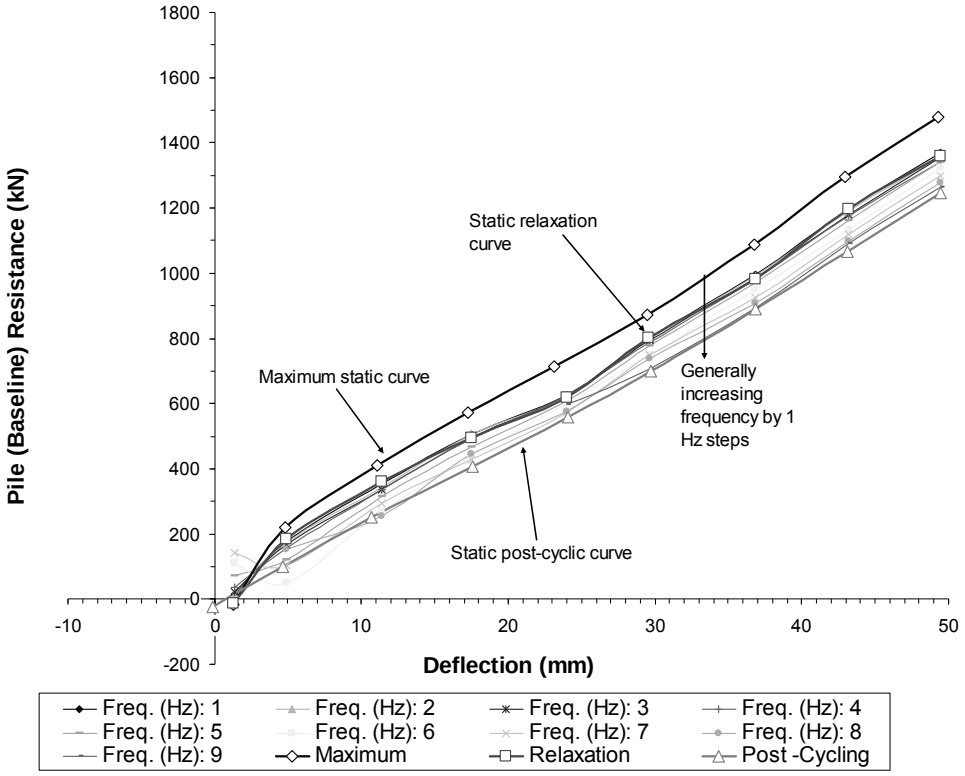

Figure 4-11 Relaxation Effects and Dynamic, Cyclic Effects on Total Passive Resistance as a Function of Frequency

in shaker basket weight is responsible for the abrupt change in displacement amplitude after the 19.1 mm deflection level. As expected, a comparison of this figure with Figure 4-6 for conditions with backfill present shows that dynamic displacement amplitude increases without the backfill present. The displacement response for the no backfill case is notably bi-modal as compared with conditions with the dense silty sand backfill in place. This is presumably as a result of test pile cap now having a lower fundamental frequency than the reaction pile cap due to the missing backfill. At zero deflection, the damped natural frequency appears to occur around 5.5 Hz. The damped natural frequency begins to shift to higher values with increasing deflection levels with resonance occurring at approximately 6 Hz. Beyond the resonant

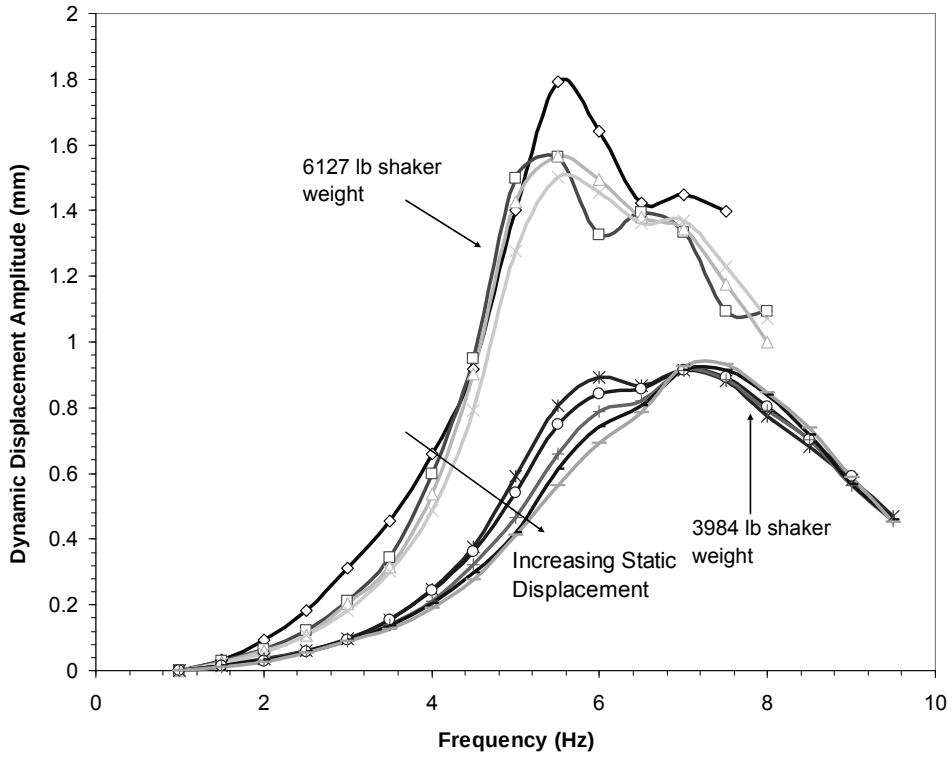

Figure 4-12 Dynamic Displacement Amplitude as a Function of Frequency and Static Displacement Level

frequency, the maximum dynamic displacement amplitude decreases with increasing frequency. This reduction is expected in part due to the dynamics and the displacement response of objects vibrating above their natural frequency, despite the larger shaker load accompanying the higher frequencies.

Figure 4-13 plots the relationship between load (system resistance) and dynamic displacement amplitude. Solid lines represent these relationships as a function of forcing frequency whereas the dotted lines represent these relationships as a function of static displacement level. As seen in the figure, system resistance increases with static displacement level and is accompanied by a decrease in dynamic displacement amplitude. It is also seen for the no backfill case with some static

displacement that load resistance is essentially constant with increasing dynamic displacement amplitude and frequency, which indicates that cyclic and rate loading effects are negligible or offsetting.

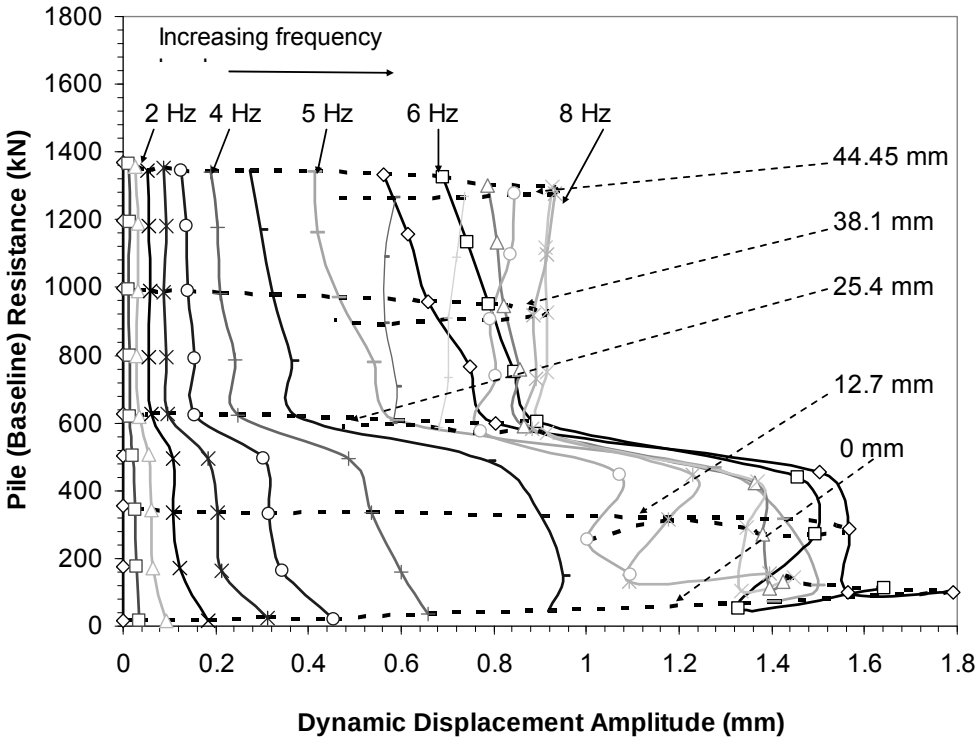

Figure 4-13 System Resistance Versus Dynamic Displacement Amplitude

4.4 Passive Resistance of Dense Silty Sand Backfill

4.4.1 Resistance Based on Load Actuators

Figure 4-14 provides load-deflection curves based on the total resistance of both the backfilled pile-cap system and pile-cap system without backfill (i.e., the baseline response). The curves are based on the *peak* loads at the end of the load actuator pushes. The baseline curve has been idealized based on a constant slope of

27 kN/mm as explained above. Also, the baseline curve is shifted approximately 6.3 mm. This shift can be seen in Figure 4-14, where the baseline curve begins at approximately -175 kN. Ideally, both curves should coincide at a displacement of zero (at least if at-rest earth pressure is neglected as is commonly the case with p-y curves). During testing, however, it was observed that the test pile cap had a tendency to creep after being pulled back from its maximum static displacement to zero applied load. The pile cap also moved from its initial starting point in response to placement and compaction of the backfill. Consequently there was some uncertainty as to how the initial points of the two load-displacement curves should correspond. Previous test results from Cole and Rollins using the same backfill conditions was consulted in order to help determine the appropriate location (i.e., amount of shift) of the two curves relative to each other. A comparison between the baseline response in their tests and those in this current study revealed that the current tests indicate a significantly less stiff baseline response. This difference is attributed to differences in ground water conditions and the last test of Cole and Rollins in which the pile cap was deflected well beyond previous levels and likely degrading the stiffness of the pile-to-cap connections. Despite this change in the baseline, the net backfill resistance should be the same for both sets of tests. Also, the resistance of the backfill can be estimated based on the soil pressure cells. Both the passive earth resistance curves from Cole and Rollins as well as the passive earth resistance calculated from the pressure cells was used to determine the shift used in the baseline. (As shown later, the passive earth resistance curves from Cole and Rollins as well as the passive earth resistance calculated from the pressure cells are in good agreement). It should be kept in mind

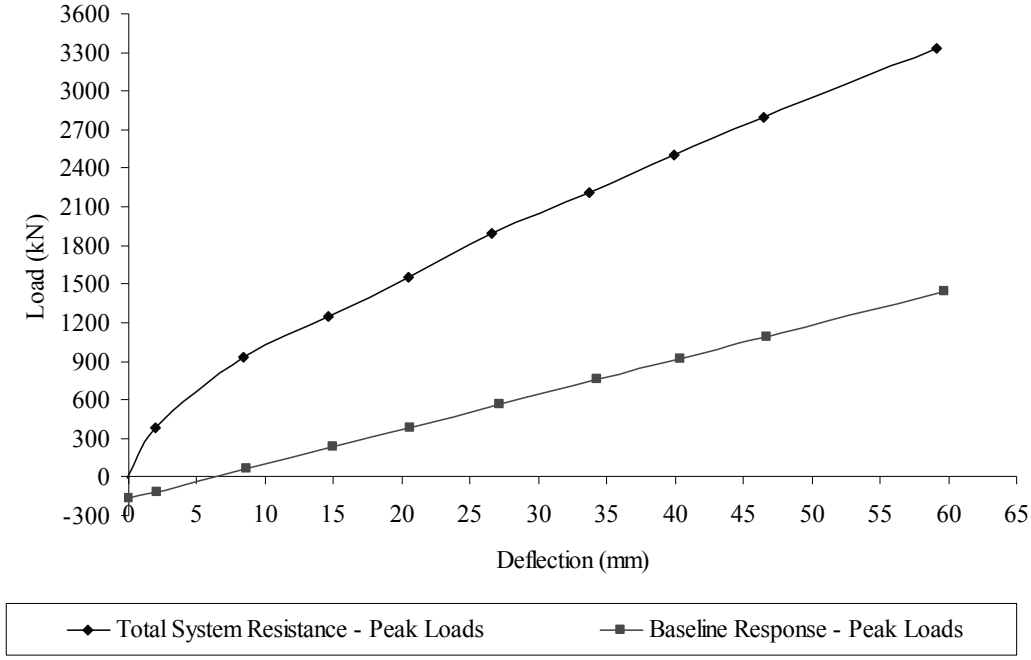

Figure 4-14 Load-Deflection Curves for Pile Cap with and without Dense Silty Sand Backfill Based on Peak Loads

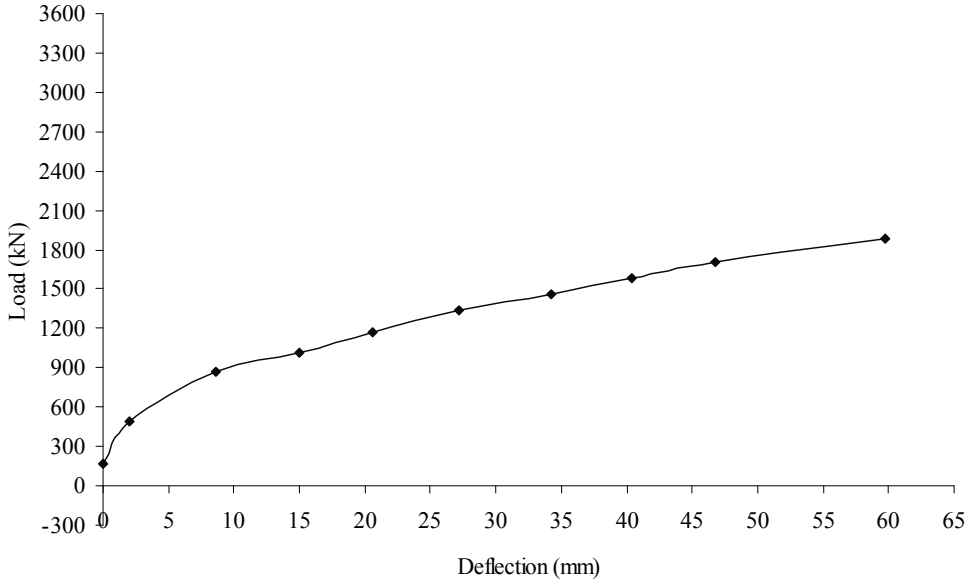

Figure 4-15 Resultant Passive Earth Load-Deflection Curve for Dense Silty Sand Backfill Based on Peak Loads

that with this shift, the initial portion of the load-displacement backfill resistance curves will show a non-zero value. Also, the idealization of the baseline response at a constant slope may become less valid at large deflection levels.

The difference between the two curves shown in Figure 4-14 represents the contribution of the dense silty sand backfill to the total system resistance. When the slopes of the two curves become parallel, the backfill soil has failed and cannot contribute more resistance. The resultant passive earth load (force) – deflection relationship for the dense silty sand backfill is shown in Figure 4-15.

Figure 4-16 provides load-deflection curves based on the total resistance of both the backfilled pile-cap system and pile-cap system without backfill after the soil has relaxed from its peak value. In this case, the baseline response is shifted -82 kN to account for the loss in load due to relaxation of the no backfill case. The resulting passive earth load (force) – deflection relationship is shown in Figure 4-17. Because the tests of Cole and Rollins used jacks which applied load much more slowly than the actuators (this allowing time for the soil to undergo relaxation (or delayed compression) as the soil is loaded), it is believe that the curve shown in Figure 4-17 is the one to which comparisons involving the results of their tests should be made.

4.4.2 Backfill Resistance Based on Earth Pressure Cells

Both static and dynamic passive pressures from the dense silty sand backfill acting on the pile cap were measured using four 230 mm in diameter earth pressure cells embedded flush in face of the pile cap. The soil pressure distributions measured with depth below the top of the pile cap for each static displacement level are shown

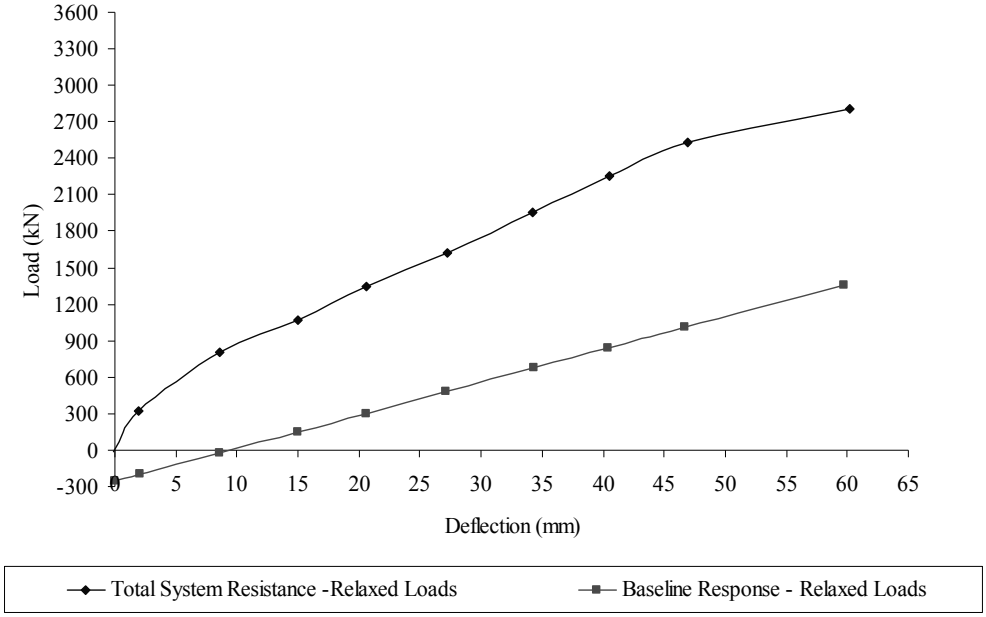

Figure 4-16 Load-Deflection Curves for Pile Cap with and without Dense Silty Sand Backfill Based on Relaxed Loads

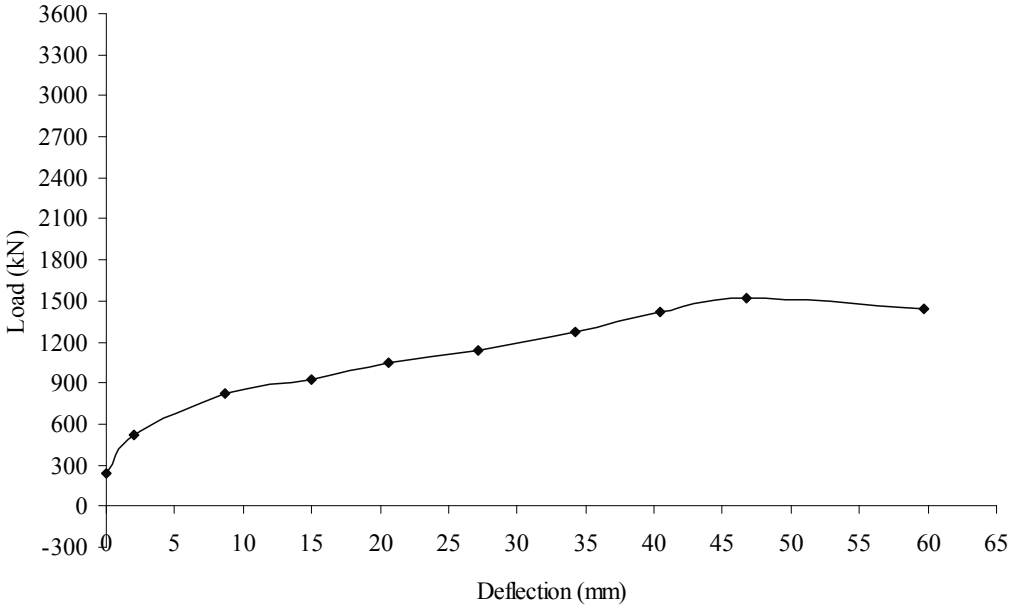

Figure 4-17 Resultant Passive Earth Load-Deflection Curve for Dense Silty Sand Backfill Based on Relaxed Loads

in Figure 4-18. It is seen that these static passive pressure distributions are non-linear, with most of the pressure being exerted on the bottom of the pile cap, despite practically negligible rotation of the cap (any rotation appears to occur at the top rather than the bottom).

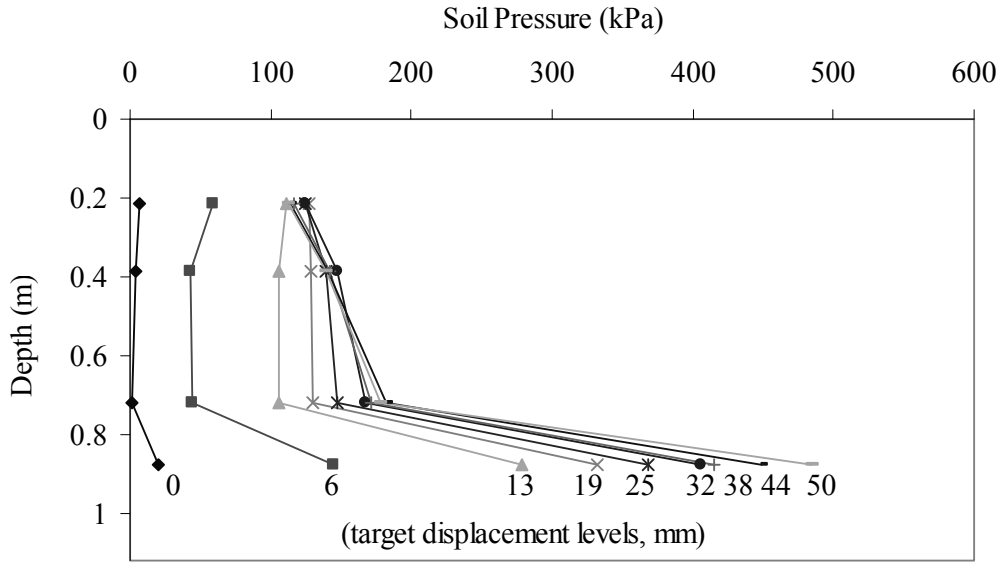

Figure 4-18 Earth Pressure Distributions Based on Pressure Cells – Static, Relaxed Load Conditions

Figure 4-19 and Figure 4-20 present the maximum and minimum dynamic pressure distributions, respectively, along the face of the pile cap measured by the pressure cells. Maximum and minimum pressure values were picked for the first and fifteenth cycles of the shaker operating at 6 and 7.5 Hz. (The two different frequencies represent the same amount of dynamic load due to the two different shaker basket configurations used; the first four deflection levels are at 6 Hz and the remainder are at 7.5 Hz). A comparison between first and fifteenth cycles did not yield a significant difference (presumably due to the ramping nature of the shaker

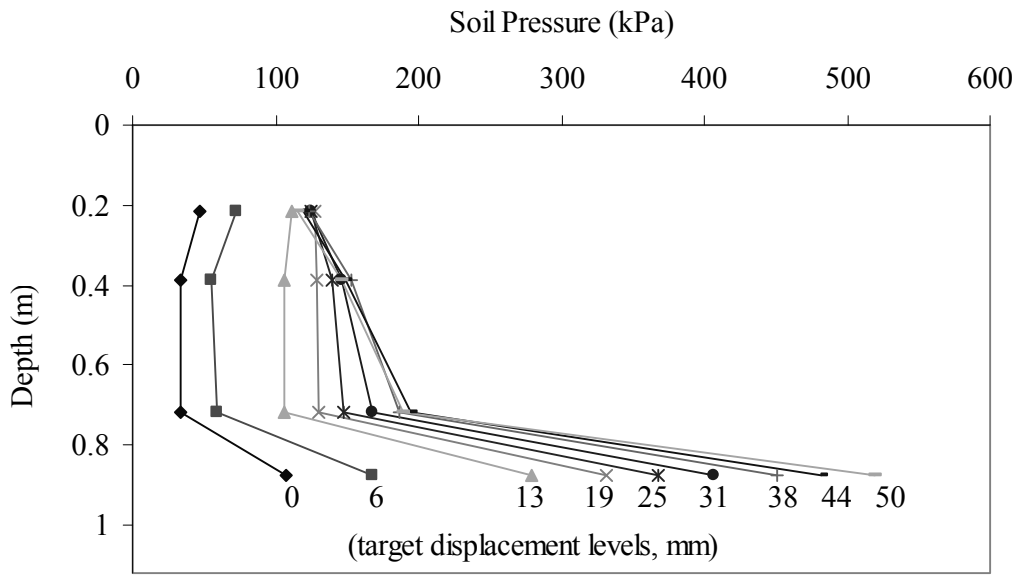

Figure 4-19 Maximum Earth Pressure Distributions Based on Pressure Cells – Dynamic Load Conditions

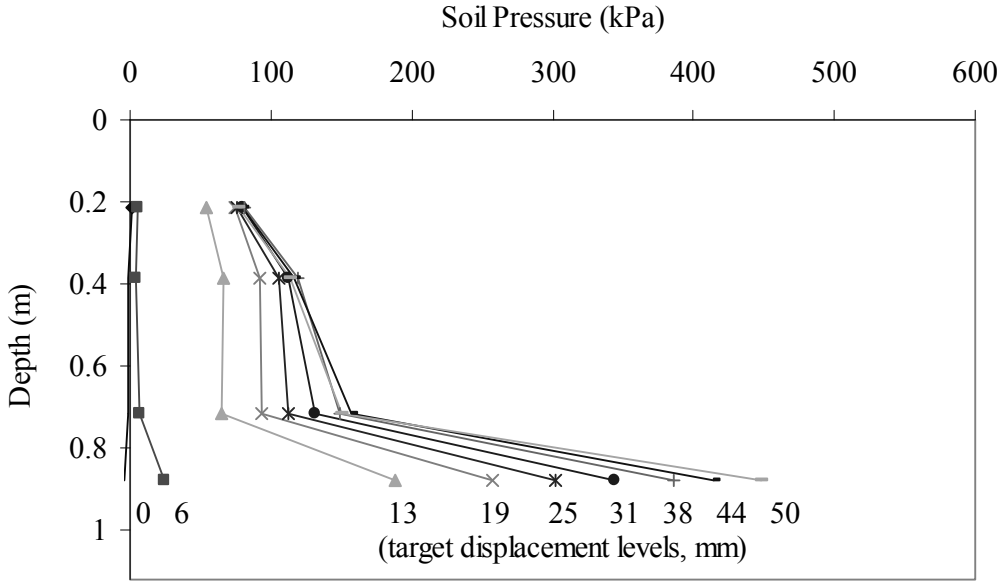

Figure 4-20 Minimum Earth Pressure Distributions Based on Pressure Cells – Dynamic Load Conditions

loading), hence the results of only the "first" cycle are shown. The amount of dynamic pile cap movement associated with each static displacement level can be determined from the dynamic displacement amplitudes shown in Figure 4-6. Doubling the dynamic displacement amplitude in this figure shows the total movement of the pile cap. These plots show a similar concentration of pressure near the bottom of the pile cap for all deflection levels.

The minimum pressures occur as the shaker causes the pile cap to move away from the backfill. Gapping is evident in Figure 4-20 with essentially zero pressure at the 0 and 6 mm static deflection levels. The maximum pressures occur as the shaker moves the pile cap into the soil. Although not shown on this graph, soil pressures decrease after the shaker passes the resonant frequency of the pile cap.

Figure 4-21 and Figure 4-22 show the maximum and minimum dynamic components isolated from combined static-dynamic distributions shown previously in Figure 4-19 and Figure 4-20. The dynamic passive pressure was calculated by subtracting the dynamic maximum and minimum earth pressure cell values from the relaxed earth pressure cell values. The maximum dynamic pressures range from approximately 0 kPa to 40 kPa. The pressure distribution shows that the pressure is increasing with depth for each static displacement level. The minimum dynamic pressures range from approximately -20 kPa to -60 kPa with one outlying pressure at -120 kPa. Negative pressures on the figure do not represent negative pressures on the pile cap face but are showing that under dynamic conditions the net pressure is less than the static pressure. The dynamic-only pressure distribution shows a trend similar to the combined distributions with the greatest change in pressure occurring near the

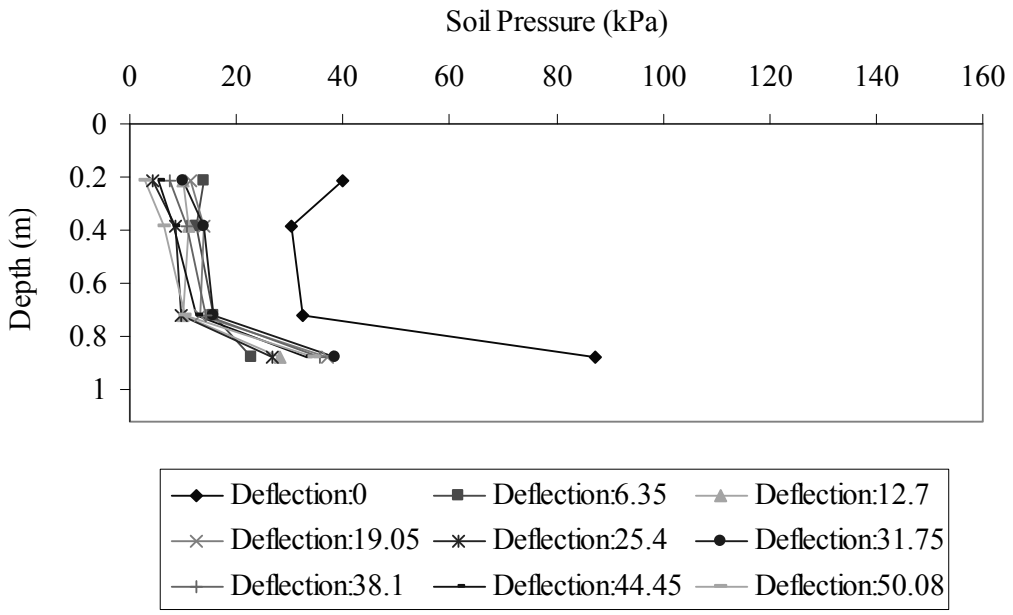

Figure 4-21 Dynamic Component of Maximum Earth Pressure Distributions

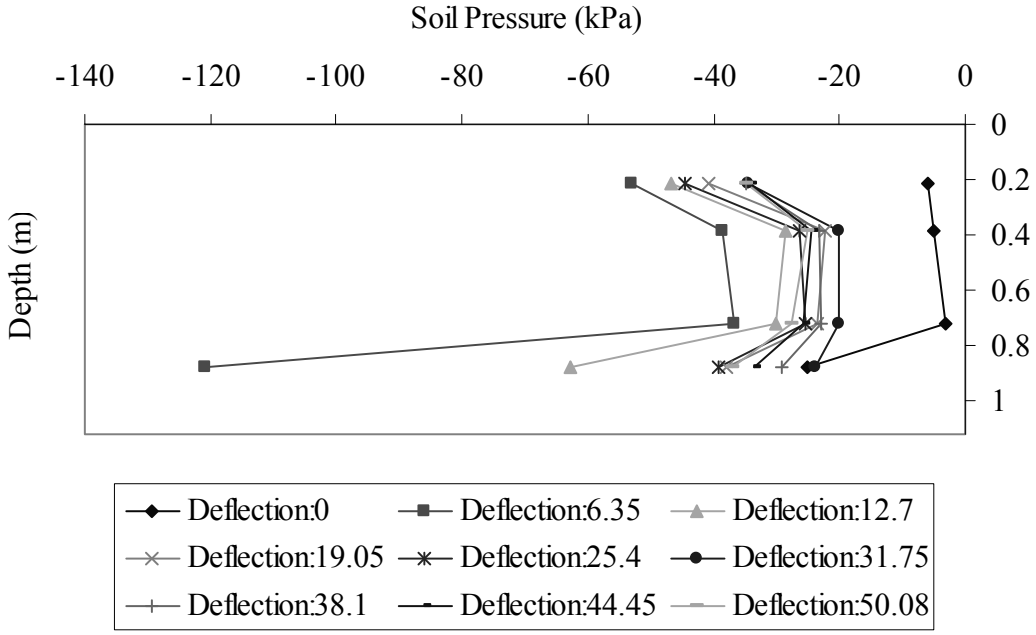

Figure 4-22 Dynamic Component of Minimum Earth Pressure Distributions

bottom of the pile cap. The dynamic pressures have no apparent dependency on static displacement levels.

4.4.3 Resistance Based on Tactile Pressure Sensors

Tactile pressure sensors were also used to measure the static and dynamic passive pressures experienced by the pile cap. To process the sensor data, Tekscan's proprietary I-scan software was used to import a matrix of 40 rows by 10 columns was into a spreadsheet. One such imported matrix (immediately before the shaker run at a static deflection level of 31 mm) is shown in Figure 4-23. The figure shows the top and bottom tactile pressure sensors with a box placed around the area used for the analysis. The tactile pressure sensors were in place for backfill placement and compaction, and the backfilling and compaction processes damaged portions of the tactile pressure sensors as indicated by dead sensels. These sensels showed no pressure being applied to the sensor. In other instances, certain cells showed the maximum calibration pressure, likely indicating a point loading caused by a non-uniform soil particle.

Pressure data was taken from the boxes which were placed in a location with the least amount of dead cells, and also placed to best represent the pressure distribution on the tactile pressure sensors. For analysis purposes, the median value across each row was chosen from the imported data in the belief that the median pressures best represent the actual pressure at a particular depth. The top sensor also seems to have increasing pressure with depth; whereas the bottom sensor shows layers

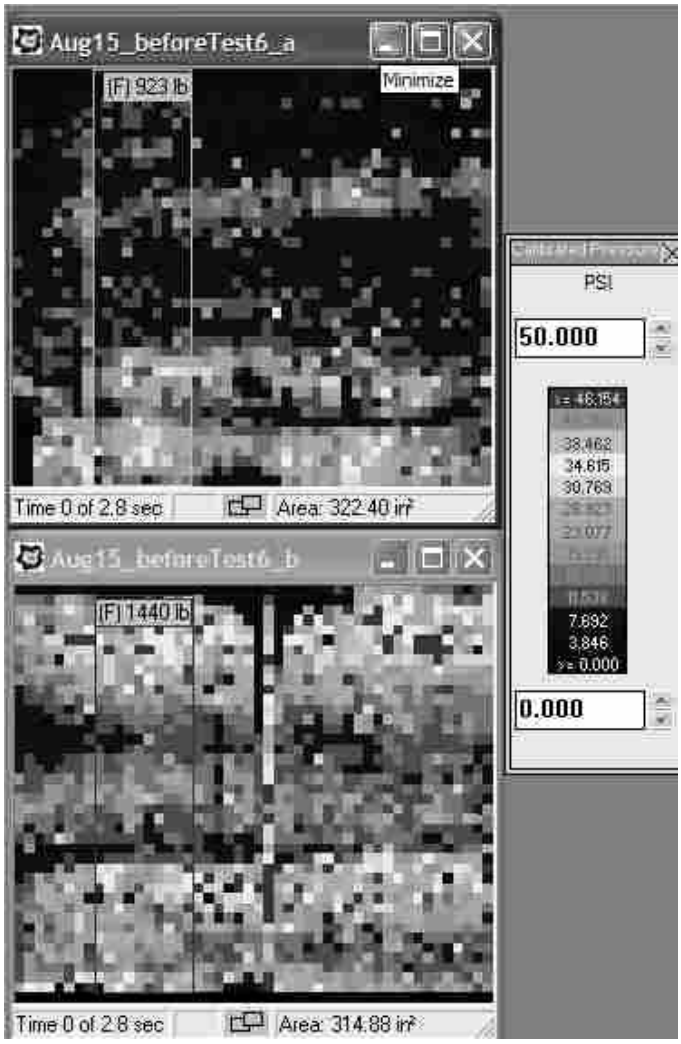

Figure 4-23 Sample of Data from Top and Bottom Tactile Pressure Sensors

of increased pressure. This layering possibly corresponds with the location of the compaction lifts.

Figure 4-24 and Figure 4-25 plot the maximum and minimum combined static and dynamic pressure on the face of the pile cap at three static deflections levels, all at a frequency of 6 Hz. Only three deflection levels are shown in the plots in order to better view the pressure distribution relationships. The figures show a trend of increasing pressure with depth. This effect becomes more pronounced with increasing

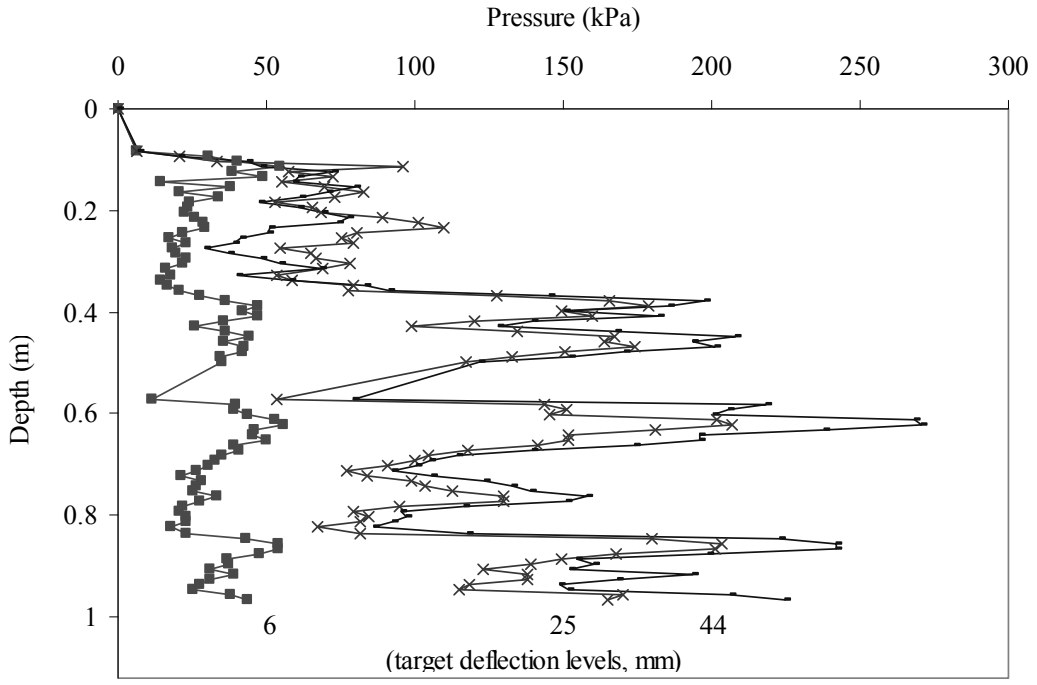

Figure 4-24 Maximum Earth Pressure Distributions Based on Tactile Pressure Sensors – Dynamic Load Conditions

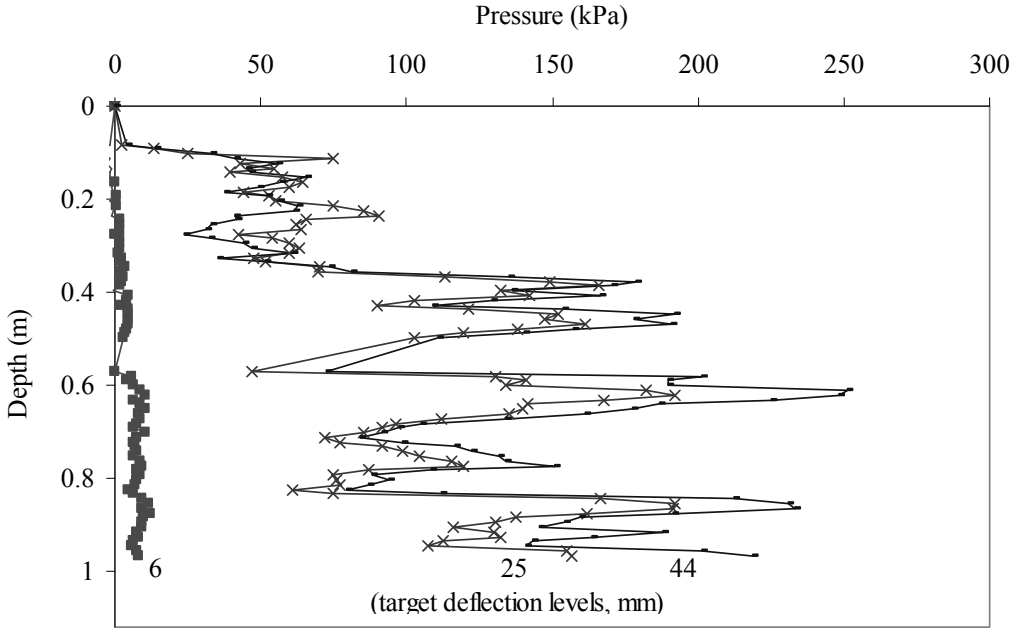

Figure 4-25 Minimum Earth Pressure Distributions Based on Tactile Pressure Sensors – Dynamic Load Conditions

deflection; however, the pressure distribution does not show significant change from a deflection of 25 mm to 44 mm. Point loads and dead sensels are evident in the figures by the scatter of the data points for each deflection level. Again, the effect of gapping is evident in the minimum earth pressure distribution at a static displacement level of 6 mm.

Figure 4-26 and Figure 4-27 compare dynamic pressure distributions from the tactile pressure sensors and the earth pressure cells at 6 Hz and three static deflection levels. Earth pressure cell values are shown as a range covering the diameter of the cell. Pressure values for the tactile pressure sensors are significantly different compared to the earth pressure cells. Despite their limited resolution, the earth pressure cell pressure distributions are believe to better represent the actual passive earth pressure. This believe is in part because the load-deflection curve based on the earth pressure cells is closer to that expected (as discussed in the next section) than the load-deflection curve based on the tactile pressure sensors. Other reasons are also presented in the next section.

4.5 Comparisons of Backfill Resistance

4.5.1 Computed Load-Deflection Curves

As explained previously, the passive earth load-deflection curve for the dense silty sand backfill can be determined by taking the load-displacement curve for the pile cap with the backfill in place and subtracting the baseline response (for example, see Figure 4-15 and Figure 4-17). The passive earth load-deflection curve for the

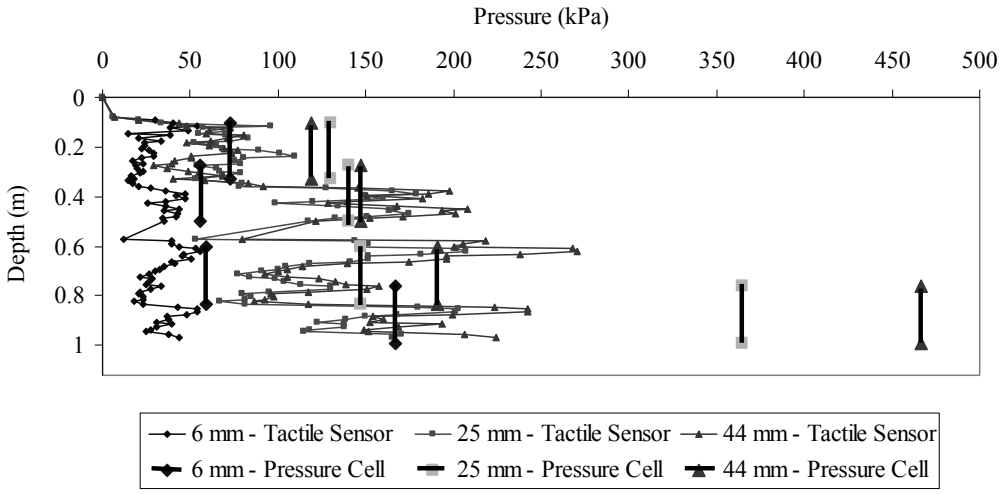

Figure 4-26 Passive Pressure Distribution Comparisons – Maximum Values

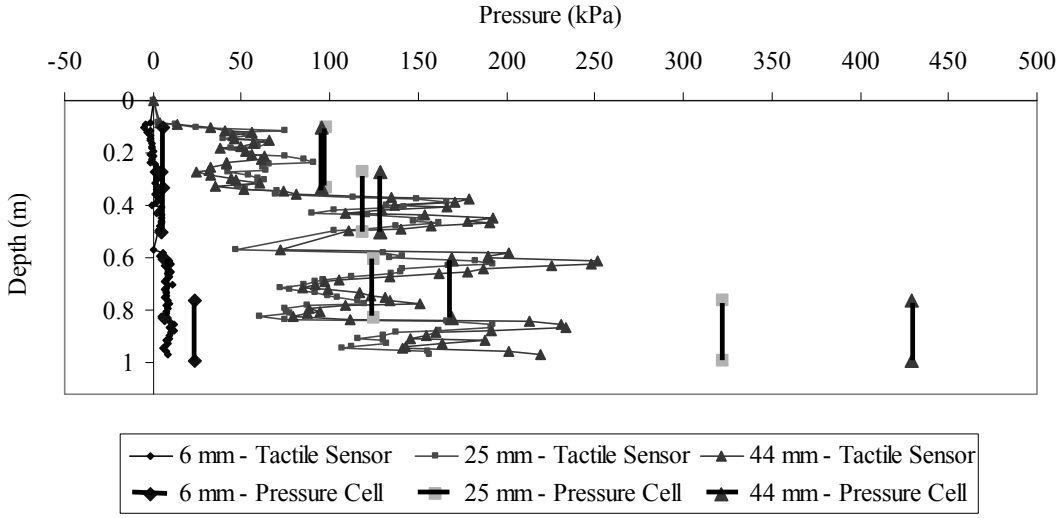

Figure 4-27 Passive Pressure Distribution Comparisons – Minimum Values

backfill can also be calculated using the tributary-area method with the pressure cell and tactile sensor data. (The assumption was made that the measured pressure distributions were representative of those the spanning the entire length (i.e., width) of the pile cap; also, the pressures at the top and bottom of the distributions were extended to the top and bottom of the cap by using a constant value similar to the

endpoints of the distribution). Such load-displacement curves, based on the maximum dynamic pressure occurring at a frequency of 6 Hz, are presented in Figure 4-28. The selection of 6 Hz is somewhat arbitrary and was selected as representing the general dynamic response of the backfilled pile cap system just before resonance effects dominate the response.

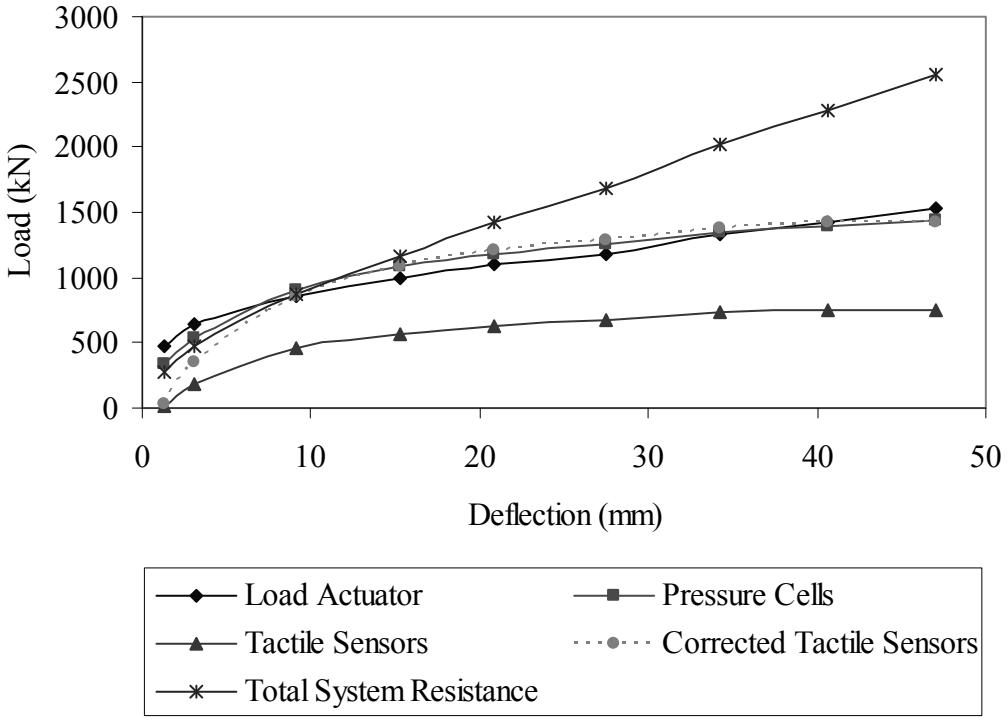

Figure 4-28 Comparison of Computed Passive Earth Load Deflection Curves

In Figure 4-28, there is reasonable agreement between the curves based on the load actuators and the pressure cells. While the trend exhibited by the tactile pressure sensors is very similar to that obtained from the pressure cells, its absolute magnitude is too low. Application of a 1.9 multiplier to the tactile pressure sensor curve provides very good agreement with the pressure cell-based curve. This discrepancy may result

from several possible factors. There might have been compliance issues at the sensor-soil interface, including trapped air within the sensor. Damage to the sensors during backfill installation and testing limited the number of sensels used to determine the load and fewer data points typically means less accuracy. Also, the smooth nature of the sensor itself could results in lower measured load values. The vertical component of the backfill resistance could have introduced shear in the sensor which adversely affected the measurement. Other more likely culprits include the fact that the tactile sensor data was recorded at a maximum sampling rate of approximately 100 samples per second which at high frequencies might not capture peak values. Also, there is a lag in the response time of the tactile sensors which might cause peak dyamic values to be missed.

The three curves depicting dynamic resistance of the pile cap, as recorded by the load actuator, earth pressure cells, and tactile pressure sensor, change slope near the same point of deflection, approximately 15 mm (being a deflection to cap height ratio of 1.3%). The curves begin with a large slope, indicating high stiffness, then gradually reduce in stiffness until the curves become somewhat linear. The slope changes significantly at approximately 1000 kN for the pressure cells and the corrected tactile pressure sensors curve. The same change occurs at approximately 800 kN for the load actuator curve. The change in slope represents the soil beginning to fail. Both the tactile pressure sensors and earth pressure cell curves tend to have the same curved shape, whereas the load actuator slope follows a more linear trend. It may be that the actuator-based curve is not as accurate due to only having one good actuator load signal and approximating the load from both actuators by doubling the

good signal. Such errors would likely be most noticeable in the beginning portions of the curve where load is relatively small and changing rapidly.

4.5.2 Comparisons with Other Predictive Methods

Cole and Rollins (Cole, 2003; Cole and Rollins, 2006; Rollins and Cole, 2006). performed a similar pile cap test with dense silty sand backfill, but without any dynamic loading. Figure 4-29 shows the passive earth load-displacement relationship obtained by them (shown as RTC Silty Sand) together with load deflection curve for the current tests calculated from both actuator loads and earth pressure cells based on relaxed load values. The three curve exhibit relatively good agreement.

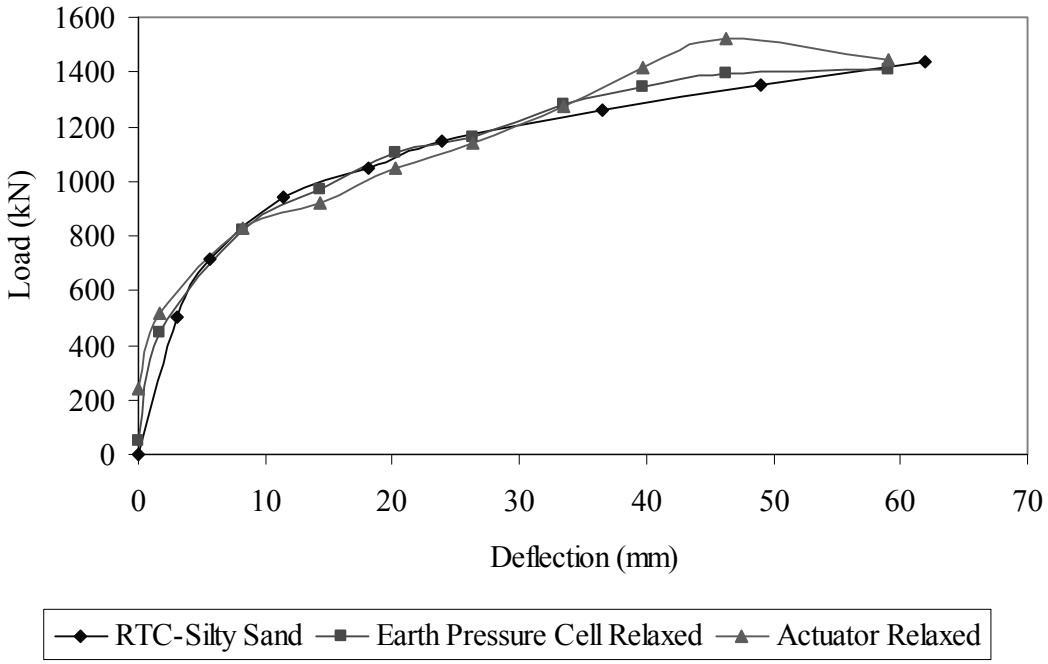

Figure 4-29 Comparison of Passive Earth Load-Deflection Curves from Cole (2003) and Current Dense Silty Sand Backfill Test

The relaxed passive resistance achieved from the current dense silty sand backfill test is approximately 1,400 kN. Using soil shear strength data and geometry of the pile cap, the theoretical horizontal passive force was computed using three methods: Rankine, Coulomb, and log-spiral. Table 4-2 displays the results. In each method, the Brinch Hansen (1966) correction factor was applied for account for three dimensional effects. The correction factor was calculated as 1.20. Table 4-3 summarizes the parameters used in the calculations, including those needed for the complete hyperbolic model of Mokwa and Duncan (2001).

Table 4-2 Measured and Computed Ultimate Passive Force Comparison

Method	Ultimate Horizontal Passive Force, P_{uh}	Error
Measured	1,400 kN	-
Rankine	620 kN	-55%
Coulomb	964 kN	-31
Log Spiral	977 kN	-30

Each method presented underestimates the amount of passive force acting on the pile cap. The Rankine method prodced the lowest value with the highest percent error, which is expected since this method assumes a linear failure surface and neglects wall friction. The Coulomb method was better with an error of 31%. This method also assumes a linear failure surface but accounts for wall friction. The log-spiral method uses a log-spiral shaped failure surface and includes the wall friction in its calculations. The log-spiral method calculates the passive force with a 30% error.

Table 4-3 Summary of Parameters Used to Calculate Horizontal Passive Resistance

cap width,	b (ft) =	17.00
cap height,	H (ft) =	3.67
embedment depth,	z (ft) =	0.00
surcharge,	q_s (psf) =	0.0
cohesion,	c (psf) =	360
soil friction angle,	ϕ (deg.) =	29
wall friction (0.75ϕ),	δ (deg.) =	22
initial soil modulus,	E_i (kip/ft^2) =	800
poisson's ratio,	ν =	0.35
soil unit weight,	γ_m (pcf) =	122
adhesion factor,	α =	1.00
Δ_{max}/H, =		0.013

The wall interface friction angle was assumed to be 0.75ϕ, consistent with Cole. Poisson's ratio was calculated from an empirical formula given by Mokwa and Duncan. The initial soil modulus was a value recommended by Mokwa and Duncan for a dense compacted material. A comparison of the measured load-deflection curves and the hyperbolic curve based on Mokwa and Duncan is shown in Figure 4-30. The agreement is generally good, with the hyperbolic curve slightly overestimating resistance near the "knee" of the curve and underestimating the ultimate value at high levels of deflection.

4.6 Dynamic Damping and Stiffness of the Pile Cap System

A simplified graphical model of the physical test features was created and is presented in Figure 4-31. The left direction is taken as positive directional notation

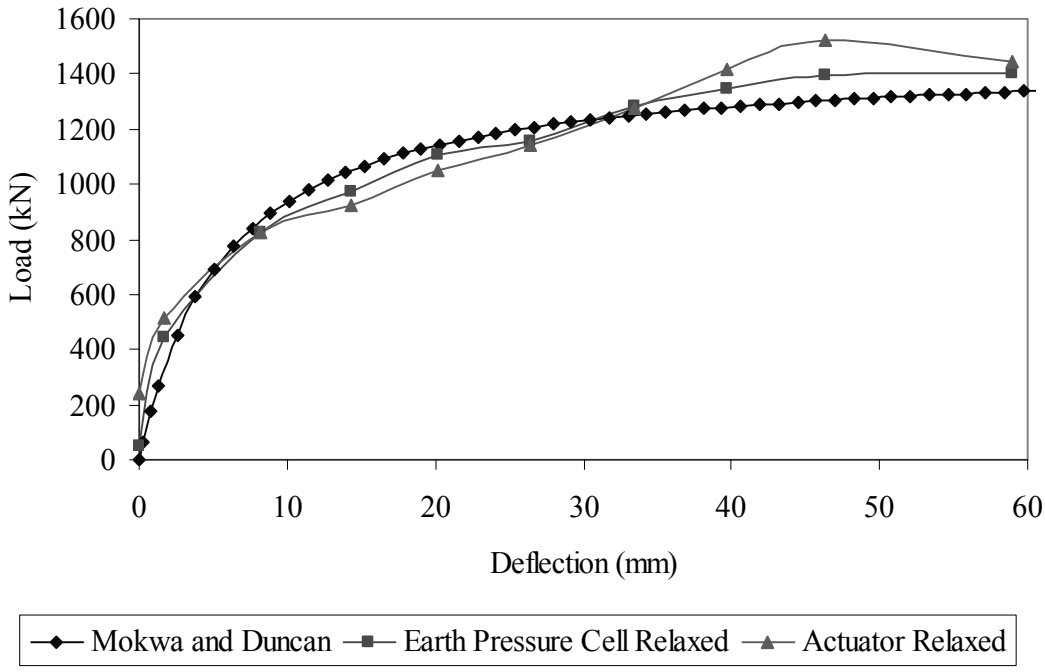

Figure 4-30 Comparison of Passive Earth Load-Deflection Curves from Mokwa and Duncan (2001) and Current Dense Silty Sand Backfill Test

which is the positive signal direction for the accelerations obtained from the accelerometer instrumentation.

As shown in Figure 4-31, R_{TC} is the reaction provided by the backfill soil and piles with components of stiffness and damping. R_{RC} is the reaction provided by the piles of the reaction cap having both stiffness and damping components. F_s is the shaker force provided to the system with a negative signal in the left direction. I_1 and I_2 are the inertial force for each mass, test cap and reaction cap, respectively. When the shaker force changes direction, then the acceleration of the pile cap is taken as a negative value and used in appropriate calculations of the inertial force. Including both pile caps in a free body diagram yields two equilibrium equations, a static and dynamic equilibrium equation (Equation 16 and Equation 17, respectively), provided

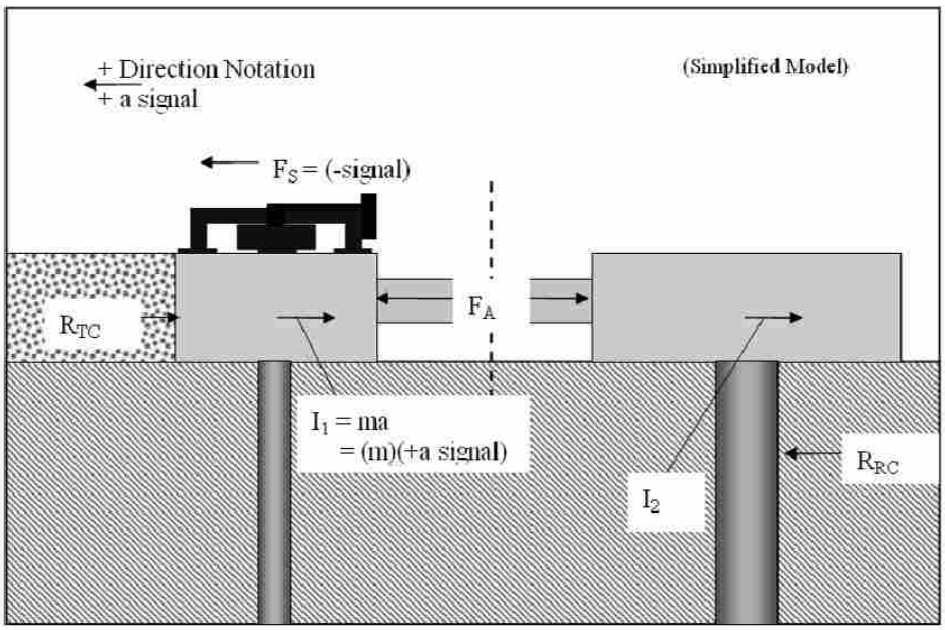

Figure 4-31 System Free Body Diagram with System Forces Represented

that the shaker force is applied such that it can be considered to be static and dynamic, respectively.

$$-R_{TC} + R_{RC} + F_s = 0 \tag{16}$$

$$-R_{TC} + R_{RC} + F_s - I_1 - I_2 = 0 \tag{17}$$

If the system free body were cut into two free bodies, a left side and a right side, at the dash line (through the actuator), then two additional equilibrium equations are obtained (Equation 18 and Equation 19, respectively). These equations allow the dynamic response of the reaction cap to be excluded from the free-body of each pile cap because the forces on the actuators are known. Solving Equation 19 for F_a, and then substituting it into Equation 18 and solving Equation 18 for F_s and substituting

this into Equation 17 (the dynamic equilibrium equation) results in a balanced equation with all forces canceling. With this confirmation, the left equilibrium equation (Equation 18) was used to model the system to obtain dynamic displacement amplitude, average load, stiffness, and damping values.

$$-R_{TC} - I_1 + F_s + F_a = 0 \tag{18}$$

$$R_{RC} - F_a - I_2 = 0 \tag{19}$$

Solving Equation 18 for R_{TC} allows the load in the system (backfill + pile cap) or baseline (no backfill) case to be isolated. To begin the data processing, an input file was prepared which included the load from the actuator, acceleration measurements acquired from the accelerometer, double integrated displacements from the accelerometer (the LVDTs became unreliable due to vibration of the reference frame), and the loop counter signal from the eccentric mass shaker. In addition, the time record and approximate shaker frequency was included. Noise in the accelerometer data was reduced by a zero-phase shift filtering process.

Using the model discussed previously this data was processed by a spreadsheet designed to calculate the shaker force, inertial force, dynamic displacement amplitude, the maximum, minimum, and median values of the displacement, stiffness, damping, and load. In the case of the load, the eccentric shaker force (calculated using Equation 14) and the inertial force load was added/subtracted to/from the actuator load to determine the reaction of the test cap, R_{TC}. The inertial force (in English units) can be calculated using:

$$I_1 = g * 386.4 * mass \tag{20}$$

where g is the measured accelerations with units of “g" and mass includes contributions from the weight of the test pile cap, the weight of an 2.4 m length of the 12 test piles which are assumed to be moving with the cap, half the weight of the two actuators, the weight of the eccentric mass shaker, and the weight of the backfill within a log-spiral shear zone (estimated at 133 kN), for a total of 686 kN.

Resulting system force-displacement loops were used to solve for the dynamic displacement amplitude, u (given by the difference between the maximum and minimum displacements in a given hysteresis loop divided by two), the stiffness, k, (given by the difference between the maximum and minimum load in a given hysteresis loop divided by two then divided by the dynamic displacement amplitude). In this calculation, the average peak-to-peak slopes for the first 20 force-displacement loops during the dwell time at an increment of 0.5 Hz were used. Isolation of each cyclic effect was not exact due to the ramping nature of the eccentric shaker, starting at 1 Hz up to 10 Hz as mentioned before. Damping, ζ, was calculated from the force-displacement loops using the Equation 21:

$$\xi = \frac{1}{4\pi}\frac{A}{E_s} \tag{21}$$

where the area of the hysteresis loop is represented by A, and E_s is the stored strain energy which equals 0.5 k u_o, in which case k is the slope of the loop (stiffness) and u_o is its displacement amplitude.

It is important to note that the results presented in this thesis for frequencies below 3 Hz are not considered reliable since at these frequencies, the effect of the shaker force is not readily distinguishable from the background noise inherent in the actuator loads and accelerometers. Additionally, since the applied force at low frequencies is small, deflections are similarly small, resulting in lower precision in calculating computed stiffness and damping.

4.6.1 Dynamic Damping and Stiffness of Pile Cap with Backfill

Figure 4-32 presents the total stiffness of the pile cap with dense silty sand backfill as a function of forcing frequency and static displacement level. The stiffness values range from approximately 175 kN/mm to 350 kN/mm. Since the dynamic load-displacement loops basically occur along reloading segments of the load-displacement curve rather than along the virgin (i.e., backbone) segment, the stiffnesses are best understood to be reloading stiffnesses rather than a secant tangent originating at zero load and zero displacement.

A general decreasing trend is exhibited of stiffness decreasing with increasing frequency from approximately 3 Hz. At high frequencies the stiffness for each displacement level becomes somewhat constant. This change in trend is caused by the increase and decrease in dynamic displacement amplitude as the system goes through resonance. Generally, as dynamic displacement amplitude increases, the stiffness tends to decrease and this behavior is reflected in the test results shown in Figure 4-32**.**

Figure 4-32 also shows increasing stiffness with increasing static displacement at low static displacement levels; however, at high displacements this trend ceases

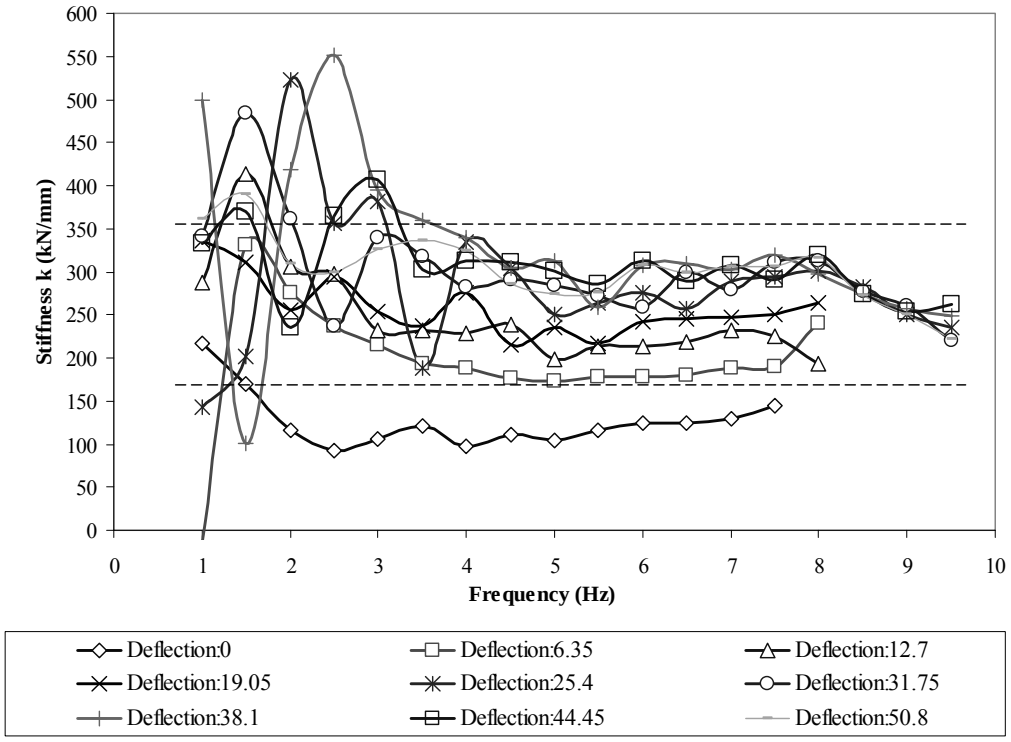

Figure 4-32 Dense Silty Sand System Stiffness as a Function of Forcing Frequency and Static Displacement Level

with stiffness values becoming nearly the same for displacement levels at approximately 300 kN/mm. It is at this point that the soil has failed, restricting the stiffness to that provided only by the piles. At zero static displacement the stiffness values are the smallest ranging between 100 and 200 kN/mm, and the values become larger as static displacement increases and more of the ultimate passive strength of the backfill soil is mobilized.

The damping ratio is plotted as a function of forcing frequency and static displacement level in Figure 4-33. The damping values are increasing with frequency with values ranging from approximately 30% to 50% from frequencies of 3 Hz to 6 Hz. The damping ratio slightly decreases with increasing frequency from 6 Hz to 8

Hz with damping values ranging from 25% to 40%. The damping values are relatively consistent for the deflection levels indicating that damping is unaffected by static deflection level; however, smaller damping values are noted for the two lowest static deflection levels. At low deflection levels, the passive force on the cap may not be mobilized sufficiently to produce the higher levels of damping observed at greater deflection levels.

This amount of damping is substantially greater than the 5% assumed in structural applications. This amount of damping is consistent with values of 5 to 19% cited by Barkan (1962), the latter of which increased to 32% once the foundation in question was backfilled to a height of 1 m.

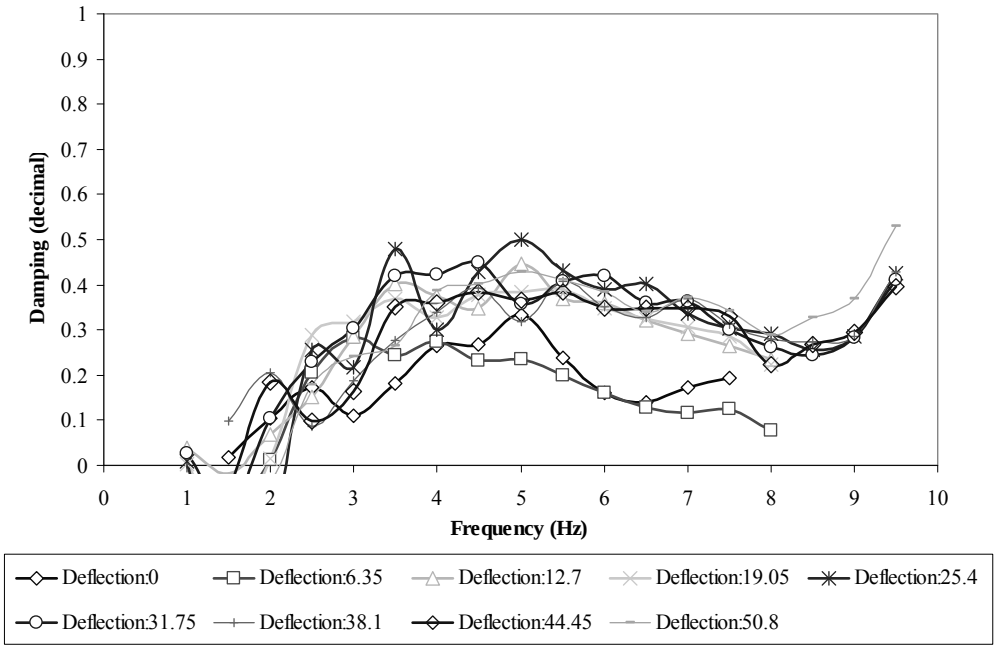

Figure 4-33 Dense Silty Sand System Damping as a Function of Forcing Frequency and Static Displacement Level

4.6.2 Dynamic Damping and Stiffness of Pile Cap without Backfill

Plots of the dynamic pile (baseline) stiffness as a function of forcing frequency are provided for each static displacement level in Figure 4-34. The plots show each static displacement test taking on stiffness values in the region of 40 kN/mm to 100 kN/mm for frequencies between 4 and 8 Hz. This stiffness is about one-third of that observed for the test with backfill in place. Figure 4-34 shows a trend of decreasing stiffness from 3 to 5.5 Hz. Thereafter, the system begins to increase in stiffness. This decrease in stiffness from 3 to 5.5 Hz is likely due in part to the increases in dynamic displacement amplitude caused by system resonance. This is consistent with the observation that stiffness typically decreases as displacement increases.

The damping ratio for the pile cap alone (baseline condition) is plotted as a function of forcing frequency for tests at each static deflection level in Figure 4-35. The test results indicate that damping decreases substantially as the forcing frequency increases. There does not appear to be any consistent trend in damping with static deflection level. In addition, the damping exhibited by the 6.35 mm displacement does not follow the normal trend and will currently be ignored. In the frequency range from 3 Hz to 4.5 Hz, the damping ratio was within the range of 25% to 50%. However, from 4.5 Hz to 8 Hz, the data shows a decreasing trend in damping trailing off to zero between 8 and 9 Hz. It is possible that part of the behavior shown at frequencies greater than the resonant frequency (such as the damping trending to zero) are due to imprecise superposition of the shaker load (which is based on a single position pulse signal) on the actuator loads, which is caused by fewer data points per cycle with increasing shaker frequency.

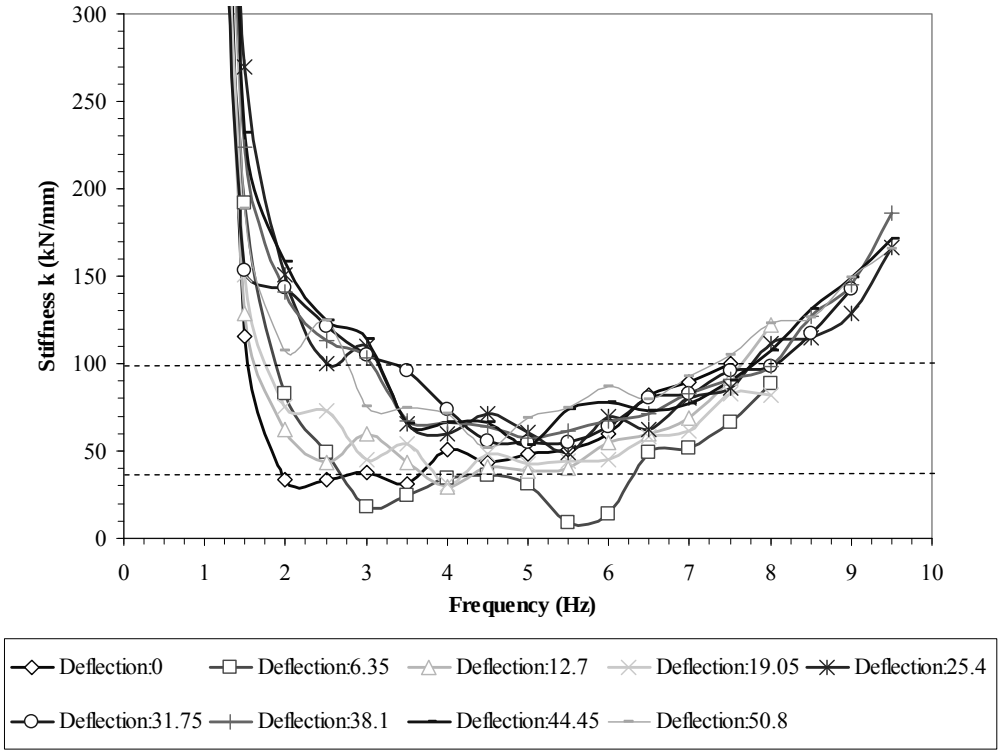

Figure 4-34 Baseline Stiffness as a Function of Forcing Frequency and Static Displacement Level

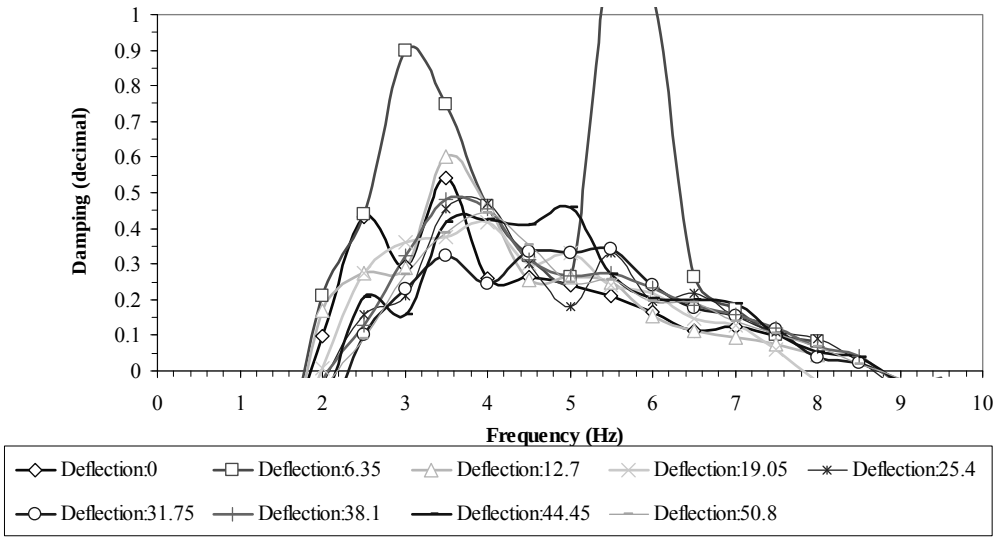

Figure 4-35 Baseline Damping as a Function of Forcing Frequency and Static Displacement Level

4.6.3 Dynamic Damping and Stiffness of Backfill

Figure 4-36 shows the stiffness of the backfill as a function of forcing frequency for each static displacement level. The stiffness for the passive earth resistance were calculated by subtracting the stiffness of the baseline response from the stiffness of the test pile cap system with the backfill in place. The stiffness values for the passive earth resistance decreases from 3 Hz till the peak frequency for each deflection level with a sharp decrease at 8 Hz. The stiffness values range from 120 kN/mm to 250 kN/mm, which are approximately two-thirds of the stiffness of the pile cap with the backfill in place.

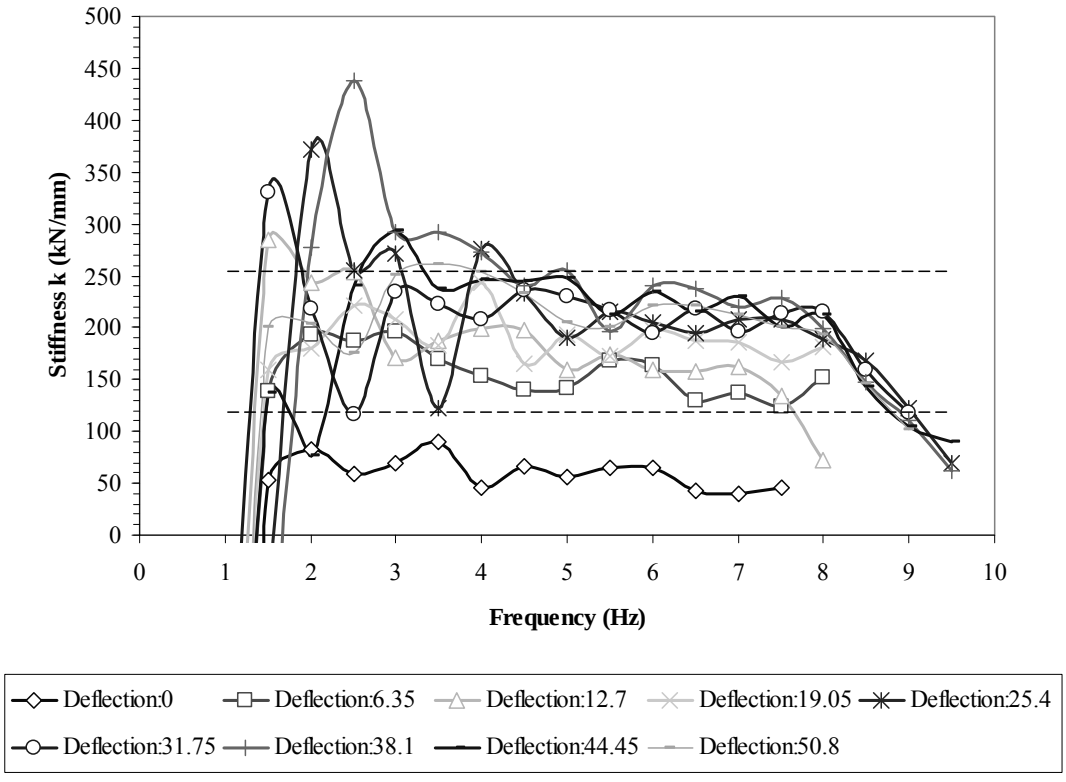

Figure 4-36 Dense Silty Sand Backfill Stiffness as a Function of Forcing Frequency and Static Displacement Level

The damping ratio for the passive backfill soil alone is plotted as a function of forcing frequency for tests at each static deflection level in Figure 4-37. The dense silty sand backfill damping ratio was obtained by first calculating the damping coefficient, c, for both the system (backfill) and baseline (no backfill) case using Equation 22 and Equation 23:

$$c_{system} = \zeta_{system} * 2\sqrt{k_{system} * m_{system}} \tag{22}$$

$$c_{baseline} = \zeta_{baseline} * 2\sqrt{k_{baseline} * m}_{baseline} \tag{23}$$

$$c_{backfill} = c_{system} - c_{baseline} \tag{24}$$

$$\zeta_{backfill} = \frac{c_{backfill}}{2\sqrt{k_{backfill} * m_{backfill}}} \tag{25}$$

where, ζ is the damping ratio, k is the stiffness, and m is the mass. Next, the baseline damping coefficient is subtracted from the system damping coefficient to isolate the dense silty sand (backfill) damping coefficient (Equation 24). Finally, the damping ratio is recomputed using Equation 25 with the known stiffness and mass of the dense silty sand backfill.

Damping as a function of forcing frequency is plotted in Figure 4-37. To improve clarity among the scattering of the data, the median value over the full static deflection range is plotted for each frequency in the figure. The figure shows increasing damping with frequency. At 3 Hz the damping ratio is approximately 32% and then increases to approximately 67% at 6 Hz, where the value becomes fairly constant for the remainder of the frequency levels. While these ratios are higher than

the 0 to 20% range often contemplated by engineers, the values are consistent with the increase observed between the backfill and no backfill cases. The damping from the backfill by itself must, with its relatively smaller mass, be significantly larger than the baseline response if there is to be an appreciable increase in damping (as was observed in these tests) for the pile cap system with the backfill in place. In a related vein, damping ratios range from approximately 20% to 30% for soils at high cyclic strains as shown by Vucetic and Dobry (1991).

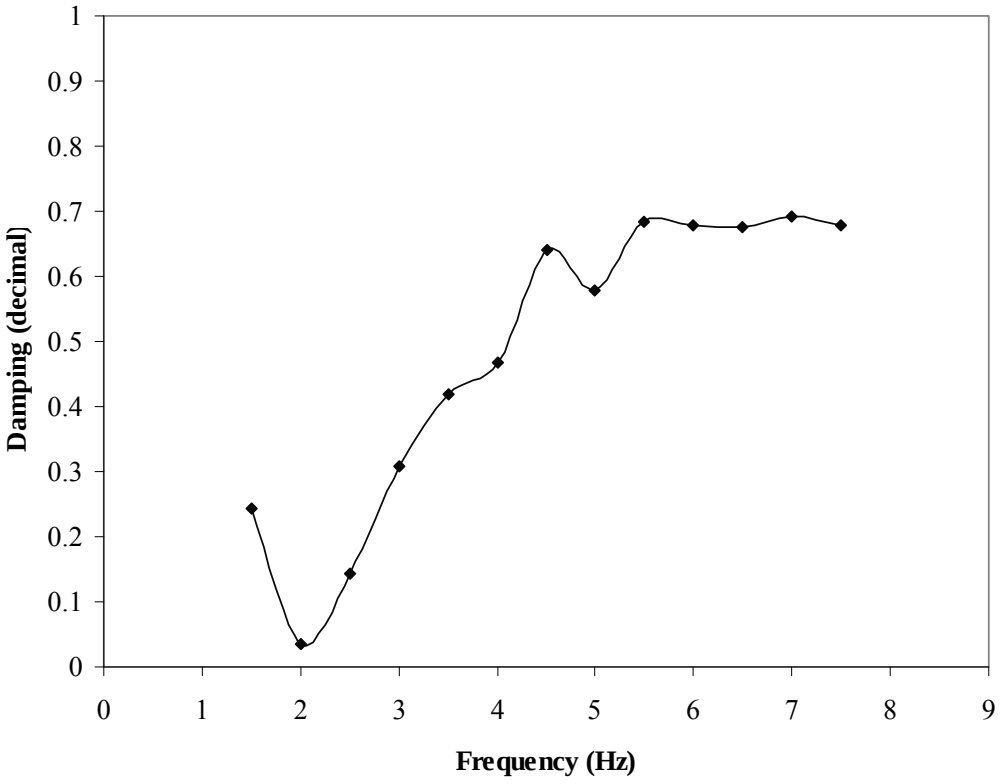

Figure 4-37 Dense Silty Sand Backfill Damping as a Function of Forcing Frequency

5 Conclusions

Based on the results of the cyclic and dynamic testing of a full-scale pile cap with and without dense silty sand backfill in place, the following conclusions are presented:

1) The presence of the backfill significantly increased the lateral load resistance of the pile-cap system. The resistance was nearly doubled at a 50 mm deflection level.

2) After initial loading, the pile cap system experienced a loss in load resistance. In the case with backfill present, this relaxation generally represented a 10 to 15% loss in resistance.

3) After undergoing dynamic, cyclic loading, the resistance of the backfilled pile cap was approximately 40 to 80% of its initial value. Dynamic displacement amplitudes were on the order of 0 to 2 mm.

4) The damped natural frequency of the pile cap with backfill varied from approximately 6.5 to 8.5 Hz, increasing with static displacement level. The damped natural frequency of the pile cap without backfill varied from approximately 5.5 to 6 Hz, also increasing with static displacement level.

5) For the pile cap with backfill, load resistance slightly decreases with increasing dynamic displacement amplitude and frequency. This suggests

that either the soil is behaving non-linearly at these small displacement levels, or that cyclic effects which degrade resistance are more prominent than rate loading effects which tend to increase resistance or that resist. For the test cap without backfill, there was no decrease in resistance with increasing dynamic displacement amplitude and frequency.

6) Earth pressure measurements made by pressure cells and tactile pressure sensors showed somewhat different pressure distributions along the pile cap face. When summed to determine soil load acting on the pile cap, the load-displacement trends were consistent, but the tactile senor data needed a 1.9 multiplier to obtain the correct magnitude. Tactile pressure sensors are not as robust as pressure cells, being subject to point loading, damage, and other factors.

7) The earth pressure cells indicate that the passive pressure from the backfill is non-linear, with a concentration of pressure near the bottom of the pile cap.

8) Rankine, Coulomb, and log-spiral earth pressure theories underestimated the passive earth pressure from the backfill by at least 30%. A hyperbolic load-displacement model provided a reasonable match to the passive earth load-deflection relationship derived from both actuator loads and earth pressure cells.

9) On average, the presence of the backfill increased the reloading stiffness of the pile cap by a factor of three to four.

10) On average, the presence of the backfill increased the damping ratio of the pile cap by a factor of two. The damping ratio exhibited between both backfill cases ranged from negligible to 50%, depending of forcing frequency and static displacement level.

11) The dense silty sand backfill acting by itself on the face of the 1.12 m tall and 5.18 m wide pile cap face exhibited a reloading stiffness on the order of 120 to 250 kN/mm and a damping ratio of 30 to 70%. These damping ratios are significantly higher than that typical expected for structural materials but appear to be consistent with values for soils.

6 References

Bakeer, R.M., Bhatia, S.K., and Ishibashi, I. (1990). "Dynamic earth pressure with various gravity wall movements." *ASCE Special Publication No. 25*, pp. 887-899.

Barkan, D.D. (1962). *Dynamics of Bases and Foundations.* McGraw-Hill, New York.

Cole, R.T. (2003). "Full-scale effects of passive earth pressure on the lateral resistance of pile caps." Doctor of Philosophy Dissertation, Brigham Young University, Provo, Utah.

Cole, R.T. and Rollins, K.M. (2006). "Passive earth pressure mobilization during cyclic loading." *Journal of Geotechnical and Geoenvironmental Engineering*, ASCE, Vol. 132, No. 9, pp. 1154-1164.

Duncan, J. M., and Mokwa, R. L. (2001). "Passive earth pressures: theories and tests." *Journal of Geotechnical and Geoenvironmental Engineering,* ASCE Vol. 127, No. 3, pp. 248-257.

Elms, D.G. and Richards, R. (1990). "Seismic design of retaining walls." *ASCE Special Publication No. 25*, pp. 854-871.

Filz, G.M. and Brandon, T.L. (1994). "Static and dynamic measurements using embedded earth pressure cells." *Transportation Research Record,* Vol. 1432, pp. 86-95.

Filz, G.M. and Duncan, J.M. (1993). "Drift of flush-mounted pressure cell readings." *Geotechnical Testing Journal*, GTJODJ, Vol. 16, No. 4, pp. 432-441.

Maroney, B. (1995). "Large scale abutment tests to determine stiffness and ultimate strength under seismic loading." PhD Dissertation, University of California, Davis, California.

Mokwa, R. L. and, Duncan, J. M. (2001). "Experimental evaluation of lateral-load resistance of pile caps." *Journal of Geotechnical and Geoenvironmental Engineering,* ASCE Vol. 127, No. 2, pp. 185-192.

Paikowsky, S.G. and Hajduk, E.L. (1997). "Calibration and use of grid-based tactile pressure sensors in granular material." *Geotechnical Testing Journal*, GTJODJ, Vol. 10, No. 2, pp. 218-241.

Personius, S.F., and Scott, W.E. (1992). "Surficial geologic map of the Salt Lake City segment of the Wasatch Fault Zone, Davis, Salt Lake, and Utah Counties, Utah" U.S. Geological Survey miscellaneous Investigation Series Map 1-2106, scale 1:50,000.

Rollins, K.M. and Cole, R.T. (2006). "Cyclic lateral load behavior of a pile cap and backfill." *Journal of Geotechnical and Geoenvironmental Engineering*, ASCE, Vol. 132, No. 9, pp. 1143-1153.

Romstad, K., Kutter, B., Maroney, B., Vanderbilt, E., Briggs, M., and Chai, Y.H. (1996). "Longitudinal strength and stiffness behavior of bridge abutments," California Department of Transportation.

Seed, H.B., Whitman, R.B. (1970). "Design of earth retaining structures for dynamic loads," *Lateral Load Stresses in the Ground and Design of Earth-Retaining Structures*. ASCE, pp. 103-147.

Vucetic, M., and Dobry, R. (1991). "Effect of Soil Plasticity on Cyclic Response," *Journal of Geotechnical Engineering*, ASCE, Vol. 117, No. 1, pp. 89-107.

Whitman, R.V. (1990). "Seismic design and behavior of gravity retaining walls." *ASCE Special Publication No. 25*, pp. 817-842.